Precambrian Research 270 (2015) 334–368

Contents lists available at ScienceDirect

Precambrian Research

journal homepage: www.elsevier.com/locate/precamres

Evolution of a ~2.7 Ga large igneous province: A volcanological, geochemical and geochronological study of the Agnew Greenstone Belt, and new regional correlations for the Kalgoorlie Terrane (Yilgarn Craton, Western Australia)

Patrick C. Hayman[a,b,*], Nicolas Thébaud[c], Mark J. Pawley[d], Stephen J. Barnes[e], Ray A.F. Cas[a], Yuri Amelin[f], Jyotindra Sapkota[g], Richard J. Squire[a], Ian H. Campbell[f], Ian Pegg[h]

[a] Monash University, School of Earth Atmosphere and Environment, Melbourne, VIC 3800, Australia
[b] Queensland University of Technology, Earth Environment and Biological Sciences, GPO Box 2434, Brisbane, QLD 4001, Australia
[c] University of Western Australia, Centre for Exploration and Targeting, 35 Stirling Highway, M006, Crawley, WA 6009, Australia
[d] Geological Survey of South Australia, Level 4, 101 Grenfell St, Adelaide, SA 5001, Australia
[e] CSIRO Earth Science and Resource Engineering, ARRC, PO Box 1130, Bentley, WA 6102, Australia
[f] The Australian National University, Canberra, ACT 0200, Australia
[g] Geological Survey of Western Australia, PO Box 1664, Kalgoorlie, WA 6433, Australia
[h] Agnew Gold Mining Company, Leinster, WA, Australia

ARTICLE INFO

Article history:
Received 9 February 2015
Received in revised form 17 August 2015
Accepted 11 September 2015
Available online 25 September 2015

Keywords:
Agnew Greenstone Belt
Archean volcanism
Large igneous province
Kalgoorlie Terrane
Chronology
Basin architecture

ABSTRACT

The thick package of ~2.7 Ga mafic and ultramafic lavas and intrusions preserved among the Neoarchean of the Kalgoorlie Terrene in Western Australia provides valuable insight into geological processes controlling the most prodigious episode of growth and preservation of juvenile continental crust in Earth's history. Limited exposure of these rocks results in uncertainty about their age, physical and chemical characteristics, and stratigraphic relationships. This in turn prevents confident correlation of regional occurrences of mafic and ultramafic successions (both intrusive and extrusive) and hinders the interpretation of tectonic setting and magmatic evolution. A recent stratigraphic drilling program of the Neoarchean stratigraphy of the Agnew Greenstone Belt in Western Australia has provided continuous exposures through a c. 7 km thick sequence of mafic and ultramafic units. In this study, we present a volcanological, lithogeochemical and chronological study of the Agnew Greenstone Belt, and provide the first pre-2690 Ma regional correlation across the Kalgoorlie Terrane. The Agnew Greenstone Belt records ~30 m.y. of episodic ultramafic–mafic magmatism that includes two cycles, each defined by a komatiite that is overlain by units that become more evolved and contaminated with time. The sequence is divided into nine conformable packages, each consisting of stacked subaqueous lava flows and comagmatic intrusions, as well as two sills without associated extrusions. Lavas, with the exception of intercalations between two units, form a layer-cake stratigraphy and were likely erupted from a system of fissures tapping the same magma source. The komatiites are not contaminated by continental crust ($[La/Sm]_{PM} \sim 0.7$) and are of the Al-undepleted Munro-type. Crustal contamination is evident in many units (Songvang Basalt, Never Can Tell Basalt, Redeemer Basalt, and Turrett Dolerite), as judged by $[La/Sm] > 1$, negative Nb and Ti anomalies, and geochemical mixing trends towards felsic contaminants. Crystal fractionation was also significant, with early olivine and chromite (Mg# > 65) followed by plagioclase and clinopyroxene removal (Mg < 65), and in the most evolved case, titanomagnetite accumulation. Three new TIMS dates on granophyric zones of mafic sills and one ICP-MS date from an interflow felsic tuff are presented and used for regional stratigraphic correlation. Cycle I magmatism began at ~2720 Ma and ended ~2705 Ma, whereas cycle II began ~2705 Ma and ended at 2690.7 ± 1.2 Ma. Regional correlations indicate the western Kalgoorlie Terrane consists of a remarkably similar stratigraphy that

* Corresponding author at: Queensland University of Technology, Earth Environment and Biological Sciences, GPO Box 2434, Brisbane, QLD 4001, Australia. Tel.: +61 7 3138 2261; fax: +61 7 3138 1535.
E-mail address: patrick.hayman@qut.edu.au (P.C. Hayman).

http://dx.doi.org/10.1016/j.precamres.2015.09.016
0301-9268/© 2015 Elsevier B.V. All rights reserved.

can be recognised at Agnew, Ora Banda and Coolgardie, whereas the eastern part of the terrane (e.g., Kambalda Domain) does not include cycle I, but correlates well with cycle II. This research supports an autochthonous model of greenstone formation, in which one large igneous province, represented by two complete cycles, is constructed on sialic crust. New stratigraphic correlations for the Kalgoorlie Terrane indicate that many units can be traced over distances >100 km, which has implications for exploration targeting for stratigraphically hosted ultramafic Ni and VMS deposits.

© 2015 Elsevier B.V. All rights reserved.

1. Introduction

Many Archean greenstone belts, including the Abitibi in Canada, Barberton in South Africa, and Kalgoorlie Terrane in Western Australia, consist of a lower sequence of intercalated komatiites and tholeiites that are overlain by felsic volcanics and sediments. The evolution, from onset to termination, of magmatism has been the focus of several studies. A common feature of these studies is cyclic magmatism, whereby there is an overall trend from komatiites at the base to more evolved rocks such as komatiitic basalts, tholeiites, and in some cases andesites and rhyolites (e.g., Kambalda Sequence, Yilgarn Craton: Arndt and Jenner, 1986; lower Pilbara Supergroup: Arndt et al., 2001; Abitibi, Canada: Ayer et al., 2002; Belingwe Greenstone Belt, Zimbabwe: Shimizu et al., 2005; Murchison Domain, Yilgarn Craton: Van Kranendonk et al., 2013). There are also many cases where cyclicity is not evident (e.g., Dundonald succession, Abitibi: Barrie et al., 1999; Taishan Greenstone Belt: Polat et al., 2006; SW Greenland: Polat et al., 2011), and rare examples of reverse cycles are known (e.g., Klipriviersberg Group, South Africa: Marsh et al., 1992). This stratigraphic diversity has led to a variety of interpretations for the geodynamic setting for the Archean terranes, ranging from intra-continental rifts, mid-ocean spreading centres, back-arc basins, island arcs, oceanic plateaux, plumes, and subduction-accretion models (Polat et al., 2011; Bédard et al., 2013). Plume sources are generally invoked for the genesis of komatiites (Campbell et al., 1989; McDonough and Ireland, 1993), whereas inferred magma sources for basaltic rocks range from plume melting of near-chondritic mantle, enriched mantle, eclogites, and subduction-related melting. Crustal contamination (up to ~30%) is also widely regarded as an important process in Archean magmatism (Sparks, 1986).

Stratigraphic and geochemical studies of Phanerozoic large igneous provinces, which are analogues to Archean greenstone belts, provide valuable insight into the evolution of magmatic systems and tectonic setting (e.g., Deccan Traps: Cox and Hawkesworth, 1984; East African Rift: Coleman and McGuire, 1988; Schilling et al., 1992; Siberian Traps: Lightfoot et al., 1993; SE Greenland: Fitton et al., 2000; Ontong Java: Fitton and Godard, 2004; Columbia River Flood Basalts: Hooper et al., 2007). The study of Archean terranes is more challenging because of deformation, metamorphism, alteration, poor exposure, and the presence of numerous sills. Our ability to reconstruct the evolution of Archean greenstone belts is strongly dependent on stratigraphic reconstructions. For this reason, a multi-disciplinary approach is necessary to establish the evolution of these successions. This approach requires a robust understanding of the lithofacies associations of the principal stratigraphic units, their lithogeochemical characteristics and strong geochronological controls.

The Kalgoorlie Terrane forms the westernmost part of the Eastern Goldfields Superterrane (Cassidy et al., 2006; Barley et al., 2008) in Western Australia. It contains several thick packages of ultramafic and mafic rocks that have been interpreted to represent the products of a single cycle of magmatism spanning ~15–20 Ma (Campbell and Hill, 1988; Connors et al., 2005). For example, at Kambalda in the southern part of the Kalgoorlie Terrane, the ~2710 Ma tholeiitic Lunnon Basalt with mild light-rare earth element (LREE) depletion, (Squire et al., 1998) is overlain by komatiite lavas (Kambalda Komatiite), which are widely regarded as a marker horizon across the Kalgoorlie Terrane. These, in turn, are overlain by two LREE-enriched basalts (Devon Consols and Paringa Basalts, ~2690 Ma; Clout, 1991). The sequence is interpreted by many as being formed by plume-driven melting underneath felsic crust (Campbell and Hill, 1988), and that the upper basalts are formed through crustal contamination of the komatiite (Lesher and Arndt, 1995; Barnes et al., 2012). Campbell et al. (1989) consider the underlying Lunnon Basalt to be the product of melting in a cooler mantle plume head, whereas the younger komatiite is considered the product of melting in the hotter plume tail.

However, to apply this model of a single plume-driven volcanic cycle across the Kalgoorlie Terrane seems problematic. In some places multiple komatiite units are known or suggested (e.g., Coolgardie: Hunter, 1993; Standing, 2001; Agnew: Beardsmore, 2002; Mt Keith: Rosengren et al., 2005; Norsemen: Barley et al., 2008). Elsewhere, such as at Ora Banda (Witt, 1995), the basalts underlying the komatiite are geochemically different to the Lunnon Basalt at Kambalda, including some basalt with LREE-enrichment (Said et al., 2010) similar to upper basalts at Kambalda. These features can potentially be explained by thrusting and repetition of stratigraphy and/or folding, although they may also represent a more complex stratigraphic architecture.

The Agnew district, situated in the north-middle part of the Kalgoorlie Terrane, consists of ultramafic–mafic rocks that are overlain by felsic volcaniclastic and siliciclastic sedimentary rocks, which are intruded by voluminous felsic plutons (Platt et al., 1978; Beardsmore, 2002; Duuring et al., 2012). The few published ages indicate that the basalts overlying the Agnew Komatiite are coeval with the basalts above the komatiite at Kambalda. Basaltic units below the Agnew Komatiite have previously been identified, but have not been examined in detail. In this paper we present a new stratigraphy for the Agnew district that is complemented by new geochemistry and geochronology. The greenstone belt is well suited for stratigraphic study because it preserves up to 7 km of continuous stratigraphy and has experienced relatively low degrees of metamorphism (greenschist to lower amphibolite) so that primary textures are commonly preserved, and extensive localities are relatively undeformed. In addition, recent stratigraphic drilling has provided access, for the first time, to a large part of the succession. The results of our study show that the ultramafic–mafic dominated succession can be divided into nine conformable extrusive units (many of which include comagmatic intrusions) that constitute two magmatic cycles. Each cycle displays progressive crustal contamination and crystal fractionation and can be correlated with coeval stratigraphy elsewhere in the Kalgoorlie Terrane. This study has important implications for the evolution of the Kalgoorlie Terrane and Neoarchean volcanic successions elsewhere in the world.

2. Geologic context

The Agnew district (Fig. 1) is located in the Kalgoorlie Terrane of the Eastern Goldfields Superterrane of the Yilgarn Craton, which has been divided into a number of domains based on geological, geophysical, geochemical, isotopic, and

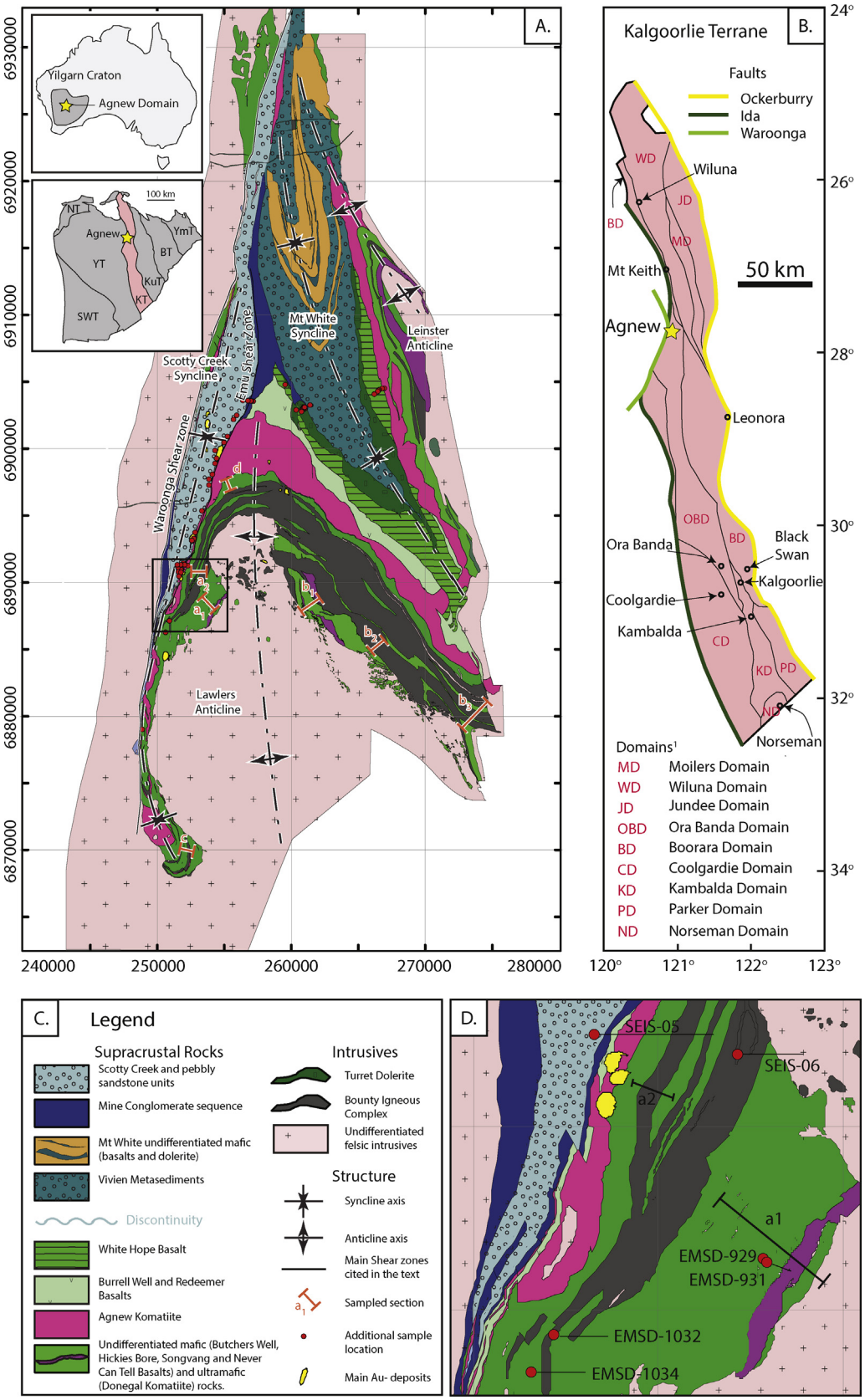

Fig. 1. Location map of the Agnew Greenstone Belt (AGB). (A) Local map of Agnew geology with field traverses and drillholes indicated. Grid reference in MGA. Location of AGB within Australia (upper inset) and the Yilgarn Craton (lower inset). NT, Naryeer Terrane; SWT, Southwest Terrane; YT, Youanmi Terrane; KT, Kalgoorlie Terrane, KuT, Kurnalpi Terrane; BT, Burtville Terrane and YmT, Yamarna Terrane. (B) Map of the Kalgoorlie Terrane with subdomains and faults indicated; 1 = after Cassidy et al. (2006). (C) Legend for (A) and (D). (D) Geology map of the Western Limb of the Lawlers Anticline with traverse and drillholes indicated.

geochronological data (Fig. 1b; Cassidy et al., 2006). The Kalgoorlie Terrane is dominated by large calc-alkaline monzogranites to granodiorites (Smithies and Witt, 1997) with minor tonalites and potassic granitoids encircled by predominantly young (2.71–2.66 Ga), and minor older (>2.73 Ga), greenstone successions (Cassidy et al., 2006). Well-defined lithostratigraphic sequences are restricted to areas in the Kambalda and Ora Banda Domains in the southern Kalgoorlie Terrane (Cassidy et al., 2006). In these areas the Kalgoorlie Terrane is subdivided into three principal lithostratigraphic units: the Kambalda Sequence, the Kalgoorlie Sequence and the Late Basins (Barley et al., 2008). The Kambalda Sequence is dominated by ~2715–2690 Ma komatiite and basalt intercalated with interflow sediments, and ~2710–2690 TTG dacitic volcanic and volcaniclastic rocks (Barley et al., 2008; Kositcin et al., 2008). The conformably overlying Kalgoorlie Sequence is dominated by deep-marine siliciclastic and volcaniclastic sediments deposited between ~2690–2670 Ma, and is in turn unconformably overlain by subaerial volcaniclastic and siliclastic sediments deposited between ~2670 and 2655 (Barley et al., 2008; Krapež et al., 2008; Krapež and Hand, 2008; Squire et al., 2010). This stratigraphy, best constrained around Kambalda, has subsequently formed the model from which other parts of the Eastern Goldfields Superterrane are compared.

In the Agnew district, the supracrustal rocks can be divided into a lower interlayered greenstone pile that consists of fine-grained tholeiitic basalt, high-Mg basalt, komatiite, gabbro and gabbro-pyroxenite-peridotite sills, with minor interbedded sedimentary layers, and an upper clastic-dominated sequence (Platt et al., 1978; Beardsmore, 2002). The lithostratigraphic subdivision and age of deposition of lower greenstone sequence is poorly constrained. The only existing age constraint is a minimum depositional age of 2692 ± 3 Ma, obtained from an interflow sediment near the top of the sequence (Kositcin et al., 2008).

The lower greenstone sequence at Agnew is unconformably overlain by two clastic-dominated packages that formed as two distinct basins separated by the Emu Fault (Fig. 1). The Mount White Syncline consists mainly of the Vivien Formation, which is composed of weakly metamorphosed polymictic conglomerate, fine- to coarse-grained sandstone, chert, basalt and dolerite (Squire et al., 2010; Duuring et al., 2012; Hall et al., 2014) with a maximum depositional age of 2686 ± 7 Ma (Squire et al., 2010). The contact between the sedimentary succession and the Turret Dolerite represents a sheared unconformity (Backhous, 2008). The Scotty Creek Formation to the west comprises a 1500 m-thick sequence of polymictic conglomerate and quartzo-feldspathic sandstones (Platt et al., 1978; Beardsmore, 2002; Duuring et al., 2007) with a maximum depositional age of 2664 ± 5 Ma (Dunphy et al., 2003; Squire et al., 2010). The unconformity between the ultramafic–mafic stratigraphy and the Scotty Creek Formation was reactivated during later deformation to form the Emu Fault (Duuring et al., 2012). The Vivien and Scotty Creek Formations at Agnew correlate, based on detrital zircon and lithological studies, to the Kambalda Domain Black Flag Group and Kurrawang Group, respectively (Squire et al., 2010).

The Kalgoorlie Terrane is dominated by a regional-scale NNW trending structural grain, defined by lineaments and fold axes, interpreted to have resulted from a series of deformation events (Swager, 1997; Weinberg and van der Borgh, 2008; Blewett et al., 2010). In the Agnew district multiple structural models have been proposed (Platt et al., 1978; Beardsmore, 2002; Blewett et al., 2010; Duuring et al., 2012). A commonly used nomenclature is the D1 to D4 event history proposed by Swager (1997), although recent local structural studies have proposed up to 12 local deformation events (e.g., Duuring et al., 2012). Regardless of the structural scheme, the bulk of the deformation recorded in the Agnew District is related to a regional Eastern Goldfields Superterrane-wide E-W contraction, estimated to have occurred ~2660 Ma (D2 after Swager, 1997). Folding to produce the Lawlers Antiform and Mount White Synform was closely linked to intrusion of the 2666 ± 3 Ma Lawlers Tonalite (Fletcher et al., 1988). This pluton, which is composed of quartz diorite to tonalite and granodiorite, is located in the core of the Lawlers Anticline and variably intruded the lower units of the stratigraphy.

3. Chemostratigraphic methods

Mapping and sampling was done during several site visits over two years covering most of the belt (Figs. 2 and 3). We used a lithofacies analysis approach, which has been used with success in other greenstone belts (e.g., Baltazar and Zucchetti, 2007), to reconstruct the volcano-sedimentary evolution of the Agnew belt, and divide the greenstone sequence into 12 lithofacies that are summarised in Table 1. Lithofacies and their relative proportions include: massive basalt (~40%), pillow basalt (5%), dolerite (31%), gabbro (4%), granophyre (<1%), ultrabasic cumulate rocks (9%), spinifex textured komatiite (7%), aphyric komatiite (1%), fragmental komatiite (0.3%), coherent felsic (2%) and fine-grained sedimentary rocks (0.2%). Many of these lithofacies occur in common associations, termed lithofacies associations (Table 2), and include: fine-grained basic (extrusions) (46%), coarse-grained basic-ultrabasic (intrusions) (43%), and spinifex-orthocumulate (komatiite extrusions) (8%). Photographs of key features are presented in Figs. 4 and 5. Lithofacies analysis was necessary for distinguishing intrusions from extrusions, determining relative ages, and reconstructing the paleo-setting. Within this manuscript, basalt, dolerite and gabbro are used as textural terms to describe basic rocks with crystal sizes <2, 2–5 and >5 mm, respectively. Although all samples are metamorphosed to greenschist facies, primary textures are commonly preserved, and the 'meta' prefix has been omitted for brevity. Minerals identified in thin section are mostly products of metamorphism.

Because of textural similarities and the obscuring effects of weathering, metamorphism and alteration, stratigraphic units were largely defined using geochemical characteristics. Geochemical classification diagrams, rare earth element (REE) plots, and bivariate plots of least mobile trace elements were used to separate the greenstone belt into different stratigraphic packages. Stratigraphic relationships were first established on the western limb of the Lawlers Anticline where there is excellent drill core coverage and fewer faults. The stratigraphy was then checked for continuity, primarily through field traverses and geochemical sampling on the eastern limb. Thicknesses reported have been corrected to their true thickness.

A large geochemical dataset ($n = 220$), collected from drill core and the freshest available outcrop, was used in this study. However, characterisation of the different stratigraphic units was largely based on samples collected from the western limb of the anticline from drill core ($n = 79$; Table 4). Samples were crushed after removal of altered and weathered portions. Samples with LOI > 5 wt.% were excluded, with the exception of komatiites. Major element contents were analysed by X-ray fluorescence, while trace elements were analysed by ICP-MS (instrument details are included in Supplementary Appendix A). Normalising factors for trace-element ratios are based on the primitive mantle estimate of McDonough and Sun (1995) and Mg# ($Mg/(Mg + Fe_{TOT})$) are calculated on a molar basis.

4. Litho- and geochemical stratigraphy

The combined lithofacies and geochemical characterisation reveals 11 distinct stratigraphic units (Fig. 2a; Table 3). These

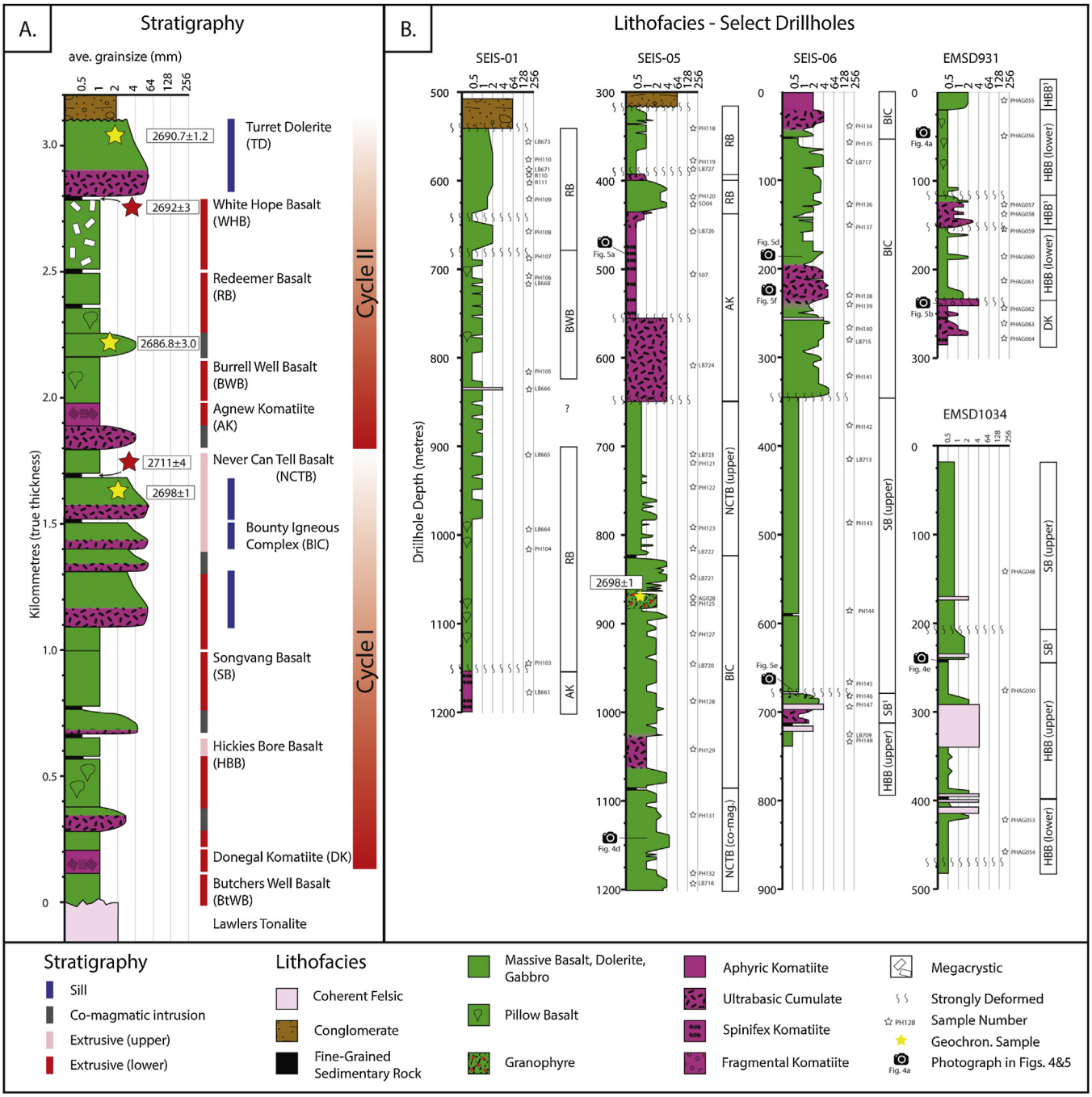

Fig. 2. (A) Summary stratigraphic column showing the variety of lithofacies and their relationship with stratigraphy. Stratigraphy is subdivided into lower and upper cycles. (B) Representative drillholes with locations for samples and photos marked. Stratigraphic abbreviations are from (A) and are based primarily on geochemistry. 1 = comagmatic intrusion.

consist of nine conformable ultramafic–mafic extrusive packages, including several comagmatic intrusions (based on similar geochemistry to hosting extrusive rocks), and two thick mafic sills without genetically associated volcanic rocks. There are also several thin, locally observed felsic intrusions and mudstone intervals. The stratigraphy can be divided into two complete cycles, each of which has a komatiite at its base, while an older enigmatic basalt unit underlies the first cycle. The stratigraphy is not a product of repetition through folding as younging is consistently in the same direction as indicated by pillows, the asymmetry of the spinifex textured komatiite flows, and the positioning of ultrabasic cumulates within mafic sills. Additionally, the sequence is not a product of thrust duplication as several distinctive geochemical and lithological units are not repeated.

Only a few stratigraphic contacts were observed because of poor preservation of outcrops; deformation focussed along the contacts; and lack of obvious differences in appearance between the basalt types such that many contacts were only revealed through geochemistry (e.g., the Redeemer and Burrell Well basalts). On the other hand, several of the extrusive units are separated by thin mudstone intervals (e.g., the Hickies Bore and Songvang basalts). In the absence of clear evidence for unconformities between units (e.g., conglomerates and/or angular relationships with overlying stratigraphy), contacts for these units are interpreted as

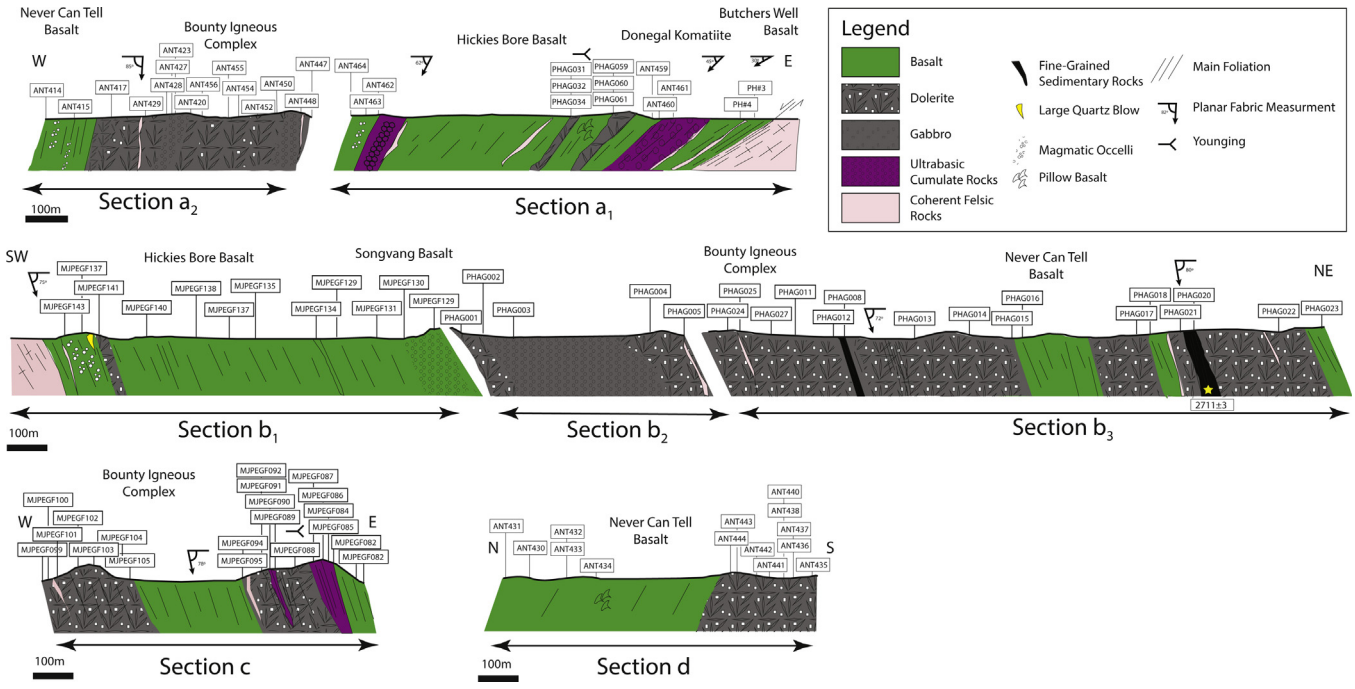

Fig. 3. Field traverses lithofacies map. Location of traverses indicated in Fig. 1(A). Stratigraphic subdivisions are based primarily on geochemistry.

being conformable. Intrusive contacts are interpreted for the Turret Dolerite, Bounty Igneous Complex and numerous comagmatic intrusions, all of which have sharp chilled margins with their hosts. The top of the ultramafic–mafic stratigraphy is marked by overlying conglomerates that contain clasts from the underlying stratigraphy and the contact is interpreted as an erosional unconformity. On the east limb the Lawlers Anticline the Turret Dolerite is unconformably overlain by the Mosquito Well Conglomerate of the Vivien Formation, whereas on the west limb the Agnew Komatiite, Redeemer Basalt and Burrell Well Basalt are unconformably overlain by the Claudius Member of the Scotty Creek Formation.

Stratigraphic thickness changes are evident across the Lawlers Anticline, with thinner greenstones rocks on the western limb (~3.1 km) in comparison to the eastern limb and hinge (~7 km, but poorly constrained). This difference is in part reflected by the absence of the White Hope Basalt and Turret Dolerite on the west limb of the anticline, where they have been eroded. This interpretation is supported by the provenance of clasts derived from overlying conglomeratic units above the sequence on the west limb, although some of this loss of the upper stratigraphy may also be a result of shearing along the Emu Fault (Nyga, 2011; Whitworth, 2012).

There is wide compositional variability for the data (Figs. 6–10). On a Jensen diagram, samples plot mostly as komatiites, komatiitic basalts and high-Mg and high-Fe tholeiites (Fig. 6a) and the data fall along the tholeiitic trend towards extreme iron enrichment (Fig. 6b). Thorium-titanium ratios, after Barnes et al. (2012), define low-, intermediate- and high-Th basaltic groups (Fig. 6c), whereas the large range of Mg# (10–90) and major element trends suggest crystal fractionation is significant (Fig. 7). However, REE plots are most useful for distinguishing different stratigraphic units (Fig. 8). A subset of the geochemical data (Fig. 9a), collected mainly from four drillholes (sample locations in Fig. 2b) where there is excellent control on the relative age of each sample, demonstrates the compositional variations through time for the full section as well as for individual stratigraphic units. Similar trends are observed when the full geochemical dataset is used (Fig. 9b).

The lithofacies, stratigraphic units, their characteristics, emplacement origins and setting are briefly summarised below (Figs. 2–10).

4.1. Mudstone, siltstone and chert: paleoenvironmental setting

Several thin intervals (0.2–4.1 m), averaging 0.3 m thick, of mudstone occur throughout the ultramafic–mafic stratigraphy. Mudstones are grey to black, finely bedded and sulphidic. One light-coloured siltstone layer, sampled for geochronology (Section 6.2), occurs within the Never Can Tell Basalt. Several light coloured massive cherty intervals are also found, commonly intercalated with mudstones. Sediments are in sharp contact with the host sequence and breccias are absent. Contact between mudstones and cherts range from gradational to sharp. Bedding, particularly in the thicker intervals, is often chaotically folded.

The absence of symmetrical ripples indicates deposition below wave base from suspension fallout (Clifton and Dingler, 1984; Boggs, 1987) or nepheloid layers (Pak et al., 1980). Black mudstone with abundant sulphides indicates anoxic-sulphidic conditions prevailed (Werne et al., 2002). The siltstone layer contains abundant euhedral zircons and is interpreted as an airfall tuff sourced from a distal pyroclastic eruption, similar to interpretations for other similar Archean sediments (e.g., Claoue-Long et al., 1988). The cherts with gradational contacts to mudstones are interpreted as silica-replacement of a mudstone protolith (S-cherts), whereas cherts with sharp contacts may either represent S-cherts or chemical precipitation on the sea floor (C-cherts) (Van Kranendonk, 2006; van den Boorn et al., 2007). The presence of intercalated intervals of mudstones and cherts indicates the paleoenvironment was subaqueous, below wave base, and far from any landmass.

4.2. Ultramafic–mafic extrusive rocks and comagmatic intrusions

Extrusive rocks and comagmatic intrusions make up the bulk of the stratigraphy, consisting mainly of flows of basalt, komatiitic basalt and komatiite, with lesser coarser-grained intrusions of

Table 1
Description and interpretation of lithofacies.

Lithofacies	Description	Interpretation
Pillow basalt	Volcanic rock forming intervals typically ~10 m thick, consisting of clusters of pillows. Individual pillows are ~50 cm across, have aphyric to fine-grained cores, often with abundant amygdales at core margins and with well defined aphyric chilled margins (<1 cm thick). The interpillow space consists of calcite, and in rare cases, hyaloclastite	Subaqueous, extrusive basalts, indicate lower magma flow rates than for sheet flows (White et al., 2009; Fink and Griffiths, 1992; Griffiths and Fink, 1992)
Massive basalt	Coherent volcanic rock, massive aphyric to fine-grained basalt, up to 150 m thick. Ranges from pale to dark green. Some intervals organised into massive fine-grained intervals (5–20 m thick) that are separated by thin aphyric intervals. Plagioclase and alkali-feldspar porphyritic in places (5–20 mm), variolitic in places, generally non-vesicular	Thick intervals of massive basalt that is not gradational into gabbro or other coarse-grained textures or granophyres, are interpreted as pahoehoe lava sheet flows. Lack evidence for apophyses into overlying strata. Indicates relatively high extrusion rates (Fink and Griffiths, 1992; Griffiths and Fink, 1992)
Dolerite	Coherent mafic volcanic rock, generally massive and uniform, with crystals of plagioclase and pyroxene (replaced by hornblende and/or chlorite) 2–5 mm. Gradational into basalt and gabbro LF	When gradational into coarser-grained lithofacies (gabbro, ultrabasic cumulate), interpreted as part of mafic intrusion. When gradational into massive basalt without associated gabbros or other coarse-grained rocks and without evidence for apophyses into overlying sequence, interperted as interior of sheet flows
Gabbro	Coherent mafic volcanic rock, generally massive and uniform, with crystals >5 mm. Generally consists of plagioclase and pyroxene (largely replaced by hornblende). Gradational into dolerite and ultrabasic cumulate LF	Slow cooled interior of mafic intrusion
Granophyre	Coherent felsic dykes and veins with gradational or sharp contacts with dolerite or gabbro host. Consists of plagioclase, alkali-feldspar and quartz with distinctive intergrowth textures. Generally <10 cm thick, rare thicker (>5 m) intervals	Late differentiation products (felsic component) of cooling mafic magma
Spinifex	Coherent volcanic rock, dark-coloured, ranging from fine-grained random spinifex (crystals generally < 5 mm) to coarse bladed spinifex (up to 50 cm long crystals)	Always found in association with aphyric komatiite and ultrabasic cumulate LF. Interpreted as A2 (random spinifex) and A3 (bladed/platy-spinifex) divisions of komatiitic lavas, as defined by Pyke et al. (1973)
Aphyric Komatiite	Coherent volcanic rock, dark-coloured, aphyric, often altered to serpentine, talc and/or carbonate. Associated with spinifex and ultrabasic cumulate LF	Interpreted as A1 division of komatiitic lavas, as defined by Pyke et al. (1973)
Ultrabasic Cumulate	Coherent volcanic rock, dark-coloured with cumulate textures, ranging from orthocumulate, mesocumulate to adcumulate, consisting of olivine crystals (commonly replaced by serpentine, magnetite, talc and/or carbonate). Found in assocation with either: spinifex and aphyric komatiite LF; or gabbro and/or dolerite LF. Crystal sizes range from <1 mm to ~1 cm	When found as thin intervals in association with spinifex and aphyric komatiite, interpreted as B2-B4 divisions of komatiite lava flows (Pyke et al., 1973). Thicker intervals not in direct assocation with spinifex or aphyric komatiite many be either cumulates associated with intrusions (e.g., Rosengren et al., 2008) or extrusions (e.g., Gole et al., 2013), however, clear evidence (op. cit.) to distinguish intrusive from extrusive komatiites is not preserved. When gradational into mafic rocks (gabbro and dolerite), interpreted as part of differentiated base of mafic intrusion
Fragmental Komatiite	Clast-supported highly deformed breccia-conglomerate with clasts of komatiite in an altered talc-carbonate matrix. In most cases individual clasts are difficult to make out due to deformation and alteration, but where discernible, they often have whispy margins. Gradational with aphyric komatiite	Gradational contacts into aphyric komatiite, absence of undeformed fragmental komatiites in region and whispy clast margins, support origin as cataclasite
Coherent Felsic	Coherent felsic rock, generally massive with porphyritic texture; sharp contacts with host. Thickness from 0.5 to 25 m. Breccias absent	Felsic intrusions (dykes and sills) into lithified crust
Fine-Grained Sediment	Thin intervals (0.2–4.1 m), avergaing 0.3 m thick. Grey to black, finely bedded and sulphidic, with lesser light coloured massive siltstone and cherty intervals. Seven different intervals are known	Subaqueous deposition, below wave base, and far from any landmass. The siltstone, based on the zircon population, is interpreted as an air-fall deposit from a distal felsic source

Table 2
Description and interpretation of Lithofacies associations.

Lithofacies association	Description	Interpretation
Spinifex-Orthocumulate	Asymmetric packages (~1 m thick) of aphyric and spinifex komatiite and ultrabasic cumulate, with sharp top and bottom contacts. Spinifex zones display consistent assymetry, grading from fine-grained random spinifex into bladed spinifex (useful for younging). Individual packages form stacked sequences up to ~100 m thickness	Stacked sequence of komatiite flow lobes (Hill et al., 1995). The repeating textural variations display many of the features of archetypal komatiite flows as defined by (Pyke et al., 1973). Primary flow top breccias not developed
Fine-grained basic	Dominated by gradational interdigitating pillow and massive basalt that are ~10– > 300 m thick. Sharp contacts with other lithofacies. In some cases massive basalt grades into dolerite. Coarser textures absent	Extrusive basaltic lava flows
Coarse-grained basic-ultrabasic	Association of mainly of dolerite and gabbro, with coarser grainsizes generally towards the centre of the body (ranging from 3 to 130 m thick). In some cases these lithofacies are also associated with ultrabasic cumulates and granophyres (total thickness ranging from 30 to 300 m thick). Internal contacts are generally gradational and, including gradational changes into basalt at the margins, which are in sharp contact with the host. Never gradational into pillow basalts	Mafic sills with chilled margins. Associations of basalt, dolerite and gabbro interpreted as undifferentiated to weakly differentiated sills; associations that also include ultrabasic cumulates and granophyres interpreted as differentiated mafic sills

Table 3
Summary of physical and compositional characteristics of the Agnew mafic-ultramafic stratigraphy.

White Hope Basalt (WHB)	**Thickness and distribution:** Total thickness ~300 m. Occurs in the Mt White syncline, observed in two drillholes and in the field, absent on the Western limb of the anticline **Descriptions and interpretations**: Consists of massive megacrystic basalt with 4–20 mm alkali feldspar crystals (~10–20 vol.%) as separate grains or glomerocrysts. Groundmass mineralogy of Pl-Hbl-Opq. Submarine sheet flows **Geochemistry:** Low-Th; cab,caa; Mg# = 40–52, 46; [La/Sm] = 0.8–1.9, 1.2; [Gd/Yb] = 1.0–1.5, 1.1
Redeemer Basalt (RB)	**Thickness and distribution:** 100–405 m thick. Fine-grained basic LFA = 70–280 m, Coarse-grained basic–ultabasic LFA = 30–125 m. Observed in many drillholes on Western limb of anticline and in outcrop in the Mt White Syncline **Descriptions and interpretations:** Divided into fine-gained basic (pillow and sheet flows) and coarse-grained basic-ultrabasic (sub-volcanic intrusions). The basalt is dark-coloured and texturally indistinguishable from the BWB. Microspinifex and cumulate textures occur in the groundmass, mineralogy includes Hbl, Srp, Chl and Tlc (Mg-rich samples), and Pl, Hbl and Qz (Mg-poor samples). Includes two thin mudstone intervals. Submarine pillow and sheet flows and comagmatic intrusions **Geochemistry:** Int-Th; kb, hmth; Mg# = 47–74, 64; [La/Sm] = 1.2–1.8, 1.4; [Gd/Yb] = 0.9–1.2, 1.0
Burrell Well Basalt (BWB)	**Thickness and distribution:** Total thickness ~200 m. Occurs sporadically on western limb, common in the Mt White Syncline **Descriptions and interpretations:** Fine-grained basic (massive and pillow (~5%) LF). Texturally indistinguishable from the RB. The RB and BWB often have an interdigitating relationship. Microspinifex and olivine cumulate textures occur in the groundmass, which consists of Hbl, Srp, Chl, Tlc and Opq. Submarine pillow and sheet flows **Geochemistry:** Low-Th; kb, hmth; Mg# = 52–76, 64; [La/Sm] = 0.6–1.2, 0.9; [Gd/Yb] = 0.8–1.2, 1.0
Agnew Komatiite (AK)	**Thickness and distribution:** Roughly 100 m thick. Spinifex dominated upper half (~50 m), cumulate lower half (~50 m), and fragmental komatiite (<8 m). AK observed in many drillholes on Western limb of anticline, in outcrop in Mt White Syncline **Descriptions and interpretations:** Upper half consists of spinifex-orthocumulate LFA (komatiitic sheet flows, each ~1 m thick), while the lower half consists of massive ultrabasic cumulate (intrusion?), including abundant adcumulate textures. Fragmental Komatiite commonly at top contact. Mineralogy consists of Tlc, Srp, Cb and Opq. Subaqueous komatiite flows (and comagmatic intrusion?); fragmental komatiite interpreted as cataclasite **Geochemistry:** k; Mg# = 76–93, 86; [La/Sm] = 0.3–3.8, 1.2; [Gd/Yb] = 0.3–1.7, 0.8
Never Can Tell Basalt (NCTB)	**Thickness and distribution:** ~300 m thick. Upper basalt (~150 m), middle intrusion (~100 m) and lower basalt (~50 m). Observed in several drillholes on the Western limb, and sporodically in outcrop across the property **Descriptions and interpretations:** Divided into upper, middle and lower sections. The upper section consists of massive basalt (minor dolerite); middle section is dominated by the coarse-grained basic-ultabasic LFA (dolerite and gabbro LF, with only minor basalt LF); and the lower section consists of massive basalt (feldspar phyric). The NCTB is intruded by several sills of the BIC. The mineralogy consists of Hbl, Qz and Pl. Includes several thin mudstone intervals. Submarine sheet flows (upper and lower basalts) and comagmatic intrusion (middle) **Geochemistry:** Int-Th; hfth; Mg# = 12–74, 37; Fe_2O_3 = 11–20, 15.5; TiO_2 (~> 1.25); [La/Sm] = 0.9–2.0, 1.3; [Gd/Yb] = 1.0–1.4, 1.2
Songvang Basalt (SB)	**Thickness and distribution:** ~335 m thick (upper SV = 225 m; lower SV = 110 m). Observed in several drillholes on the Western limb, and sporodically in outcrop across the property **Descriptions and interpretations:** Consists of an upper massive basalt and a lower coarse-grained basic-ultrabasic LFA (dolerite, gabbro, ultrabasic cumulate and minor basalt). The upper SV contains Chl-altered porphyroclasts (3 mm) in a groundmass of Hbl, Qz and Fld. The lower SV contains microspinifex texture and an altered groundmass mostly of Tlc, Srp and Opq. Includes one thin mudstone near the base of the upper SV. Submarine sheet flows and comagmatic differentiated intrusion **Geochemistry:** High-Th; k, kb, hmth; Mg# = 40–84, 68; Zr/Th = 25–50; [La/Sm] = 1.1–4.3, 1.8; [Gd/Yb] = 0.9–1.8, 1.1
Hickies Bore Basalt (HBB)	**Thickness and distribution:** 525 m thick (upper HBB = 85 m; lower HBB = 350 m, intrusions = 5–100 m). Top and bottom observed in several drillholes on the Western limb, and the HBB is observed sporodically in outcrop across the property **Descriptions and interpretations:** Upper HBB consists of massive basalt; Lower HBB consists of massive and pillow basalt (amygdaloidal in places), including coarse-grained basic-ultrabasic LFA (dolerite, gabbro, as well as ultrabasic cumulate and basalt). Basalts consist of Hbl and Qz, while the Coarse-Grained LFA consists of Hbl, Qz, Fld, Srp and Tlc. Submarine pillow and sheet flows and differentiated comagmatic intrusions **Geochemistry:** Low-Th; hfth, hmth; Mg# = 43–68, 55; [La/Sm] = 0.7–3.8, 1.1; [Gd/Yb] = 0.9–1.9, 1.1
Donegal Komatiite (DK)	**Thickness and distribution:** ~100 m thick. Top ~50 m observed in two drillholes and sporadic exposures on the Western limb **Descriptions and interpretations:** Consists of spinifex-orthocumulate LFA (aphyric komatiite (20%), spinifex komatiite (30%) and ultrabasic cumulate (30%), and lesser fragmental komatiite (10%) at the top. Mineralogy consists of Tlc, Srp, Cb and Opq. Subaqueous spinifex flows and cataclasites (fragmental komatiite) at top where deformation is concentrated **Geochemistry:** k; Mg# = 83–85, 84; [La/Sm] = 0.5–0.8, 0.6; [Gd/Yb] = 0.8–0.9, 0.9
Butchers Well Basalt (BtWB)	**Thickness and distribution:** >100 m thick? Only occurs in sporadic outcrops on Western limb. Intruded at base by granite **Descriptions and interpretations:** Massive basalt. Mineralogy consists of Hbl, Qz, Pl, Mus and Chl. Submarine sheet flows? **Geochemistry:** td, hfth; Mg# = 20–34, 27; [La/Sm] =0.7–1.0, 0.8; [Gd/Yb] = 1.0
Turret Dolerite (TD)	**Thickness and distribution:** Total thickness = 300 m. Observed in several drillholes on the E limb. Not found on the W limb **Descriptions and interpretations:** Consists of coarse-grained basic-ultrabasic LFA (dolerite, gabbro, cumulate ultrabasic LF and rare basalt and granophyre LF). Includes granophyric groundmass and variable mineralogy of mainly Hbl, Pl, Chl and Opq (+/-Tlc and Srp). Differentiated Sill **Geochemistry:** High-Th; hmth; Mg# = 25–82, 57; Zr/Th = 21–25; [La/Sm] = 2.2–2.9, 2.6; [Gd/Yb] = 1.1–1.3, 1.2
Bounty Igneous Complex (BIC)	**Thickness and distribution:** Total thickness = ~500 m. Upper sill (225 m), middle sill (>40 m) and lower sill (250 m). Observed in several drillholes on the Western limb, and sporodically in outcrop across the property **Descriptions and interpretations:** Consists of three sills of the coarse-grained basic-ultrabasic LFA (dolerite, gabbro, cumulate ultrabasic LF and minor basalt and granophyre LF). Mineralogy varies, but includes Hbl, Qz, Pl, Chl, Ca and Opq. Has chilled margins with NCTB. Differentiated Sills **Geochemistry:** Low-Th; hmth; Mg# = 11–81, 59; [La/Sm] = 0.7–2.7, 1.3; [Gd/Yb] = 0.9–1.4-0.8

Pl, plagioclase; Cpx, clinopyroxene; Opq, opaques; Fld, feldspar; Hbl, hornblende; Srp, serpentine; Tlc, talc; Ca, carbonate; and Qz, quartz. Geochemistry values displayed as range and average. Low-Th, int-Th and high-Th (see Fig. 6c). cab, calc-alkaline basalt; caa, calc-alkaline andesite, kb, komatiitic basalt; hmth, high-Mg tholeiite; hfth, high-iron tholeiite, td, tholeiitic dacite (see Fig. 6a).

Table 4
Major and trace elements of representative samples of the Agnew ultramafic–mafic suite.

Formation Method Unit	SampleID	Drillhole[A]	DepthFrom[B]	Lithology	SiO_2 XRF %	Al_2O_3 XRF %	TiO_2 XRF %	MgO XRF %	Fe_2O_3 XRF %	CaO XRF %	Na_2O XRF %	K_2O XRF %	P_2O_5 XRF %	MnO XRF %	LOI GRAV %	S XRF %	Total
Vivien Dolerite	VO 02	VVDD170A	220.50	Dolerite	54.16	15.59	0.56	6.13	11.24	9.58	2.02	0.47	0.05	0.18	2.27	0.01	99.92
Vivien Dolerite	VO 04	VVDD170A	267.00	Dolerite	50.70	15.39	0.43	8.17	11.63	11.92	1.42	0.13	0.03	0.18	1.60	0.01	99.54
Vivien Dolerite	VO 10	VVDD182	251.00	Dolerite	52.65	15.55	0.55	6.92	10.91	11.63	1.36	0.21	0.05	0.18	1.30	0.01	99.77
Vivien Dolerite	VO 35	VVDD199	134.10	Dolerite	52.01	15.35	0.83	5.32	14.06	9.87	2.06	0.25	0.07	0.18	1.92	0.01	99.81
Vivien Dolerite	VO 55	VVDD200	318.00	Dolerite	54.23	15.35	0.56	6.63	10.62	9.52	2.46	0.39	0.07	0.16	2.79	0.01	100.17
Vivien Dolerite	VO 24	VVDD201	135.20	Dolerite	50.21	21.83	0.32	6.14	6.05	13.98	1.20	0.15	0.03	0.09	2.26	0.01	100.06
Vivien Dolerite	VO 51	VVDD202	158.50	Dolerite	55.86	12.42	0.98	6.79	8.78	14.29	0.59	0.07	0.08	0.13	3.89	0.06	99.96
Vivien Dolerite	VO 52	VVDD202	165.00	Dolerite	56.00	8.35	0.58	11.38	10.40	12.64	0.30	0.07	0.06	0.21	2.03	0.01	99.54
White Hope Basalt	RF#25	EMSD 887	340.20	Basalt (megacrystic)	49.89	18.12	1.39	3.92	11.76	11.29	2.87	0.48	0.12	0.16	1.33	0.11	100.00
White Hope Basalt	TW 02	EMSD441	127.70	Basalt (megacrystic)	52.28	18.48	0.98	3.57	9.92	11.60	2.71	0.22	0.08	0.16	4.93	0.10	99.71
White Hope Basalt	RF#34	EMSD845	294.35	Basalt (megacrystic)	50.12	18.61	0.94	5.13	10.91	10.03	3.22	0.72	0.08	0.23	1.75	0.14	100.00
White Hope Basalt	RF#87	EMSD919	275.60	Basalt (megacrystic)	49.41	23.00	1.13	5.68	11.54	3.14	5.72	0.20	0.08	0.10	3.54		100.00
Redeemer Basalt	AW024	EMSD1038	482.00	Basalt (massive)	49.06	15.50	0.76	11.28	12.08	8.85	2.13	0.07	0.08	0.19	2.70	0.02	99.41
Redeemer Basalt	UB3	EMSD242B	348.50	Basalt (massive)	54.69	15.98	0.80	6.57	9.35	9.73	2.40	0.17	0.10	0.20	0.84	0.01	100.38
Redeemer Basalt	UB1	EMSD398	144.70	Basalt (pillowed)	51.73	13.20	0.50	12.79	10.31	8.33	2.85	0.07	0.05	0.17	2.56	0.01	99.30
Redeemer Basalt	PH110	SEIS01	568.00	Dolerite	53.66	14.82	0.99	6.49	12.29	8.55	2.63	0.25	0.12	0.19	1.21		100.95
Redeemer Basalt	R 110	SEIS01	587.80	Dolerite	50.60	18.27	0.50	9.30	9.77	7.82	3.27	0.26	0.06	0.14	2.64		99.78
Redeemer Basalt	R 111	SEIS01	598.50	Dolerite	51.60	16.48	0.58	8.97	9.09	9.70	2.94	0.42	0.06	0.16	1.91	0.02	100.09
Redeemer Basalt	PH108	SEIS01	654.00	Dolerite	50.70	17.89	0.56	8.87	9.08	9.53	2.88	0.27	0.05	0.16	1.61		100.95
Redeemer Basalt	PH104	SEIS01	1017.30	Basalt (pillowed)	49.54	11.54	0.46	13.49	11.39	11.81	1.45	0.08	0.04	0.20	1.21		100.58
Redeemer Basalt	PH118	SEIS05	335.50	Basalt (massive)	50.18	15.37	1.44	6.32	14.39	9.89	1.87	0.23	0.14	0.17	0.63	0.05	99.91
Redeemer Basalt	PH119	SEIS05	383.00	Basalt (massive)	49.90	13.23	0.56	11.91	12.62	9.46	1.89	0.14	0.05	0.24	1.86	0.02	99.58
Redeemer Basalt	PH120	SEIS05	416.00	Dolerite	42.12	19.42	0.73	10.61	14.75	10.32	1.31	0.44	0.06	0.22	3.06	0.01	99.73
Redeemer Basalt	SO 04	SEIS05	421.70	Gabbro	52.20	17.23	0.52	7.50	9.08	10.49	2.60	0.19	0.05	0.14	1.13	0.01	99.94
Burrell Basalt	MN006	EMSD1066W6	892.50	Basalt (massive)	49.36	12.87	0.74	12.67	12.97	8.56	2.49	0.07	0.08	0.17	1.63	0.05	100.40
Burrell Basalt	UB4	EMSD222	122.60	Basalt (massive)	48.59	15.47	1.10	7.61	13.80	10.26	2.73	0.16	0.08	0.20	0.76	0.02	99.04
Burrell Basalt	AW059	EMSD913	631.00	Dolerite	49.72	18.69	0.94	5.66	10.39	11.62	2.64	0.13	0.07	0.14	1.13	0.03	99.63
Burrell Basalt	MN360	EMSD939	331.10	Basalt (massive)	47.16	10.67	0.59	18.72	14.01	8.10	0.38	0.15	0.03	0.20	3.61	0.02	99.30
Burrell Basalt	MN239	EMSD939	361.30	Basalt (massive)	49.79	11.57	0.69	15.08	13.53	8.19	0.86	0.06	0.02	0.21	2.69	0.03	99.50
Burrell Basalt	PH107	SEIS01	681.30	Basalt (massive)	50.14	13.74	0.52	11.40	10.94	10.99	1.96	0.09	0.05	0.17	1.71	0.02	99.75
Burrell Basalt	PH106	SEIS01	721.00	Basalt (pillowed)	50.24	14.74	0.57	10.47	10.96	10.58	2.09	0.10	0.05	0.20	1.36		100.96
Burrell Basalt	MN128	WDU1167	180.60	Basalt (massive)	46.17	10.38	0.59	20.80	13.16	8.01	0.62	0.05	0.04	0.16	4.78		99.00
Agnew Komatiite	MN178	ED145	265.00	Komatiite (spinifex)	46.47	5.59	0.35	30.67	10.72	6.01	0.05		0.02	0.12	13.20	0.07	99.90
Agnew Komatiite	MN163	ED147	300.40	Komatiite (spinifex)	44.71	8.17	0.45	26.32	13.77	5.99	0.36	0.01	0.03	0.18	9.10	0.07	99.80
Agnew Komatiite	AW020	EMSD767	422.70	Komatiite (spinifex)	42.67	10.48	0.56	26.12	15.05	4.67	0.20	0.01	0.08	0.15	7.72	0.44	99.34
Agnew Komatiite	SO 07	SEIS05	508.20	Komatiite (spinifex)	42.88	7.47	0.49	27.26	17.29	4.37	0.01	0.03	0.03	0.15	6.93	0.01	99.93
Bounty Igneous Complex	PHAG039	EMSD1032	79.00	Basalt	47.87	10.90	0.67	14.85	12.86	11.20	1.14	0.31	0.05	0.15	1.47		100.32
Bounty Igneous Complex	PHAG040	EMSD1032	120.80	Basalt	47.57	11.24	0.63	14.65	12.74	11.70	1.11	0.10	0.05	0.21	1.34		100.56
Bounty Igneous Complex	PHAG041	EMSD1032	136.00	Basalt	48.38	9.93	0.62	14.99	12.67	12.03	0.97	0.16	0.04	0.20	1.03		100.32
Bounty Igneous Complex	PHAG043	EMSD1032	218.00	Ultrabasic cumulate	50.14	15.67	0.49	9.15	8.50	13.56	1.97	0.34	0.03	0.15	0.86		100.98
Bounty Igneous Complex	PHAG044	EMSD1032	306.80	Basalt (chilled margin)	48.46	10.91	0.61	16.72	13.34	8.63	0.84	0.24	0.05	0.20	2.65		100.27
Bounty Igneous Complex	PH125	SEIS05	877.30	Granophyre	56.54	11.95	1.51	1.22	18.83	6.26	2.92	0.23	0.30	0.24	1.45		100.06
Bounty Igneous Complex	PH128	SEIS05	989.60	Dolerite	48.56	20.22	0.57	6.39	7.79	14.35	1.84	0.13	0.04	0.11	0.63	0.01	99.89
Bounty Igneous Complex	PH129	SEIS05	1040.00	Ultrabasic cumulate	43.67	13.90	0.37	18.06	14.46	8.56	0.68	0.07	0.03	0.20	4.31		99.93
Bounty Igneous Complex	PH135	SEIS06	64.00	Basalt (massive)	52.36	13.93	0.88	7.83	11.15	9.99	3.32	0.34	0.07	0.13	1.70	0.01	100.20
Bounty Igneous Complex	PH136	SEIS06	126.80	Dolerite	52.67	13.21	1.30	4.53	16.75	8.95	2.13	0.14	0.09	0.23	1.30		100.06
Bounty Igneous Complex	PH137	SEIS06	156.50	Dolerite	50.80	16.99	0.49	8.09	7.80	13.38	2.12	0.16	0.03	0.13	1.35	0.03	99.94
Bounty Igneous Complex	PH140	SEIS06	271.20	Dolerite	50.22	14.64	1.65	6.51	14.14	9.64	2.68	0.14	0.16	0.22	0.56	0.01	99.64
Bounty Igneous Complex	PH141	SEIS06	321.00	Ultrabasic cumulate	49.51	17.37	1.11	6.01	11.36	11.45	2.76	0.15	0.10	0.18	0.64	0.02	100.12
Never Can Tell Basalt	PHAG045	EMSD1032	322.20	Basalt (massive)	48.82	15.45	1.46	5.95	14.47	10.17	3.14	0.18	0.14	0.22	0.48	0.02	101.00
Never Can Tell Basalt	LB3	EMSD133	279.80	Basalt (massive)	47.63	14.75	1.55	5.38	17.20	10.15	2.69	0.27	0.14	0.24	0.81	0.02	100.12

Never Can Tell Basalt	LB5	EMSD156	239.00	Basalt (massive)	49.71	14.69	1.53	5.81	15.05	10.04	2.52	0.27	0.14	0.23	0.33	0.02	99.14
Never Can Tell Basalt	LB6	EMSD222	321.50	Basalt (massive)	51.25	14.03	1.45	6.09	14.11	9.11	3.31	0.27	0.13	0.24	0.36	0.01	100.25
Never Can Tell Basalt	LGU1	EMSD223	272.50	Basalt (massive)	48.90	14.84	1.56	6.35	16.74	9.15	1.85	0.31	0.13	0.18	1.86	0.02	98.98
Never Can Tell Basalt	LB7 A	EMSD242B	479.70	Basalt (massive)	48.70	15.26	1.30	5.98	15.38	9.21	2.87	0.94	0.13	0.22	1.22	0.01	100.23
Never Can Tell Basalt	LB1	EMSD398	387.90	Basalt (massive)	50.82	14.91	1.56	5.39	15.97	8.68	1.68	0.61	0.15	0.22	1.26	0.01	99.80
Never Can Tell Basalt	R 165	EMSD446	1168.00	Basalt (massive)	49.33	13.68	2.05	4.01	20.44	8.21	1.57	0.27	0.21	0.23	0.93	0.05	99.83
Never Can Tell Basalt	R 164	EMSD446	1171.00	Basalt (massive)	51.92	12.81	2.08	5.02	18.25	6.71	2.48	0.28	0.18	0.26	0.35	0.01	100.33
Never Can Tell Basalt	LB4	EMSD609	149.50	Basalt (massive)	47.10	15.81	1.64	6.01	14.86	11.15	2.87	0.25	0.15	0.16	0.61	0.01	99.94
Never Can Tell Basalt	PH121	SEIS05	722.20	Basalt (massive)	50.47	14.13	1.48	5.19	15.40	9.57	3.14	0.29	0.13	0.20	0.46	0.03	99.96
Never Can Tell Basalt	PH123	SEIS05	793.50	Basalt (massive)	49.84	14.41	1.47	5.74	15.42	9.20	3.26	0.30	0.13	0.23	0.42		100.02
Never Can Tell Basalt	PH131	SEIS05	1119.00	Dolerite	52.90	13.30	2.00	4.55	16.06	7.46	2.82	0.31	0.39	0.21	0.70	0.01	100.14
Never Can Tell Basalt	PH132	SEIS05	1183.10	Dolerite	52.31	14.48	1.81	4.32	14.35	8.55	3.32	0.29	0.35	0.20	0.75	0.02	100.05
Songvang Basalt	PHAG048	EMSD1034	141.80	Basalt (massive)	49.83	9.96	0.52	17.09	11.94	9.19	0.97	0.28	0.04	0.18	2.29	0.03	99.74
Songvang Basalt	PH142	SEIS06	377.25	Basalt (massive)	48.66	8.92	0.48	16.25	11.96	12.16	1.23	0.09	0.04	0.21	1.55		99.34
Songvang Basalt	PH143	SEIS06	482.25	Basalt (massive)	49.79	9.51	0.54	18.35	11.82	8.31	1.06	0.40	0.05	0.18	3.14	0.02	99.67
Songvang Basalt	PH144	SEIS06	584.00	Basalt (massive)	53.84	14.27	0.70	6.73	11.49	10.31	2.10	0.32	0.06	0.17	0.55	0.01	100.10
Songvang Basalt	PH145	SEIS06	667.00	Basalt (massive)	54.05	12.62	0.65	10.25	9.19	10.09	2.88	0.09	0.04	0.14	0.54	0.01	99.79
Songvang Basalt	PH146	SEIS06	682.00	Ultrabasic cumulate	48.94	7.07	0.40	25.02	12.44	5.82	0.06	0.01	0.03	0.20	5.37	0.03	100.00
Hickies Bore Basalt	PHAG050	EMSD1034	275.10	Basalt (massive)	49.44	14.47	1.26	6.90	14.41	10.63	2.34	0.23	0.11	0.21	0.37	0.02	100.82
Hickies Bore Basalt	PHAG053	EMSD1034	425.30	Basalt (massive)	49.51	13.02	0.72	8.04	11.93	14.28	1.90	0.29	0.06	0.25	0.50		100.96
Hickies Bore Basalt	PHAG031	EMSD929	107.50	Basalt (pillowed)	52.46	13.95	0.74	7.41	10.76	11.69	2.61	0.13	0.06	0.20	0.46	0.05	100.98
Hickies Bore Basalt	PHAG056	EMSD931	49.00	Basalt (pillowed)	51.70	12.74	0.68	8.91	11.68	12.76	1.01	0.26	0.05	0.20	0.79		100.62
Hickies Bore Basalt	PH148	SEIS06	731.80	Basalt (massive)	50.69	14.91	1.29	5.28	13.83	10.63	2.86	0.17	0.11	0.22	0.55	0.02	100.25
Donegal Komatiite	PHAG062	EMSD931	239.60	Komatiite (aphyric)	47.45	6.94	0.30	28.51	10.81	5.66	0.10		0.02	0.20	8.01	0.28	100.02
Donegal Komatiite	PHAG063	EMSD931	261.00	Ultrabasic cumulate	46.09	6.86	0.29	28.34	11.53	6.30	0.40	0.01	0.02	0.17	5.43	0.09	100.00
Donegal Komatiite	PHAG064	EMSD931	270.70	Komatiite (aphyric)	48.17	7.22	0.30	27.01	9.55	7.13	0.47	0.02	0.01	0.12	5.72	0.09	99.87
Butchers Basalt	PH#3	254883	6888515	Basalt (massive)	60.00	12.02	0.29	2.19	17.19	4.60	1.41	0.64	0.48	0.20	3.79	0.07	100.00
Butchers Basalt	PH#4	254764	6888566	Basalt (massive)	76.10	11.27	0.39	1.29	4.88	2.12	2.61	1.24	0.04	0.06	1.12	0.04	100.00

SampleID	Ba ICPMS ppm	Be ICPMS ppm	Co ICPMS ppm	Cr ICPMS ppm	Cs ICPMS ppm	Cu ICPMS ppm	Ga ICPMS ppm	Hf ICPMS ppm	Li ICPMS ppm	Mo ICPMS ppm	Nb ICPMS ppm	Ni ICPMS ppm	Pb ICPMS ppm	Rb ICPMS ppm	Sb ICPMS ppm	Sc ICPMS ppm	Sn ICPMS ppm	Sr ICPMS ppm	Ta ICPMS ppm	Th ICPMS ppm
VO 02	109.0		57	42	0.64	21	15.5	1.39		0.27	2.76	39	3.14	15.56		41.1	0.60	154	0.21	2.28
VO 04	41.2		65	212	0.09	133	14.3	0.86		0.22	1.58	80	3.00	1.01		46.0	0.16	127	0.13	1.34
VO 10	86.1		72	10	0.13	88	15.8	1.23		0.30	2.65	37	2.86	4.75		44.5	0.53	129	0.20	2.11
VO 35	52.3		70	33	0.11	18	17.8	1.51		0.33	2.74	9	5.25	5.32		44.7	0.78	177	0.20	2.67
VO 55	88.5		60	7	0.46	38	15.1	1.46		0.27	2.64	23	3.13	9.66		37.9	0.28	148	0.23	2.49
VO 24	74.0		36	371	0.13	86	14.6	0.78		0.15	1.39	96	2.14	3.23		22.3	0.37	120	0.13	1.30
VO 51	7.1		75	113	0.03	498	13.8	1.95		0.47	4.43	73	6.17	1.33		41.0	0.39	60	0.30	3.29
VO 52	29.6		60	279	0.06	74	10.3	1.67		0.18	3.37	133	2.35	0.97		60.2	0.73	58	0.23	2.86
RF#25	512.9	0.37	58	153	0.89	46	19.0	2.20	6.5	0.85	3.77	59	7.68	17.13	2.16	40.4	1.08	380	0.31	0.48
TW 02	53.1		60	206	0.99	143	16.6	0.84		0.09	2.70	114	1.89	8.86		42.6	0.65	166	0.16	0.38
RF#34	461.3	0.56	56	241	1.46	53	16.4	1.64	9.8	0.36	2.59	87	6.97	20.58	2.03	32.2	0.93	303	0.22	0.33
RF#87	193.8	0.45	45	239	0.43	2	15.9	1.87	37.6	0.06	2.98	108	6.55	4.31	0.56	36.9	0.59	183	0.23	0.38
AW024	46.1	0.24	63	762	0.03	7	12.7	1.46	15.5	0.20	2.32	186	2.86	0.20	0.36	16.1	1.23	125	0.17	0.48
UB3	29.3	0.46	63	286	0.30	74	16.2	1.97	7.7	0.24	3.45	67	1.24	2.96		40.0	0.72	98	0.26	0.89
UB1	20.5	0.24	62	753	0.17	112	11.3	0.96	16.7	0.16	1.33	230	1.01	1.56		33.4	0.12	89	0.11	0.45
PH110	24.2	0.32	57	56	0.49	121	15.1	2.47	13.2	0.54	3.64	35	1.66	5.77	0.79	39.3	0.79	129	0.29	1.05
R 110	53.1		54	714	1.19	25	17.3	1.23	32.8	0.05	2.19	123	1.50	8.80		32.4		123	0.20	0.59
R 111	72.5		57	577	2.57	74	14.6	1.14	22.3		1.90	99	1.65	17.27		35.3		117	0.16	0.51
PH108	63.4	0.11	43	467	1.03	31	11.6	0.93	15.7	0.14	1.48	57	0.98	6.49	0.36	26.1	0.13	99	0.13	0.38
PH104	16.1	0.13	66	1125	0.05	16	9.2	0.56	4.3	0.36	0.80	282	0.59	0.27	0.44	25.9	0.30	57	0.08	0.34
PH118	44.1		83	189	0.16	75		2.78			4.95	104	2.65	3.07		37.3		128	0.36	1.10
PH119	43.5	0.20	94	1525	0.08	26	12.0	1.08	13.8	0.29	1.64	514	0.93	2.15	0.44	40.6	0.07	27	0.21	0.54
PH120	103.6	0.16	68	374	0.99	2	14.1	1.42	45.0	1.14	2.15	124	0.77	14.72	0.50	63.7	0.08	63	0.23	0.66

Table 4 (*Continued*)

SampleID	Ba ICPMS ppm	Be ICPMS ppm	Co ICPMS ppm	Cr ICPMS ppm	Cs ICPMS ppm	Cu ICPMS ppm	Ga ICPMS ppm	Hf ICPMS ppm	Li ICPMS ppm	Mo ICPMS ppm	Nb ICPMS ppm	Ni ICPMS ppm	Pb ICPMS ppm	Rb ICPMS ppm	Sb ICPMS ppm	Sc ICPMS ppm	Sn ICPMS ppm	Sr ICPMS ppm	Ta ICPMS ppm	Th ICPMS ppm
SO 04	41.4		52	204	0.35	48	15.2	0.95		0.08	1.52	90	0.78	2.94		34.8	0.34	111	0.10	0.47
MN006	15.8	0.04	55	660	0.28	25	12.5	1.20	27.7	1.59	1.91	142	6.73	1.22	1.02	40.0	0.79	119	0.15	0.29
UB4	19.4	0.43	65	164	0.28	116	16.2	1.55	6.6	0.19	2.54	115	2.07	1.79		41.1	0.70	102	0.17	0.27
AW059	41.5	0.25	84	177	0.27	87	15.5	0.90	5.4	0.23	1.44	48	2.95	0.68	0.46	28.8	1.16	107	0.16	0.21
MN360	29.9	0.12	85	1525	2.52	46	9.7	0.76	40.1	0.09	1.08	506	0.71	6.05	1.66	23.9	1.58	32	0.09	0.07
MN239	24.2	0.16	82	818	0.49	129	10.9	0.92	36.4	0.04	1.36	315	2.88	1.60	2.13	30.9	4.06	173	0.10	0.10
PH107	28.2	0.14	83	1085	0.23	31	10.7	0.79	8.4	0.23	0.93	243	1.66	0.73	0.44	34.3	1.03	95	0.12	0.28
PH106	64.0		62	644	0.89	41		0.86			0.97	165	2.49	1.94		40.0		92	0.07	0.22
MN128	5.7	0.08	84	1979	4.20	2	9.3	0.72	47.3	0.13	1.02	619	0.86	2.35	0.25	32.8	0.39	14	0.09	0.09
MN178	1.8		92	2225	0.42	71	4.9	0.37	12.6	0.07	0.49	1517	1.04	0.20	0.87	19.6	0.07	62	0.05	0.04
MN163	2.4	0.21	94	2983	0.73	7	7.0	0.59	11.0	0.14	0.76	997	0.94	0.32	0.29	28.0	0.70	34	0.07	0.15
AW020	4.1	0.10	108	4291	2.73	89	8.4	0.66	8.1	0.05	0.76	874	0.27	0.55	0.63	35.1	3.46	17	0.06	0.16
SO 07	3.8		36	1077	5.01	2	2.2	0.15		0.01	0.25	357	0.79	1.21		13.9	0.45	126	0.03	0.05
PHAG039	28.3	0.07	74	1554	1.56	26	9.0	0.79	35.4	0.05	1.33	370	0.55	15.84	0.15	31.7	2.02	22	0.11	0.21
PHAG040	5.6		81	1411	0.30	54		0.89			1.38	481	0.90	0.93		38.4		54	0.09	0.29
PHAG041	13.7	0.04	77	1406	0.64	48	8.1	0.70	21.3	0.03	1.32	321	0.80	5.04	0.16	30.3	0.40	14	0.12	0.23
PHAG043	43.8	0.03	58	566	0.79	174	10.4	0.50	11.7	0.23	0.89	95	1.61	11.00	1.67	42.5	0.47	141	0.10	0.17
PHAG044	53.1	0.17	73	1696	1.22		9.4	0.74	29.2	0.09	1.10	401	1.88	7.40	0.07	19.6	0.62	59	0.10	0.20
PH125	70.1	0.98	49	1	25.14	6	23.3	5.10	21.2	0.79	5.97	1	1.05	8.78	0.34	31.3	0.14	84	0.41	1.76
PH128	28.5	0.16	50	447	0.29	180	15.4	0.67	3.6	0.19	1.34	102	1.24	1.96	0.39	43.2	1.36	140	0.19	0.21
PH129	6.3	0.11	110	352	0.60	8	9.6	0.42	27.6	0.08	0.83	604	0.26	1.63	0.19	15.9	0.07	7	0.11	0.10
PH135	51.1	0.23	52	112	1.76	131	11.3	0.85	34.5	0.20	1.96	95	2.07	16.21	0.15	40.2	2.29	207	0.14	0.45
PH136	29.3	0.52	78	1	0.61	21	17.8	2.34	20.2	0.27	4.40	22	1.06	3.62	0.10	46.3	1.40	84	0.46	0.85
PH137	24.6	0.16	135	130	0.96	141	11.7	0.54	6.0	0.82	0.99	102	3.47	5.87	0.47	46.8	1.11	148	0.37	0.18
PH140	34.4	0.53	96	170	0.08	3	17.2	2.53	12.6	0.35	3.69	54	1.99	2.00	0.08	34.6	1.95	96	0.24	0.86
PH141	46.0	0.37	66	350	0.36	126	16.7	1.96	7.5	0.42	3.99	75	1.74	1.98	0.17	46.4	1.29	114	0.42	0.74
PHAG045	44.5	0.48	60	185	0.19	46	16.1	2.40	10.8	0.46	4.28	73	4.25	1.97	0.14	36.4	1.03	134	0.32	0.86
LB3	39.3	0.76	62	90	0.30	83	19.7	2.76	32.2	0.30	4.46	65	4.22	3.76		41.3	1.32	116	0.30	0.94
LB5	52.0	0.64	58	89	0.56	64	19.9	2.85	13.4	0.32	4.92	65	1.12	4.03		40.8	0.78	141	0.35	0.99
LB6	89.5	0.70	66	86	0.62	14	17.7	2.63	18.7	0.30	4.37	67	1.66	6.82		38.8	0.47	124	0.27	0.95
LGU1	53.7	0.73	60	92	4.24	177	19.3	2.69	73.7	0.41	4.92	64	3.04	12.64		40.7	1.63	107	0.35	0.95
LB7 A	236.2	0.72	61	76	1.79	199	20.3	2.44	35.2	0.59	4.28	76	8.68	49.68		35.3	1.94	163	0.29	0.84
LB1	96.0	0.70	59	91	6.56	96	20.2	2.74	60.6	0.16	4.30	59	75.34	39.64		41.9	0.61	96	0.24	0.96
R 165	26.0	0.76	84	0	0.68	130	24.9	4.43	66.3	1.23	6.87	12	2.47	4.79		44.0		88	0.50	1.67
R 164	50.6	0.72	70	1	2.73	91	21.9	3.70	47.5	0.36	3.39	17	2.76	6.83		43.2		154	0.22	1.39
LB4	36.0	1.02	87	97	0.19	63	19.8	2.75	37.0	3.21	4.93	71	5.96	3.45		42.9	1.67	159	0.28	0.92
PH121	62.5		84	89	0.31	75		2.89			4.33	81	1.29	4.60		41.7		114	0.32	0.89
PH123	80.3	0.47	68	86	2.08	24	14.8	2.50	21.9	0.39	4.98	79	1.33	18.00	0.56	44.9	0.15	90	0.49	0.92
PH131	81.7	0.76	61	81	1.67	28	19.0	4.24	38.8	1.12	8.37	41	1.25	11.99	0.32	34.8	0.11	138	0.75	1.76
PH132	77.9	0.65	64	131	1.00	60	19.8	3.76	31.7	1.00	8.47	48	1.24	10.32	0.48	35.3	1.58	152	0.78	1.59
PHAG048	69.8	0.27	94	2062	4.90	38	8.5	1.02	31.3	0.37	1.86	479	1.39	13.02	0.26	28.5	0.33	53	0.18	0.86
PH142	7.2	0.27	93	2369	0.23	1	8.3	1.04	11.5	0.20	2.61	619	0.61	1.25	0.36	33.7	1.51	25	0.28	0.93
PH143	73.7	0.34	86	2260	5.90	7	9.5	1.75	32.6	0.47	4.02	656	1.04	20.79	0.17	30.3	1.91	52	0.43	1.95
PH144	134.8	0.65	63	108	0.30	102	13.6	1.66	11.5	0.31	2.46	65	2.67	6.91	0.12	29.8	1.45	125	0.20	2.04
PH145	35.6		52	543	0.17	25		1.98			3.58	150	1.34	0.91		39.7		117	0.26	2.02
PH146	1.2	0.18	115	3397	0.55	6	6.8	1.11	2.8	0.24	2.56	1014	0.50	0.28	0.13	23.4	1.19	13	0.31	1.18
PHAG050	50.2	0.31	65	170	0.17	99	15.1	1.92	26.0	0.33	3.16	69	1.05	5.26	0.07	38.8	0.95	105	0.25	0.35
PHAG053	40.7	0.31	65	529	0.09		12.2	0.77	13.8	0.70	1.60	134	3.38	3.93	0.51	35.1	0.22	85	0.14	0.23
PHAG031	57.4	0.25	65	557	0.33	79	11.1	1.12	3.1		1.70	165	0.61	2.50	0.14	39.7	0.41	94	0.12	0.24
PHAG056	91.5	0.23	66	548	3.02	73	13.2	1.16	6.9		1.71	163	0.55	18.19	0.10	37.1	0.46	154	0.13	0.24
PH148	48.8		76	175	0.10	90		2.19			3.32	109	1.68	2.74		46.2		97	0.24	0.39
PHAG062	1.5		93	2454	1.84	102		0.42			0.49	1448	0.35	0.53		26.0		35	0.03	0.03
PHAG063	1.2	0.08	97	2677	0.71	43	6.0	0.41	8.8		0.46	1211	0.29	0.51	0.10	22.5	0.18	43	0.04	0.03
PHAG064	3.7	0.08	87	2624	2.04	45	6.0	0.44	7.5		0.51	1204	0.46	1.90	0.14	23.9	0.18	40	0.03	0.06
PH#3	3.2		97	2503	0.33	94		0.40			1.39	1266	0.32	0.96		25.7		25	0.04	0.09
PH#4	284.6	0.34	62	353	0.16	76	13.1	1.29	38.3	0.24	2.89	75	1.58	4.41	0.14	44.6	0.46	92	0.24	0.57

Table 4 (*Continued*)

SampleID	U ICPMS ppm	V ICPMS ppm	Y ICPMS ppm	Zn ICPMS ppm	Zr ICPMS ppm	La ICPMS ppm	Ce ICPMS ppm	Pr ICPMS ppm	Nd ICPMS ppm	Sm ICPMS ppm	Eu ICPMS ppm	Gd ICPMS ppm	Tb ICPMS ppm	Dy ICPMS ppm	Ho ICPMS ppm	Er ICPMS ppm	Tm ICPMS ppm	Yb ICPMS ppm	Lu ICPMS ppm
VO 02	0.62	214	15.7	66	53.6	8.35	16.53	2.04	8.28	2.02	0.72	2.32	0.40	2.54	0.55	1.63	0.24	1.53	0.23
VO 04	0.36	208	11.8	75	33.2	4.85	9.96	1.26	5.27	1.36	0.53	1.61	0.29	1.88	0.41	1.22	0.18	1.16	0.18
VO 10	0.53	223	14.6	67	52.5	7.71	15.18	1.83	7.35	1.79	0.63	2.04	0.35	2.24	0.49	1.44	0.21	1.36	0.20
VO 35	0.68	565	16.7	90	60.4	9.25	18.58	2.27	9.19	2.20	0.70	2.47	0.42	2.67	0.58	1.69	0.25	1.59	0.24
VO 55	0.64	209	15.4	61	55.3	8.99	17.77	2.14	8.66	2.04	0.67	2.31	0.39	2.47	0.54	1.57	0.23	1.46	0.22
VO 24	0.33	105	7.9	36	27.7	4.39	8.66	1.06	4.30	1.03	0.41	1.19	0.21	1.30	0.28	0.84	0.12	0.79	0.12
VO 51	0.84	257	20.9	49	80.4	11.09	21.70	2.63	10.65	2.56	0.75	2.98	0.51	3.27	0.71	2.06	0.30	1.92	0.29
VO 52	0.70	256	19.5	55	69.3	9.71	19.47	2.35	9.57	2.35	0.64	2.70	0.46	2.97	0.65	1.90	0.28	1.76	0.26
RF#25	0.12	322	28.8	59	76.1	3.90	11.05	1.79	9.23	3.19	1.06	3.87	0.75	5.01	1.18	3.32	0.47	3.13	0.48
TW 02	0.10	293	21.9	82	32.9	3.93	9.78	1.44	6.99	2.18	0.65	2.78	0.50	3.24	0.72	2.11	0.30	1.94	0.28
RF#34	0.08	240	21.1	75	57.1	6.63	12.64	1.61	7.19	2.17	0.64	2.63	0.51	3.39	0.80	2.26	0.32	2.16	0.33
RF#87	0.15	293	23.1	90	65.4	5.43	12.81	1.89	9.24	3.06	0.95	3.59	0.65	4.05	0.91	2.41	0.32	1.95	0.28
AW024	0.17	217	14.8	66	51.7	3.29	7.70	1.12	5.29	1.68	0.53	2.05	0.40	2.66	0.64	1.77	0.25	1.61	0.24
UB3	0.24	239	23.1	56	77.2	5.59	13.08	1.84	8.41	2.47	0.77	3.05	0.56	3.56	0.79	2.32	0.34	2.19	0.33
UB1	0.12	185	12.7	42	37.4	2.41	5.55	0.78	3.59	1.11	0.45	1.49	0.28	1.88	0.43	1.29	0.19	1.24	0.19
PH110	0.30	276	28.5	89	89.9	7.27	16.20	2.24	10.22	3.10	0.91	3.59	0.71	4.67	1.10	3.10	0.43	2.88	0.45
R 110	0.15	154	16.8	69	43.1	3.74	8.85	1.18	5.84	1.72	0.54	2.08	0.41	2.78	0.60	1.79	0.28	1.82	0.28
R 111	0.13	188	15.2	63	38.9	3.19	7.67	1.03	5.14	1.54	0.54	1.86	0.38	2.55	0.55	1.65	0.25	1.67	0.26
PH108	0.10	155	12.2	39	33.5	2.58	5.84	0.82	3.86	1.23	0.41	1.46	0.29	1.97	0.47	1.31	0.19	1.23	0.19
PH104	0.09	159	9.1	44	17.6	1.95	4.09	0.57	2.62	0.85	0.36	1.06	0.22	1.49	0.36	1.01	0.14	0.94	0.14
PH118	0.30	300	28.8	108	102.7	8.05	19.21	2.65	12.92	3.54	1.15	4.34	0.76	4.91	1.06	3.19	0.44	3.14	0.44
PH119	0.12	227	12.6	75	39.2	2.87	6.22	0.86	3.92	1.23	0.48	1.53	0.30	2.03	0.47	1.36	0.19	1.28	0.19
PH120	0.16	306	19.0	88	51.3	3.83	8.29	1.15	5.29	1.72	0.51	2.20	0.44	2.98	0.70	2.01	0.28	1.86	0.28
SO 04	0.12	202	14.2	57	39.6	2.82	6.57	0.90	4.15	1.26	0.49	1.70	0.32	2.12	0.48	1.40	0.21	1.33	0.20
MN006	0.09	233	16.7	109	43.9	1.51	4.50	0.77	4.15	1.56	0.44	2.09	0.40	2.59	0.59	1.74	0.25	1.64	0.25
UB4	0.07	281	23.3	66	59.0	3.12	8.38	1.35	6.90	2.28	0.87	2.97	0.55	3.56	0.80	2.33	0.34	2.20	0.34
AW059	0.05	146	16.9	50	28.4	2.35	6.20	1.01	5.19	1.84	0.67	2.24	0.44	2.96	0.70	1.95	0.27	1.81	0.28
MN360	0.02	197	10.9	128	27.4	0.97	2.85	0.51	2.77	1.04	0.48	1.40	0.27	1.78	0.40	1.16	0.17	1.07	0.16
MN239	0.03	226	14.4	67	34.9	1.86	4.66	0.78	4.10	1.42	0.52	1.81	0.34	2.24	0.50	1.46	0.21	1.38	0.21
PH107	0.05	205	12.1	57	25.6	1.36	3.31	0.51	2.55	0.95	0.40	1.31	0.28	1.93	0.47	1.35	0.19	1.29	0.20
PH106	0.06	215	13.0	64	31.2	1.72	4.20	0.58	3.15	0.99	0.40	1.57	0.31	2.18	0.49	1.43	0.20	1.42	0.22
MN128	0.03	185	10.9	63	25.1	1.01	3.05	0.55	3.03	1.08	0.38	1.39	0.26	1.72	0.38	1.12	0.16	1.05	0.16
MN178	0.01	105	5.3	72	13.4	0.49	1.38	0.25	1.35	0.50	0.17	0.66	0.13	0.82	0.18	0.54	0.08	0.50	0.08
MN163	0.04	156	9.4	68	21.3	0.80	2.49	0.45	2.41	0.89	0.54	1.18	0.23	1.49	0.34	0.97	0.14	0.93	0.14
AW020	0.04	207	8.7	70	20.7	0.81	2.22	0.40	2.28	0.91	0.17	1.20	0.24	1.59	0.37	0.98	0.13	0.85	0.13
SO 07	0.09	77	3.3	38	4.9	0.32	0.82	0.14	0.79	0.30	0.07	0.40	0.08	0.52	0.11	0.34	0.05	0.33	0.05
PHAG039	0.09	192	10.0	81	26.4	1.23	3.88	0.67	3.42	1.18	0.43	1.36	0.27	1.74	0.40	1.09	0.15	0.97	0.15
PHAG040	0.08	224	12.7	91	32.3	2.32	6.04	0.90	4.54	1.38	0.43	1.89	0.31	2.16	0.48	1.44	0.18	1.42	0.18
PHAG041	0.06	197	9.5	51	22.0	1.60	4.33	0.69	3.54	1.18	0.40	1.35	0.26	1.70	0.39	1.03	0.14	0.89	0.13
PHAG043	0.05	205	9.2	54	15.1	1.47	3.61	0.56	2.86	1.00	0.39	1.21	0.24	1.57	0.36	1.00	0.14	0.89	0.13
PHAG044	0.06	198	10.2	81	24.3	2.31	4.74	0.72	3.57	1.21	0.35	1.41	0.28	1.81	0.42	1.15	0.16	1.04	0.16
PH125	0.49	0	76.6	83	181.9	12.75	31.24	4.92	24.47	8.05	2.55	9.70	1.85	12.09	2.77	7.89	1.11	7.29	1.10
PH128	0.06	217	12.2	47	20.9	1.77	4.38	0.69	3.59	1.27	0.58	1.56	0.31	2.01	0.46	1.30	0.18	1.19	0.18
PH129	0.03	89	6.6	100	14.7	0.96	2.63	0.42	2.13	0.71	0.33	0.84	0.16	1.04	0.24	0.70	0.10	0.66	0.10
PH135	0.12	195	16.6	87	27.6	2.41	6.44	1.06	5.37	1.86	0.59	2.18	0.42	2.78	0.64	1.80	0.25	1.66	0.26
PH136	0.20	406	30.0	104	81.8	5.37	14.19	2.22	10.83	3.50	1.16	4.03	0.77	4.98	1.13	3.16	0.44	2.92	0.44
PH137	0.03	220	8.9	45	17.1	1.20	3.16	0.52	2.70	0.99	0.46	1.18	0.23	1.50	0.34	0.94	0.13	0.85	0.13
PH140	0.29	245	34.4	83	83.2	5.86	15.29	2.43	12.11	3.99	1.13	4.69	0.92	6.05	1.40	3.99	0.56	3.72	0.57
PH141	0.18	282	25.5	103	71.0	4.78	11.82	1.79	8.79	2.83	0.92	3.31	0.64	4.13	0.95	2.68	0.38	2.48	0.38
PHAG045	0.23	301	30.5	136	85.0	6.55	14.85	2.19	10.56	3.47	1.18	3.95	0.77	5.06	1.19	3.32	0.46	3.07	0.47
LB3	0.26	374	36.0	111	107.6	6.78	16.43	2.43	11.55	3.56	1.12	4.45	0.82	5.42	1.23	3.64	0.53	3.43	0.52
LB5	0.25	324	34.7	85	111.5	6.64	16.53	2.47	11.75	3.61	1.05	4.55	0.83	5.32	1.19	3.48	0.51	3.29	0.51
LB6	0.26	314	34.9	83	104.0	7.17	17.68	2.60	12.27	3.67	1.15	4.55	0.82	5.27	1.17	3.46	0.50	3.28	0.51
LGU1	0.26	267	30.8	49	109.0	6.77	15.93	2.27	10.70	3.19	1.07	4.00	0.72	4.64	1.04	3.05	0.44	2.90	0.45

Table 4 (*Continued*)

SampleID	U ICPMS ppm	V ICPMS ppm	Y ICPMS ppm	Zn ICPMS ppm	Zr ICPMS ppm	La ICPMS ppm	Ce ICPMS ppm	Pr ICPMS ppm	Nd ICPMS ppm	Sm ICPMS ppm	Eu ICPMS ppm	Gd ICPMS ppm	Tb ICPMS ppm	Dy ICPMS ppm	Ho ICPMS ppm	Er ICPMS ppm	Tm ICPMS ppm	Yb ICPMS ppm	Lu ICPMS ppm
LB7 A	0.23	293	30.9	154	97.3	6.13	15.01	2.23	10.60	3.25	1.15	4.04	0.73	4.65	1.04	3.05	0.45	2.92	0.45
LB1	0.27	307	36.4	56	111.4	6.96	16.65	2.47	11.84	3.59	1.27	4.51	0.82	5.31	1.19	3.53	0.52	3.41	0.52
R 165	0.51	340	52.1	120	171.3	10.73	26.20	3.87	18.66	5.74	1.57	7.03	1.26	8.16	1.81	5.37	0.79	5.21	0.79
R 164	0.40	305	46.0	149	141.5	9.53	22.90	3.45	16.75	5.14	1.56	6.28	1.14	7.28	1.62	4.76	0.70	4.51	0.68
LB4	0.34	339	37.8	67	116.3	7.00	17.43	2.62	12.53	3.84	1.32	4.72	0.86	5.52	1.22	3.58	0.52	3.39	0.53
PH121	0.25	315	30.2	95	100.7	6.48	16.15	2.31	11.28	3.45	1.15	4.77	0.79	5.29	1.12	3.41	0.46	3.25	0.47
PH123	0.23	321	32.1	108	91.8	6.51	15.28	2.27	11.00	3.50	1.16	4.15	0.79	5.16	1.18	3.34	0.47	3.07	0.46
PH131	0.43	195	48.1	103	168.9	13.71	31.02	4.44	20.69	6.00	1.90	6.82	1.23	7.80	1.77	4.97	0.69	4.58	0.70
PH132	0.37	222	43.7	121	150.4	11.83	27.25	3.93	18.58	5.46	1.90	6.12	1.11	7.04	1.59	4.46	0.62	4.12	0.63
PHAG048	0.24	171	11.9	61	35.3	4.11	8.53	1.13	4.98	1.46	0.48	1.59	0.30	1.99	0.46	1.30	0.18	1.20	0.19
PH142	0.24	188	14.2	71	34.6	3.24	7.65	1.09	5.05	1.57	0.49	1.83	0.35	2.32	0.53	1.52	0.22	1.42	0.22
PH143	0.48	172	18.9	71	60.6	6.70	14.86	1.98	8.61	2.39	0.60	2.59	0.48	3.07	0.70	2.00	0.29	1.90	0.29
PH144	0.61	161	22.9	80	54.9	9.39	19.67	2.60	11.15	3.01	0.83	3.29	0.61	3.94	0.90	2.55	0.36	2.37	0.35
PH145	0.34	207	19.7	87	70.8	7.59	16.49	2.24	9.56	2.71	0.69	3.01	0.52	3.54	0.77	2.17	0.33	2.20	0.31
PH146	0.27	132	11.3	81	38.1	5.03	9.66	1.23	5.23	1.41	0.27	1.56	0.29	1.87	0.43	1.22	0.18	1.16	0.18
PHAG050	0.10	301	27.0	73	67.6	3.97	10.14	1.61	8.09	2.79	0.93	3.34	0.66	4.46	1.05	2.93	0.41	2.73	0.42
PHAG053	0.07	234	15.0	58	23.5	2.36	5.69	0.88	4.39	1.52	0.48	1.80	0.36	2.44	0.58	1.65	0.23	1.54	0.23
PHAG031	0.07	219	14.7	74	40.1	2.79	7.12	1.09	5.39	1.69	0.69	2.26	0.40	2.62	0.58	1.69	0.26	1.65	0.25
PHAG056	0.06	207	14.0	67	41.8	2.49	6.60	1.02	5.05	1.60	0.67	2.15	0.38	2.54	0.56	1.62	0.25	1.59	0.24
PH148	0.10	316	26.8	112	78.1	4.50	11.44	1.79	9.39	2.76	0.96	3.93	0.68	4.60	1.00	3.04	0.44	3.04	0.43
PHAG062	0.01	129	5.9	75	14.9	0.67	1.84	0.26	1.33	0.43	0.11	0.71	0.13	0.91	0.20	0.69	0.10	0.64	0.10
PHAG063	0.01	114	6.7	55	13.9	0.59	1.85	0.32	1.80	0.64	0.26	0.94	0.17	1.15	0.26	0.76	0.12	0.76	0.12
PHAG064	0.02	129	7.7	49	14.7	0.53	1.66	0.31	1.75	0.69	0.29	1.01	0.20	1.35	0.31	0.92	0.15	0.98	0.15
PH#3	0.05	125	7.8	89	15.4	1.11	3.45	0.55	2.66	0.73	0.42	1.04	0.24	1.31	0.28	0.83	0.10	0.80	0.12
PH#4	0.34	257	19.5	64	43.3	3.11	9.65	1.30	6.43	2.07	0.71	2.48	0.48	3.15	0.64	2.08	0.29	1.97	0.30

[A] Drillhole collar coordinates are listed in Supplementary Appendix B. Number listed for Butchers Basalt samples represent Easting Coordinate (MGA).

[B] Number listed for Butchers Basalt samples represent Northing Coordinate (MGA)

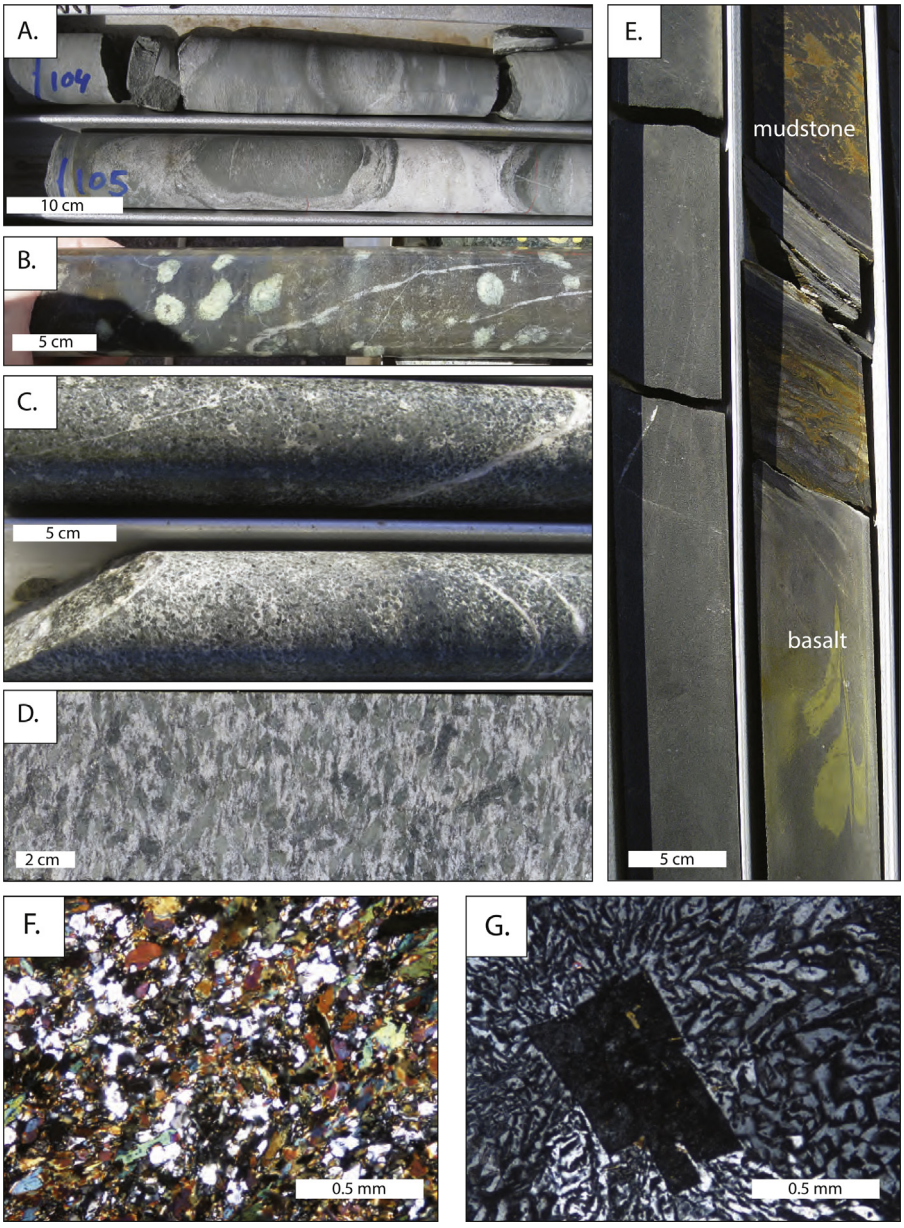

Fig. 4. Representative photos of drillcore and microphotographs of mafic lithofacies and interflow sediments. (A) Pillow basalt lithofacies (Hickies Bore Basalt; EMSD-931 47 m), (B) Massive basalt with feldspar megacrysts (White Hope Basalt; EMSD-919 300 m), (C) Dolerite lithofacies (Bounty Igneous Complex; EMSD1032 210 m), (D) Gabbro lithofacies (Never Can Tell Basalt comagmatic intrusion; SEIS-05 1144.2), (E) Mudstone lithofacies (interflow sediment with basalt at contact between Songvang and Hickies Bore Basalts; EMSD1034 242), (F) Photomicrograph of quartz-hornblende altered groundmass, common to basalts (Never Can Tell Basalt; EMSD222 321.5) and (G) Photomicrograph of feldspar crystal surrounded by granophyric groundmass (Turret Dolerite; VVDD187 359.1 m).

similar composition to their hosts, which are interpreted as comagmatic. The stratigraphic units, from oldest to youngest, include:

4.2.1. Butchers Well Basalt

The Butchers Well Basalt is the lowermost greenstone unit and is intruded by granite at its base. It was only observed in subcrop and a few outcrops, and was not intersected by drilling. It consists of light green, massive basalt. There were no features suggestive of pillows, although recognition of such features in outcrop is challenging in this district. The mineralogy consists of hornblende, quartz, plagioclase, muscovite and chlorite.

The Butchers Well Basalt has amongst the lowest Mg# (21–35) of the Agnew section, and is a high-Fe tholeiite to tholeiitic dacite. It is 2–4× more enriched than primitive mantle, slightly depleted in LREEs ($[La/Sm]_{PM}$ = 0.7–1.0) and with a flat heavy REE (HREE) pattern ($[Gd/Yb]_{PM}$ = 1.0)).

In summary, although there is limited data, the Butchers Well Basalt is a subaqueous extrusive tholeiitic basalt that is highly fractionated (low-Mg#) and moderately enriched.

4.2.2. Donegal Komatiite

The Donegal Komatiite is light grey to green, undeformed to highly deformed, and altered. It consists of several komatiitic flows, with individual sheets 0.8–1.2 m thick, and lesser fragmental komatiite. Flow unit tops are marked by aphyric or spinifex textures. The fragmental facies (5–10 m in thickness) is interpreted as bedding parallel cataclasites and are only found at the top contact with the Hickies Bore Basalt. The mineralogy consists of talc, serpentine, carbonate and opaque minerals.

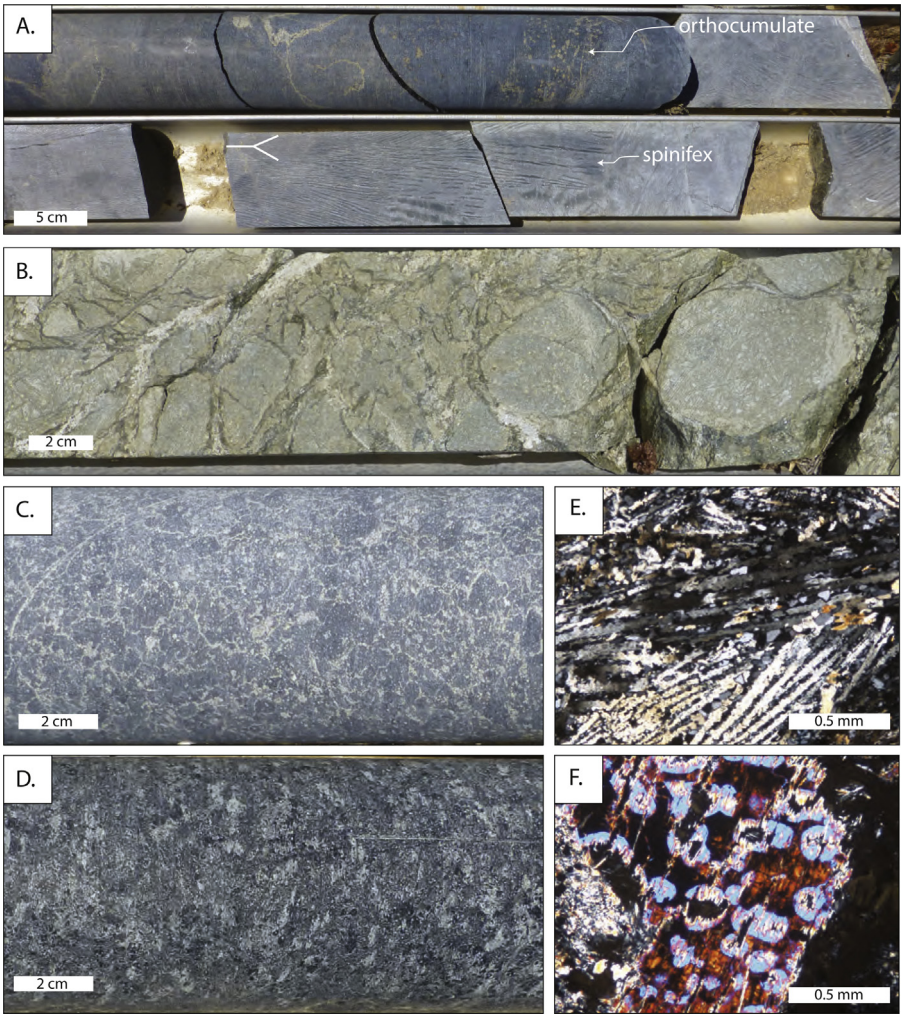

Fig. 5. Representative photos of drillcore and microphotographs of ultramafic lithofacies. (A) Spinifex-orthocumulate lithofacies association, with well-developed spinifex size grading indicating way-up (marked by younging symbol) (Agnew Komatiite; SEIS-05 479 m), (B) Fragmental ultramafic lithofacies interpreted as cataclasite (see text) (Donegal Komatiite; EMSD931 232 m); (C) Cumulate ultramafic lithofacies, olivine adcumulate texture in komatiite (Agnew Komatiite; EMSD951 387 m); (D) Cumulate ultramafic, pyroxene crystals (Bounty Igneous Complex; SEIS-06 182 m), (E) Microspinifex texture common in komatiitic basalts (Songvang Basalt; SEIS-06 667 m), and (F) Cumulate texture, characterised by olivine crystals contained in pyroxene, in a layered mafic intrusion (Bounty Igneous Complex; SEIS-06 230 m).

Samples of the aphyric and spinifex komatiite ($n = 3$) are geochemically indistinguishable from the Agnew Komatiite, which forms the basal unit of cycle II. They have high Mg# (~84) and contain low aluminium values (~7 wt.% Al_2O_3) with depleted $[La/Sm]_{PM}$ (0.5–1.0) and $[Gd/Yb]_{PM}$ (0.9–1.1).

In summary, the Donegal Komatiite consists of extrusive subaqueous komatiite flows, although alteration and deformation was focussed along the upper contact to produce cataclasites. Compositionally, the Donegal Komatiite is an uncontaminated Al-undepleted (Munro-type) komatiite (Arndt et al., 2008).

4.2.3. Hickies Bore Basalt

This stratigraphic unit is divided geochemically into upper and lower sections, separated by a thin sulphidic mudstone. The lower section consists mainly of light green massive and pillowed basalt with abundant amygdales. Several mafic sills (one 40–50 m thick, and at least three others that are 3–5 m thick) are recognised in the lower section. Most are undifferentiated sills, although the thickest sill is differentiated and includes an ultrabasic cumulate base. The upper section is composed of light green, aphyric to medium-grained, massive basalt. Basalt consists of a mosaic of mainly fine-grained (<200 μm) euhedral hornblende (75%) and quartz (25%) and rare plagioclase.

The Hickies Bore Basalt is a low-Th basalt that falls within the high-Mg- and high-Fe tholeiite fields of the Jensen diagram (Fig. 6a). It has relatively restricted and moderate Mg# (43–68, averaging 55), low contents of incompatible elements, and a relatively flat REE-profile ($[La/Sm]_{PM} = \sim 1.1$ and $[Gd/Yb]_{PM} = \sim 1.1$). Up sequence trends include an overall decrease in Mg# and concomitant increase in $[La/Sm]_{PM}$ and $[Gd/Yb]_N$. The upper Hickies Bore Basalt, relative to the lower Hickes Bore Basalt, is more enriched in incompatible elements (~2×) and has higher Zr/Y (>1.9), TiO_2 (>1.2 wt.%) and lower Mg# (<50), whereas comagmatic intrusions in the lower Hickies Bore Basalt are similar to the hosting basalts.

In summary, the Hickies Bore Basalt consists mainly of subaqueous extrusions and comagmatic intrusions of high-Mg tholeiitic composition that are slightly enriched in REEs. The sequence becomes progressively more fractionated with time.

4.2.4. Songvang Basalt

The Songvang Basalt is divided into two sections based on grain size: a lower layered section and an upper massive section. The lower section, from base to top, grades from basalt to dolerite, gabbro, ultrabasic cumulate, gabbro, dolerite and basalt, and is interpreted as a layered comagmatic intrusion to the upper section. The upper section is dark green, massive and mostly aphyric

basalt, and is interpreted to be stacked lava sheet flows. The fine-grained altered groundmass of the upper section consists mainly of fibrous talc and serpentine and minor opaque minerals, and is porphyritic in places with dispersed chlorite-replaced euhedral shapes (~0.5–3 mm), suggestive of olivine. Micro-spinifex textures (only observable in thin section), consisting of branching aggregates of <2 mm-long serpentine and talc altered blades (Fig. 5e), occur locally near the base of the upper section. A thin mudstone interval occurs within the lower portion of the upper section (Fig. 2a).

The Songvang Basalt mainly plots as a komatiitic and high-Mg tholeiitic basalt (Fig. 6a), although there is considerable compositional diversity. It is also one of only two siliceous high magnesium basalts at Agnew, containing elevated silica (47–55, averaging 53 wt.% SiO_2) for such high overall Mg# (40–84, averaging 68). The Songvang Basalt also has pronounced LREE enrichment ($[La/Sm]_{PM}$ = ~1.8) and minor HREE enrichment ($[Gd/Yb]_{PM}$ = ~1.2). The upper massive basalt is geochemically indistinguishable from the lower intrusion, with the exception of ultrabasic cumulate samples, which have higher Mg# (78–84). The Songvang Basalt can be distinguished from other stratigraphic units because it has a unique range for Zr/Th (25–50). It also has a pronounced negative Nb and Ti anomaly (Fig. 8).

In summary, the Songvang Basalt consists of extrusive subaqueous lava sheet flows intruded by a comagmatic layered mafic sill at the base. Compositionally, the Songvang Basalt is a komatiitic basalt with pronounced LREE enrichment.

4.2.5. Never Can Tell Basalt

The Never Can Tell Basalt is divided, based on geochemistry and grain size, into upper and lower sections of mostly massive basalt and a middle gabbro- and dolerite-rich section. The lower section consists of massive plagioclase porphyritic (crystals up to 5 mm) basalt while the upper section consists mainly of light green aphyric to fine-grained massive basalt with minor amounts of dolerite. The groundmass mineralogy of the lower and upper sections consists of a mosaic of hornblende and quartz (<200 μm). The lower and upper sections are interpreted as lava flows. The dominantly coarser-grained middle section has a mineralogy consisting mainly of hornblende, quartz and feldspar, as minor apatite, sphene and opaque minerals. The middle section is interpreted as a comagmatic intrusion. Up to three thin mudstone intervals occur within the unit.

The Never Can Tell Basalt is classified as a high-Fe tholeiite (Fig. 6a) and falls within both low- and intermediate-Th groups (Fig. 6c). It has low Mg# (12–74, averaging 37), high Fe (11–20, averaging 15.5 wt.% Fe_2O_3), high Ti (0.5–2.8, average = 1.6 wt.% TiO_2), and moderate enrichment in LREEs ($[La/Sm]_{PM}$ = ~1–2) and HREEs ($[Gd/Yb]_{PM}$ = 1–1.4). Such high contents of Fe classify the unit as a ferrobasalt, making it unique in this respect at Agnew. It also has relatively high contents of incompatible elements including REE, Zr, Nb, U, Y and Hf (~8–20× primitive mantle). Another difference between the Never Can Tell Basalt and the rest of the Agnew section is in terms of TiO_2/V (Fig. 10b), where all samples but those from the Never Can Tell Basalt form a rough linear trend. This discordant trend is interpreted to reflect accumulated titanomagnetite. The lower and upper basalts are geochemically similar, whereas the intrusion can be distinguished based on its higher enrichment in incompatible elements (Fig. 8) and lower Mg# (<36) (Fig. 9).

In summary, the Never Can Tell Basalt consists largely of subaqueous extrusive high-Fe tholeiitic basalts that are highly fractionated and enriched in incompatible elements. The extrusive pile is intruded by a late, even more fractionated and enriched, comagmatic sill.

4.2.6. Agnew Komatiite

The Agnew Komatiite consists of a lower sequence dominated by ultrabasic cumulate, and an upper sequence of compound lavas comprising multiple differentiated flow lobes each ~1 m thick. There are few drillholes through contacts of the cumulate and thus there is not enough data to determine whether the mode of emplacement was extrusive or intrusive. The upper contact of the upper sequence is either gradational with the overlying Burrell Well Basalt, or marked by bedding-parallel tectonic cataclasites. All samples have been altered largely to talc, serpentine and carbonate, and lesser chlorite and opaque minerals, however, relict spinifex and cumulate textures are generally preserved.

Compositions are variable, with a range of Mg# (76–93, averaging 86) and high LOI (5–26 wt.%), both of which are a result of the range of lithofacies types and alteration. Cumulates have Mg# (>86), Al_2O_3 (<6 wt.%) TiO_2 (<0.27 wt. %), with flat REE profiles (1 x primitive mantle), although with considerable scatter because results are close to the limits of detection. Aphyric and spinifex-textured komatiite (upper sequence), which represent better approximations of the parent liquid composition, is characterised by low Ti (0.3–0.6 wt.% TiO_2) and Al (5.6–10.5 wt.% Al_2O_3), high Mg# (76–85), Mg (26–31 wt.% MgO) and Al_2O_3/TiO_2 (15–30), $[La/Sm]_{PM}$ (0.6–0.7), $[Gd/Yb]_{PM}$ (0.8–1.2) with flat LREE-depleted profiles ~1–1.5× primitive mantle. Compositions for the upper lavas grade into those for the overlying Burrell Well Basalt, with a cut-off chosen at the divide between komatiite and komatiitic basalt on the Jensen plot (>22 wt.% MgO) (Fig. 6a).

The Agnew Komatiite, in summary, consists of a thick cumulate lower sequence and an overlying stacked sequence of subaqueous komatiite flows. Compositional characteristics are most similar to uncontaminated Al-undepleted (Munro-type) komatiites that are typical of the Neoarchean (Arndt et al., 2008).

4.2.7. Burrell Well Basalt

The Burrell Well Basalt consists of black to dark green and aphyric to fine-grained massive basalt, which forms sheet flows that are ~6–18 m thick, and rare pillow basalt. Darker intervals (Mg-rich) are mostly altered to talc, serpentine, chlorite and carbonate with minor amounts of opaque minerals. Some intervals display microspinifex and cumulate textures. Lighter-coloured ineravals (Mg-poor) comprise hornblende, plagioclase and quartz.

The Burrell Well Basalt is a low-Th basalt with a systematic spread of compositions from komatiitic basalt at the base to high-Mg basalt at the top (Fig. 6a). These compositional variations are reflected in Mg# (52–76) as well as LREEs ($[La/Sm]_{PM}$ = 0.6–1.2) and HREEs ($[Gd/Yb]_{PM}$ = 0.8–1.2).

In summary, the Burrell Well Basalt represents subaqueous basalts that are compositionally gradational from the underlying Agnew Komatiite and become progressively more fractionated through time, starting in the komatiitic basalt field on the Jensen plot and finishing in the high-Mg tholeiite field. The Burrell Well Basalt is contemporaneous with, and has an interdigitating relationship to, the texturally identical Redeemer Basalt, which also locally overlies the Agnew Komatiite. However, the two units can be distinguished based on compositional differences. This relationship suggests that there were two localised, overlapping, compositionally distinct volcanic centres.

4.2.8. Redeemer Basalt

The Redeemer Basalt is divided into lavas and one intrusion. The lavas consist of dark-coloured massive basalt that is made up of mainly sheet flows (~4–16 m thick) and minor pillow basalts, and are intercalated with at least one thin mudstone interval (Fig. 2). The intrusion consists mainly of dolerite with lesser basalt and gabbro, and has sharp chilled margins with the lavas, and in one case, the Agnew Komatiite. Finer-grained intervals consist of talc,

serpentine, carbonate and chlorite with relict textures including microspinifex, while the doleritic and gabbroic intervals consist mainly of larger crystals of plagioclase, hornblende and rare potassium feldspar in a quartz-feldspar groundmass, including minor opaque minerals.

The Redeemer Basalt is the only basalt in the study area that falls exclusively within the intermediate-Th group, and consists of komatiitic and high-Mg basalts (Fig. 6). The Redeemer Basalt has relatively high Mg# (47–74) with enriched LREE ($[La/Sm]_{PM}$ = 0.8–1.9) and relatively undepleted HREE ($[Gd/Yb]_{PM}$ = 0.9–1.2). Based on similar geochemistry to the lavas, the intrusion is interpreted as being related (i.e., comagmatic). The intrusion is generally more fractionated (Mg# < 65) and has elevated Al_2O_3, REE and other incompatible elements. Up sequence trends within the lavas show a systematic decrease in Mg# and increase in both LREE and REE.

Barnes et al. (2014) identified an interval of low-Th tholeiitic mafic rocks lying within the Redeemer Basalt package on the eastern limb of the Lawlers Anticline (north-east of Traverse D; Fig. 1a). This interval was not sampled in this study. Data of Barnes et al. (2014) imply that a section of Redeemer Basalt stratigraphy is present here that is not preserved on the more attenuated western limb of the anticline. Examination of percussion chips in the field indicates that the low-Th unit is a mixture of basalt and dolerite that cannot be reliably assigned to an intrusive or extrusive origin. Further investigation is needed to resolve the issue, but it remains possible that the Redeemer Basalt also contains a component of low-Th group basalts not recognised in this study. Alternatively, this interval may be intercalated Burrell Well Basalt.

In summary, the intermediate-Th Redeemer Basalt consists of subaqueous extrusive basalts (komatiitic basalt) intruded by a more evolved comagmatic (high-Mg tholeiite) sill. A more complex internal stratigraphy may exist, but remains unresolved pending future sampling.

4.2.9. White Hope Basalt

The White Hope Basalt is a porphyritic (megacrystic), dark-coloured massive basalt, interpreted as sheet flows, with distinctive euhedral plagioclase megacrysts (up to ~20%), ranging in size up to ~2 cm. Intervals are massive and without signs of internal organisation or pillows. Megacrysts are set in a crystalline altered groundmass of plagioclase, clinopyroxene and opaque minerals and very fine-grained unresolvable interstitial minerals.

The White Hope Basalt has the highest average aluminium content (19 wt.% Al_2O_3) and some of the most evolved compositions, with low Mg# (40–52). It is a low-Th, calc-alkaline basalt/andesite.

In summary, the White Hope Basalt is a subaqueous extrusive, megacrystic, highly fractionated and Al- and Fe-rich basalt.

4.3. Ultramafic–mafic intrusive rocks

The stratigraphy includes two ultramafic–mafic sills, the Bounty Igneous Complex and the Turret Dolerite. These sills are described separately here, in comparison to sills described in Section 4.2, because they are not genetically related (i.e., comagmatic) to any lavas in the sequence.

4.3.1. Bounty Igneous Complex

The Bounty Igneous Complex intrudes the Never Can Tell Basalt and comprises three mafic sills that are separated by thin screens of the host rock. Each of the sills comprise basalt and ultrabasic cumulate at the base, gabbro and dolerite interiors with granophyric domains, and basalt at the top margin. Chilled margins with the Never Can Tell Basalt are observed on the top and bottom contacts, making the Bounty Igneous Complex younger than the host. Mafic intervals consist dominantly of hornblende and quartz while ultrabasic layers consist of talc-carbonate-serpentine replacing original olivine and pyroxene.

Most samples of the Bounty Igneous Complex have compositions corresponding to low-Th, high-Mg tholeiitic basalts with an average Mg# = 59. They have relatively flat REE profiles ($[La/Sm]_{PM}$ = ~1.1; $[Gd/Yb]_{PM}$ = ~1.1) that are 4–6× enriched relative to primitive mantle. They are geochemically similar to the White Hope Basalt, but lack the characteristic plagioclase megacrysts.

In summary, the Bounty Igneous Complex represents at least three tholeiitic differentiated ultramafic–mafic sills that are enriched, relative to primitive mantle. Lavas of similar composition are not found anywhere in the sequence. Because the relative timing of the intrusion in relation to cycles I and II is poorly constrained, the Bounty Igneous Complex is tentatively excluded from the cycles.

4.3.2. Turret Dolerite

The Turret Dolerite (referred to as the Vivien Dolerite in some previous publications, e.g., Barnes et al., 2014) is a differentiated mafic sill comprising, from base to top, basalt, ultrabasic cumulate, gabbro, dolerite, granophyre and basalt. It intrudes the youngest extrusive stratigraphic unit (the White Hope Basalt) and thus represents the youngest stratigraphic unit in this study. The sill consists mainly of equigranular hornblende and plagioclase, which is locally surrounded by a granophyric groundmass. Olivine-rich cumulates now consist entirely of talc and carbonate, although remnant outlines of olivine grains are evident.

The high-Th Turret Dolerite plots mostly as a high-Mg tholeiitic basalt (Fig. 6a). It is of siliceous high-Mg basalt parentage (cf. Songvang Basalt) and displays significant enrichment in the LREEs ($[La/Sm]_{PM}$ = 2.2–2.9) and moderate enrichment in HREEs ($[Gd/Yb]_{PM}$ = 1.1–1.3). It also has pronounced negative Nb and Ti, and minor Ta, anomalies (Fig. 8). It is compositionally very different to the other units at Agnew and can be distinguished using a variety of ratios, including Zr/Th (<25) and $[La/Sm]_N$ (>2.2).

In summary, the Turret Dolerite is a differentiated high-Th mafic sill with extreme LREE enrichment and represents the youngest preserved major magmatic event of the section. Although the Turrett Dolerite is not comagmatic with any extrusions, it is grouped into cycle II because its timing relative to all other magmatic events is well constrained, in contrast to the Bounty Igneous Complex.

5. Geochemistry

Many studies have used trace element compositions to identify magma sources, determine the effects of crystal fractionation, and constrain contamination for Phanerozoic (e.g., Shervais, 1982; Rollinson, 1993; Fitton et al., 2000; Pearce, 2008; Jowitt and Ernst, 2013), and to a lesser degree, Archean successions (Huppert and Sparks, 1985; Arndt and Jenner, 1986; Lesher and Arndt, 1995; Smithies et al., 2005). The Agnew geochemical data will be examined to provide insight into the formation of the ultramafic–mafic rocks, including the temporal evolution of the system.

5.1. Crustal contamination, magma source and crystal fractionation

The hallmarks of crustal contamination (e.g., negative Nb and Ti anomalies: Fig. 8; $[La/Sm]_{PM}$ > 1: Fig. 9) (Pearce, 2008; van Hunen and Moyen, 2012) are evident in the Songvang Basalt, Never Can Tell Basalt, Redeemer Basalt and Turrett Dolerite; the remaining units display little to no signs of contamination. The basal Butchers Well Basalt is uncontaminated, but without timing constraints, its relationship to the overlying sequence remains unclear. The Donegal Komatiite, forming the base of cycle I, is uncontaminated

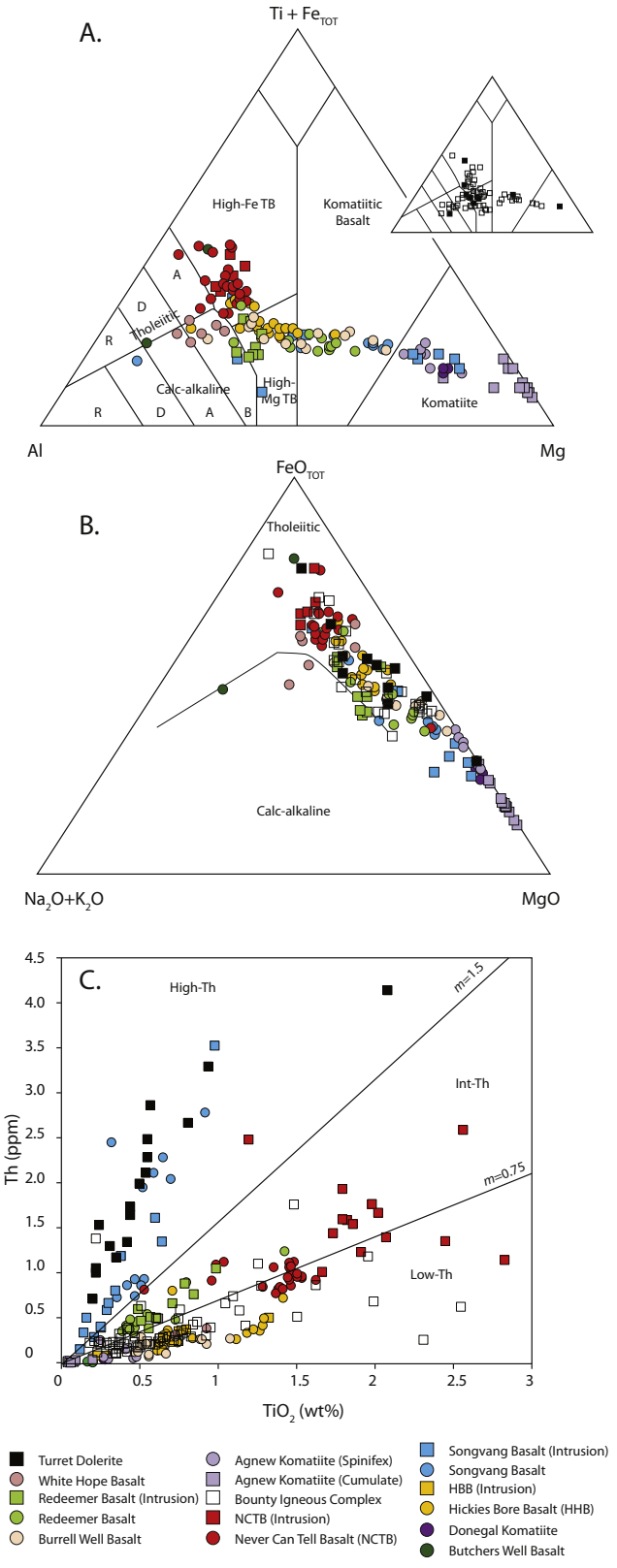

Fig. 6. Geochemical classification diagrams. (A) Mg-Ti + Fe_{TOT}-Al diagram (Jensen Plot) of Agnew suite. Bounty Igneous Complex and Turret Dolerite in inset, B) MgO-FeO_{TOT}-$Na_2O + K_2O$ diagram (AFM Plot) of Agnew suite demonstrating tholeiitic character. Black line separating fields from Irvine and Baragar (1971), and (C) Th vs. TiO_2 plot dividing suite into high-Th, low-Th and int-Th, after Barnes et al. (2012). Turret Dolerite and Songvang Basalt are the only high-Th basalts; the Redeemer Basalt is the only exclusively intermediate-Th, while the remainder are low-Th basalts, with the exception of the Never Can Tell Basalt, which straddles the boundary between intermediate- and low-Th basalts.

($[La/Sm]_{PM}$ (~0.7)) and primitive (high Mg#). The overlying Hickies Bore Basalt displays intermediate compositional characteristics (e.g., in terms of $[La/Sm]_{PM}$ and Mg#) to the overlying contaminated Songvang and Never Can Tell Basalts. This intermediate character may reflect very small amounts of contamination and record part of a general progression in the degree of contamination through time. Cycle II comprises the basal uncontaminated and primitive Agnew Komatiite, contaminated Redeemer and Turrett Dolerite, and two units that are intermediate in character, the Burrell Well and White Hope Basalts, which may also display small amount of contamination, again recording a general increase in contamination through time. The Bounty Igneous Complex, with low $[La/Sm]_{PM}$, is also uncontaminated.

We constrain the nature of the contaminant(s) by comparing trends between the Agnew geochemical data with point data for different contaminants (Figs. 9b and 10a). This is well illustrated in Fig. 10, for example, where the data spreads out between komatiites (uncontaminated magmas) and average felsic Archean crust (point 2), local andesite (3) and/or local felsic intrusion (point 1). Compositions for upper, bulk and lower continental crust are unlikely contaminants, although we cannot reject the possibility of mixing between multiple contaminants.

Magma source is constrained by the uncontaminated units; the Donegal Komatiite, Agnew Komatiite and the Bounty Igneous Complex. Both komatiites have mantle sources similar in composition to modern depleted mantle (Fig. 9b), while a more enriched source, relative to primitive mantle, is identified for the Bounty Igneous Complex. Magma source compositions may vary for other units, but our preferred explanation, based on the trends in Figs. 9b and 10a, is that units of cycles I and II all have one source (similar to modern depleted mantle) that was contaminated to varying degrees. The Bounty Igneous Complex, for reasons explained in section 4.3.1, is excluded from cycles I and II.

Geochemical trends are consistent with crystal fractionation being significant for the Agnew mafic-ultramafic rocks (Figs. 7, 9 and 10). Positive correlations between Mg# and Ni (Fig. 7) and MgO (not shown) are consistent with olivine being an important fractionating phase for the more primitive samples (Mg# > 65), the komatiites and komatiitic basalts. For more evolved magmas (Mg# < 65), plagioclase and clinopyroxene are the main fractionating phases. For example, trends between Mg# vs. Al_2O_3 and CaO (positive slopes in Fig. 7), Mg# vs. Fe_2O_3 (negative slope Fig. 7), and $Eu/Eu^* (=Eu_N/(Sm_N \times Gd_N)^{0.5}) < 1$ (Fig. 10d) indicate plagioclase fractionation for samples with Mg# < 65. As well, clinopyroxene fractionation is suggested by decreasing contents of CaO/Al_2O_3 with decreasing Mg# over the range of ~35–75 (Fig. 10c). In terms of accessory phases, chromite is an early crystallising phase for Mg# > 65, whereas titanomagnetite accumulation is important only for the Never Can Tell Basalt, where samples plot off the main trend in Ti-V space (Fig. 10b). This overall sequence of crystal fractionation for major phases (ol-pl-cpx) is evident in each complete cycle (Fig. 9).

Attempting to quantify crystal fractionation using major and minor elements of the Agnew suite without accounting for the effects of contamination would provide spurious results. Nevertheless, the general order of crystallisation is similar to what is expected of komatiites contaminated by granite at low pressures (ol-opx-pl-cpx; Sparks, 1986).

In summary, crystal fractionation and crustal contamination explains much of the geochemical variation in the Agnew dataset. Cycles I and II were generated from one magma source, excluding the Butchers Well Basalt and Bounty Igneous Complex, with each cycle becoming overall more evolved (fractionated) and crustally contaminated (Figs. 9 and 10b). Indeed, oblique trends in Th/Yb vs. Nb/Yb space (Fig. 10a), typical of many Archean ultramafic–mafic successions, are interpreted as evidence for

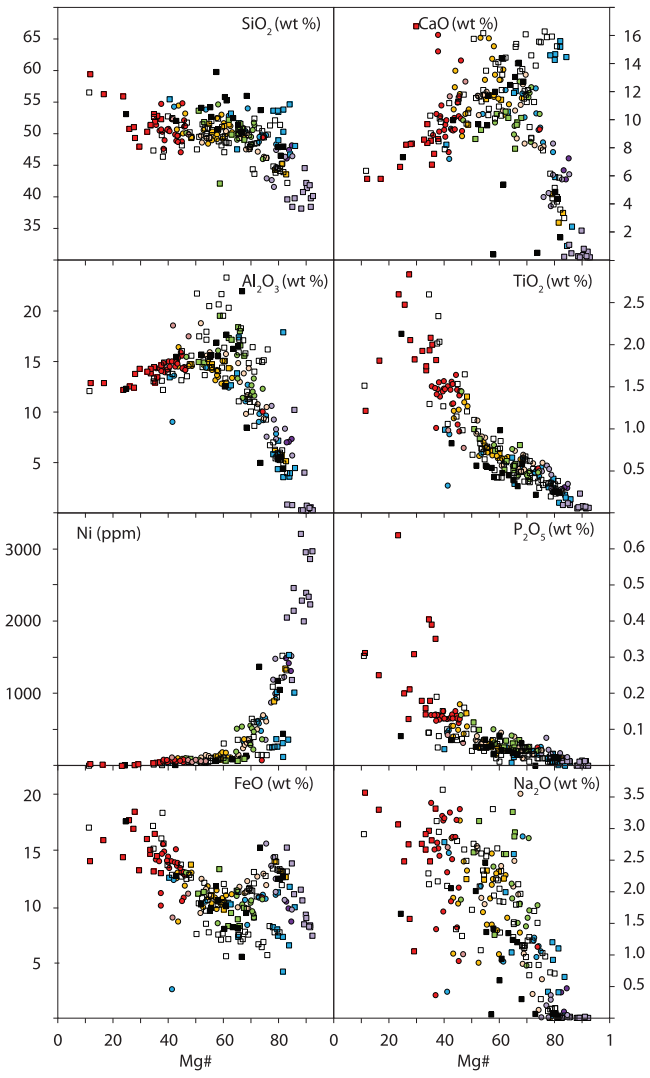

Fig. 7. Major element bivariate plots of the Agnew suite plotted against Mg# (molar). Trends are consistent with the Agnew mafic-ultramafic being genetically related, and that crystal fractionation is a significant process. Symbol legend in Fig. 6.

assimilation and fractional crystallisation processes (Pearce, 2008; Bédard, 2013).

6. Geochronology

A major difficulty in lithostratigraphic correlation of Archean greenstone belts composed of mainly mafic successions is the rarity of dateable minerals. Typically, the best way to determine the age of a mafic–ultramafic succession is by its crosscutting relations with dateable felsic or intermediate rocks, or from detrital zircon ages derived from intercalated sediments. Until now, the age of the Agnew Greenstone Belt was constrained from a single U/Pb zircon age from an interflow sediment (2692 ± 3; Kositcin et al., 2008). Four new samples were dated by this present study and permit a more precise characterisation of the timing of emplacement of the magmatism through direct dating of its comagmatic intrusions and interflow sediments.

Samples were collected in outcrop and from drill-core from granophyric intervals of mafic sills and from one thin siltstone interval. Granophyres were analysed at the Australian National University (ANU) while the siltstone was analysed at Curtin University, Western Australia. After removing weathered surfaces and inclusions, each sample (2–4 kg) was processed at either the ANU mineral separation lab, or at the Minsep Laboratories in Denmark, Western Australia at the Geological Survey of Western Australia Carlisle Laboratory. Samples were crushed using a jaw crusher, powdered using a ring mill, and sieved. Zircons were then concentrated using conventional density and magnetic methods, and isolated by hand-picking. Analytical results for each of the samples are presented hereafter.

6.1. TIMS dating

Three samples of granophyre, collected from mafic sills in the Agnew region, were dated by isotope dilution thermal ionization mass spectrometry (ID-TIMS) U–Pb analysis of zircons at ANU. Each sample yielded 35–50 zircon grains, which were annealed at 850 °C and leached in hydrofluoric acid at 180 °C in a procedure known as chemical abrasion (Mattinson, 2005, 2011) to remove parts of the grains damaged by radiation. Some grains from each sample were partially or completely disintegrated during chemical abrasion. This suggests that the radiation dose accumulated by these grains, or their parts, exceeded the threshold of the dose that causes damage of the zircon crystal lattice that can be cured by annealing. Between five and fifteen grains that survived chemical abrasion were analysed at the ANU SPIDE^{2}R lab using dissolution, chemical separation and data reduction similar to procedures of Amelin et al. (1999), and mass spectrometry, including spiking with a ^{202}Pb-^{205}Pb-^{233}U-^{236}U, mixed tracer for accurate fractionation correction for both Pb and U, similar to the procedures of Amelin et al. (2010). Preference was given to the grains with euhedral to subhedral shape, minimum fracturing, and no visible turbidity. The data were reduced using the algorithm of Schmitz and Schoene (2007). The grains were not weighted before analysis, and their weights could not be reliably estimated from the dimensions because partial dissolution during chemical abrasion makes their shapes complex, therefore the U and Pb concentrations were not determined. Instead, we report the quantities of U and total and non-radiogenic Pb for each analysed grain calculated from isotope dilution equations.

The ID-TIMS U–Pb data are presented in Table 5 and shown in concordia plots in Fig. 11. Zircons from all three samples have high model Th/U ratios between 0.6 and 3.6, consistent with an igneous origin. On the other hand, the content of non-radiogenic Pb, discordance of the U–Pb system, and the ^{207}Pb/^{206}Pb dates vary considerably between the grains in each sample, requiring a detailed data evaluation for each sample to decipher the patterns of the secondary processes. The data for the three granophyre samples are discussed in detail below.

No. 48 (VVDD178, 427–429 m) – granophyre from Turret Dolerite (collar location = MGA Zone 51, 261510, 6903260, 515).

Collected near the top of the Turret Dolerite, this rock consists of coarse-grained interlocking pyroxene and plagioclase crystals with interstitial quartz-feldspar granophyric intergrowths and lesser magnetite. It has since been modified through partial recrystallization, replacement of pyroxenes by hornblende and chlorite and calcite overprinting. The rock is classified as an upper greenschist to amphibolite facies granophyric meta-gabbro.

Analyses of 14 zircon grains form a linear array with substantial excess scatter in the concordia diagram (Fig. 11a). The lower intercept of this array of 219 ± 44 Ma, which significantly differs from the present day (zero) point, indicates that the zircons experienced Pb loss at present (during recent weathering and, possibly, chemical abrasion) and at a much earlier time. For such data, the upper concordia intercept of 2670 ± 15 Ma cannot be considered a reliable age estimate. A more reliable, and more precise, age of 2690.7 ± 1.2 Ma is given by a regression (Fig. 11b) through three concordant and

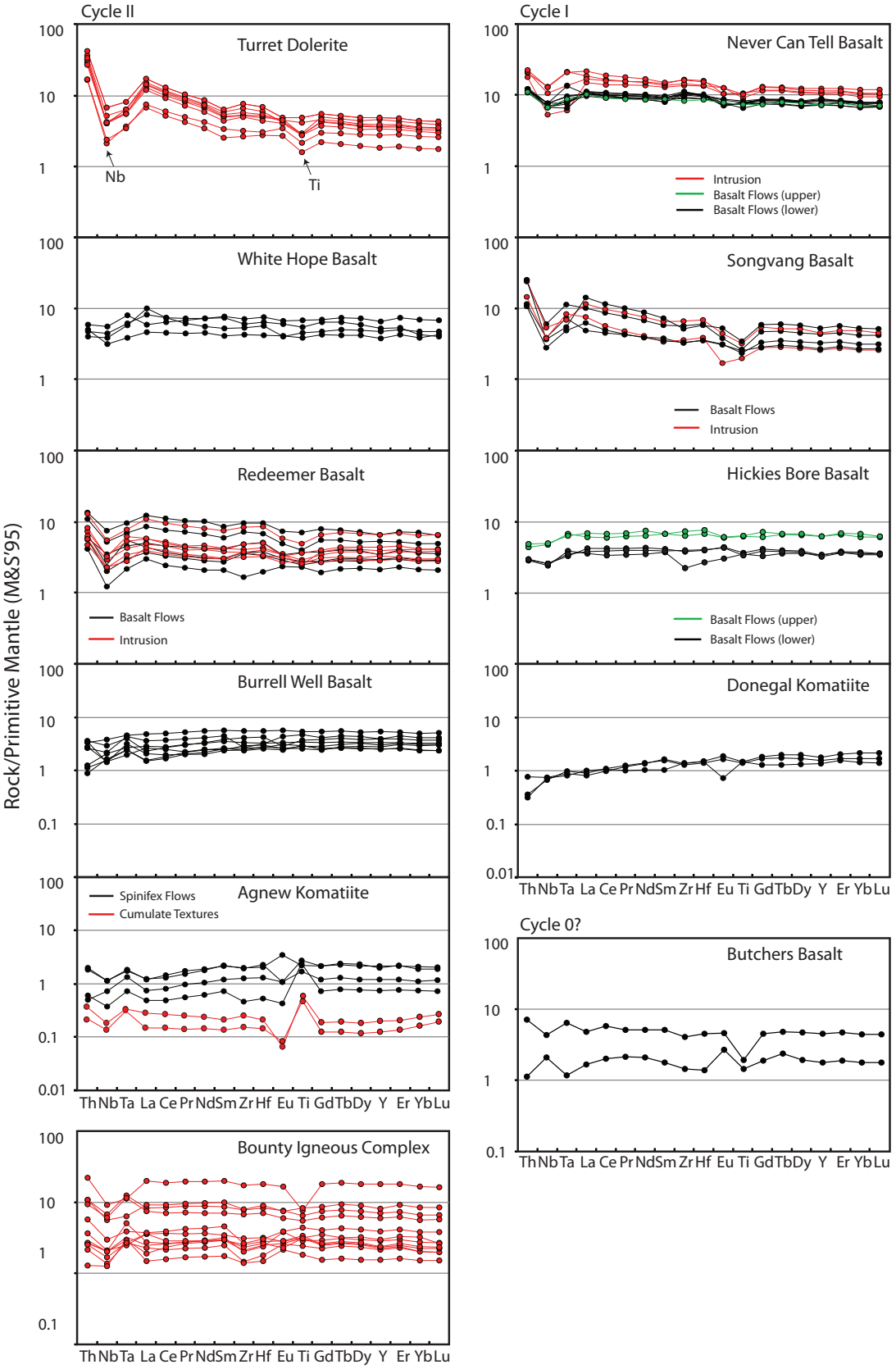

Fig. 8. Rare earth element plots, normalised to primitive mantle (McDonough and Sun, 1995), for each stratigraphic unit, grouped into cycles I and II. The Butchers Basalt is tentatively assigned to cycle 0, and Bounty Igneous Complex is ungrouped.

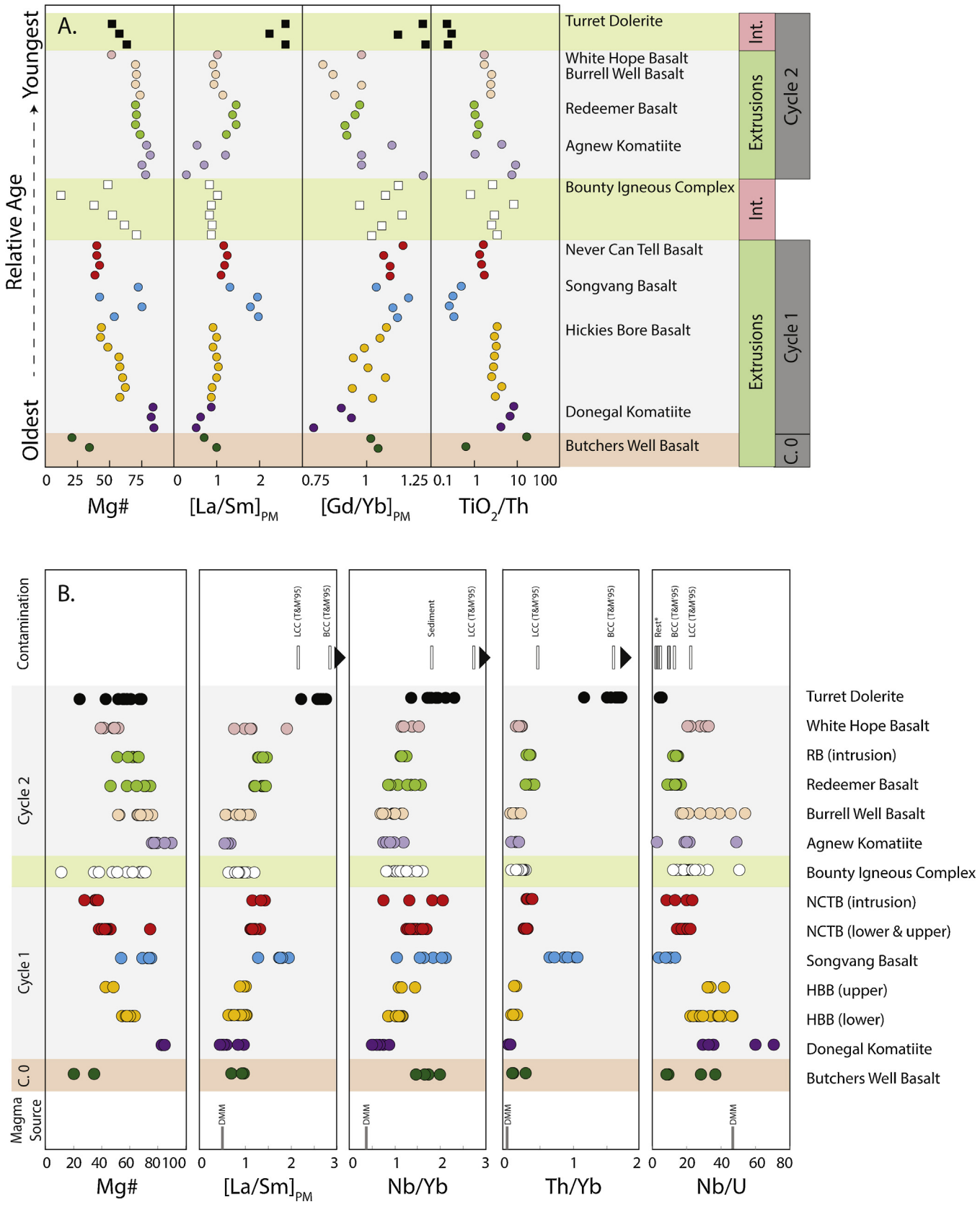

Fig. 9. Geochemical data arranged by relative time. (A) Subset of data of extrusive rocks types selected from only a few drillholes from which the relative timing is well constrained (Fig. 2). The order of extrusive lithofacies is well constrained, however, the order of samples from the Turret Dolerite and Bounty Igneous Complex reflect internal differentiation of mafic sills. (B) Data grouped by different stratigraphic unit. In some cases data are subdivided into upper, lower and comagmatic intrusions. Symbol legend as in Fig. 6.

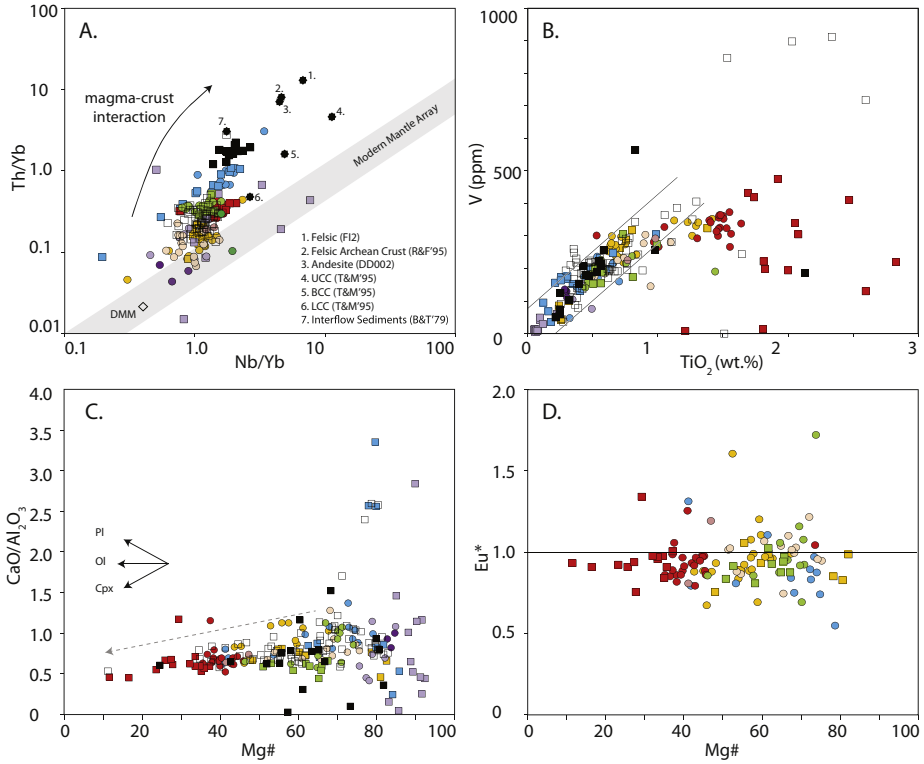

Fig. 10. Trace element diagrams tracking magma source, crustal contamination and crystal fractionation. (A) Th/Yb vs. Nb/Yb diagram demonstrating the Agnew data spreads out from ~depleted mantle (DMM) to a number of felsic/intermediate contaminants (diagram after Pearce, 2008). See explanation in text. R&F'95 = Rudnick and Fountain (1995), T&M'85 = Taylor and Mclennan (1985), B&T'79 = Bavinton and Taylor (1980). (B) Vanadium vs. TiO_2 plot demonstrating the data form a trend on which all the data plot, with the exception of the Never Can Tell Basalt. The data are interpreted as indicating origins from one magma source, and that the Never Can Tell Basalt crystallised under different fO_2 conditions (after Shervais, 1982). (C) CaO/Al_2O_3 vs. Mg# illustrating the strong control of pyroxene fractionation over plagioclase, and (D) Eu* vs. Mg# illustrating how many samples have values <1, exhibiting plagioclase removal. The Donegal and Agnew Komatiite, as well as Bounty Igneous Complex and Turrett Dolerite have been removed from d for clarity. Symbol legend in Fig. 6.

nearly concordant data points for grains 13–15. This is interpreted as the crystallisation age of the Turret Dolerite.

No. 45 (EMSD910, 464–487 m) – granophyre from Redeemer Basalt (collar location = MGA Zone 51, 256277, 6903060, 512).

A composite sample from a range of depths was collected from near the top of a mafic sill 100–400 m thick. The samples consist of coarse-grained interlocking pyroxene and plagioclase with lesser magnetite and patches of quartz-feldspar granophyric intergrowths. Pyroxenes have been completely replaced by hornblende and chlorite. The rock is interpreted as an upper greenschist to amphibolite facies meta-granophyric gabbro.

Three moderately discordant and one concordant zircon analyses (#2, 4, 5, 6) plot along a discordia line with a lower intercept of 650 ± 120 Ma and an upper intercept of 2686.8 ± 3.0 Ma (Fig. 11c). The latter value is considered the best age estimate for this sample. The $^{207}Pb/^{206}Pb$ date of 2685.3 ± 2.0 Ma of the concordant grain #6 is consistent with the upper intercept age. Analyses of the grains #1 and 3 (not shown in concordia diagram) have younger $^{207}Pb/^{206}Pb$ dates at the same level of discordance than the other four grains suggesting additional ancient alteration that caused loss of radiogenic Pb. The analyses of these two grains are not included in the age calculation.

The crystallisation age of this comagmatic intrusion to the Redeemer Basalt is interpreted as 2686.8 ± 3.0 Ma. However, because the lavas, based on field and geochemical constraints, must be older than the Turret Dolerite (2690.7 ± 1.2 Ma), the age is interpreted as being closer to the older end of the error bracket (~2690 Ma).

AG028 (SEIS-05, 874 m) – granophyre from Bounty Igneous Complex (MGA Zone 51, 252195, 6891312, -172).

This sample, collected 50 m below the top contact of a 260 m thick mafic sill, consists of patches (2–3 mm) of dark fine-grained hornblende (±magnetite) and light fine-grained quartz and plagioclase. The original rock consisted of coarse-grained pyroxene and plagioclase with minor granophyre, but has since been extensively recrystallised and the pyroxenes have been replaced by hornblende and chlorite.

U–Pb data for 15 grains show a rather complex pattern. All grains contained highly radiogenic Pb and yielded precise analyses, most of which show only moderate (<10%) amount of discordance, but in the concordia diagram (Fig. 11d) the data form an array with considerable scatter (MSWD = 82), and lower and upper intercepts of 220 ± 100 Ma and 2698.9 ± 5.8 Ma, respectively. However, 7 of 15 data points (#2, 5, 8–12) form a tight linear array with no excess scattering (MSWD = 1.3) and concordia intercepts at 221 ± 15 Ma and 2698.14 ± 0.95 Ma. These intercepts are consistent, within uncertainty, with the intercepts array defined by all data, but are much more precise. The nature of the apparent age dispersion in this sample is unclear. It is likely that the data that plot on the left side of the 7-point best-data array experienced more extensive ancient Pb loss, such as observed in the other samples. The origin of the higher $^{207}Pb/^{206}Pb$ dates of the grains #13–15 is less certain. They might have contained cores inherited from older crustal sources and assimilated by the dolerite. Another possibility is redistribution of radiogenic Pb within the zircon grains during an ancient metamorphic event, and that during chemical abrasion, grain domains depleted in radiogenic Pb where preferentially dissolved in comparison to grain domains enriched in radiogenic Pb. In any case, coincidental alignment of 7 precise zircon analyses in a concordia diagram, such as observed here, is highly improbable.

Table 5
TIMS analysis of zircons from granophyric zones of mafic sills from the Agnew Greenstone Belt.

Grain number	Included in age calc?	pg U	pg total Pb	pg non-rad. Pb	Th/U	$^{207}Pb/^{204}Pb$	$^{207}Pb/^{235}U$	% uncert.	$^{206}Pb/^{238}U$	% uncert	Rho	$^{207}Pb/^{206}UPb$	% uncert.	$^{206}Pb/^{238}U$	$^{207}Pb/^{235}U$	$^{207}Pb/^{206}UPb$	$^{207}Pb/^{206}UPb$	Discordance
		(b)	(b)	(b)	(c)	(corr.) (d)	(rad.) (d)	(d)	(rad.) (d)	(d)	(e)	(rad.) (d)	(d)	date (Ma) (f)	Age (Ma) (f)	Age (Ma) (a,f)	age uncert. (f)	% (g)
Sample no. 48: VVDD178-427 m: Turret Dolerite																		
1	no	68	9	1.15	1.31	59	1.906	0.74	0.09335	0.688	0.941	0.14806	0.25	575.3	1083.1	2323.6	4.3	75.2
2	no	139	30	0.93	0.86	245	3.931	0.31	0.17483	0.296	0.953	0.16308	0.09	1038.7	1620.1	2487.9	1.6	58.3
3	no	87	33	0.46	0.77	562	7.423	0.25	0.31121	0.237	0.955	0.17298	0.07	1746.6	2163.7	2586.7	1.2	32.5
4	no	81	32	5.85	1.25	51	6.683	0.34	0.27564	0.303	0.898	0.17584	0.15	1569.4	2070.3	2614.0	2.5	40.0
5	no	218	88	0.21	0.71	3501	8.345	0.31	0.34375	0.282	0.924	0.17608	0.12	1904.7	2269.3	2616.3	1.9	27.2
6	no	242	116	0.11	0.71	8366	9.886	0.32	0.40516	0.317	0.978	0.17697	0.07	2192.8	2424.2	2624.7	1.1	16.5
7	no	170	78	0.29	0.70	2224	9.478	0.23	0.38665	0.222	0.960	0.17778	0.06	2107.3	2385.4	2632.3	1.1	19.9
8	no	40	24	5.43	1.48	42	9.434	0.38	0.38439	0.335	0.903	0.17800	0.16	2096.7	2381.1	2634.4	2.7	20.4
9	no	184	107	11.25	1.05	84	10.876	0.23	0.43696	0.207	0.927	0.18053	0.08	2337.0	2512.6	2657.7	1.4	12.1
10	no	62	36	0.63	0.63	497	12.491	0.41	0.49360	0.402	0.980	0.18353	0.08	2586.2	2642.0	2685.1	1.4	3.7
11	no	82	49	0.76	0.64	557	12.803	0.23	0.50492	0.221	0.947	0.18390	0.07	2634.9	2665.3	2688.4	1.2	2.0
12	yes	41	27	2.20	0.90	111	13.191	0.37	0.51960	0.358	0.966	0.18412	0.10	2697.5	2693.4	2690.3	1.6	-0.3
13	yes	30	31	12.24	2.19	27	13.015	1.87	0.51226	1.84	0.986	0.18426	0.31	2666.3	2680.7	2691.6	5.1	0.9
14	yes	33	23	2.67	0.99	78	13.033	0.34	0.51285	0.322	0.944	0.18431	0.11	2668.8	2682.1	2692.1	1.9	0.9
Sample no. 45: ED910-464 m: Redeemer Basalt																		
1	no	9	5	0.21	0.68	239	11.236	1.24	0.45945	1.22	0.990	0.17736	0.17	2437.1	2542.9	2628.3	2.9	7.3
2	yes	4	4	0.60	3.67	50	11.169	2.25	0.45140	2.18	0.977	0.17945	0.48	2401.5	2537.3	2647.8	8.0	9.3
3	no	14	10	1.46	1.14	70	12.635	0.71	0.50564	0.679	0.964	0.18123	0.19	2638.0	2652.8	2664.2	3.2	1.0
4	yes	4	4	2.26	2.65	25	12.168	2.03	0.48559	1.79	0.919	0.18174	0.80	2551.6	2617.4	2668.8	13.2	4.4
5	yes	14	13	0.40	3.25	225	12.358	0.65	0.49233	0.627	0.972	0.18205	0.15	2580.7	2632.0	2671.7	2.5	3.4
6	yes	14	13	0.39	2.75	234	12.998	0.63	0.51358	0.61	0.982	0.18356	0.12	2671.9	2679.5	2685.3	2.0	0.5
Sample: AG028, SEIS05-874 m: Bounty Igneous Complex																		
1	no	53	37	1.17	1.77	271	12.183	0.26	0.48424	0.245	0.935	0.18247	0.09	2545.7	2618.6	2675.5	1.5	4.9
2	yes	186	113	1.07	1.83	857	10.476	0.55	0.41608	0.546	0.993	0.18261	0.06	2242.7	2477.8	2676.7	1.1	16.2
3	no	187	115	1.11	1.81	846	10.593	0.37	0.41937	0.362	0.984	0.18319	0.07	2257.6	2488.1	2682.0	1.1	15.8
4	no	10	7	0.17	1.15	359	12.968	0.94	0.51230	0.92	0.983	0.18358	0.17	2666.4	2677.3	2685.5	2.9	0.7
5	yes	41	26	0.20	1.61	1099	11.557	0.44	0.45655	0.428	0.984	0.18359	0.08	2424.3	2569.2	2685.5	1.3	9.7
6	no	17	11	0.13	1.01	788	12.728	0.65	0.50185	0.639	0.983	0.18395	0.12	2621.7	2659.7	2688.8	2.0	2.5
7	no	24	17	0.36	1.70	404	12.912	0.45	0.50865	0.435	0.973	0.18411	0.10	2650.9	2673.3	2690.3	1.7	1.5
8	yes	14	9	0.06	1.40	1426	12.132	0.89	0.47744	0.875	0.989	0.18429	0.13	2516.1	2614.6	2691.9	2.2	6.5
9	yes	8	6	0.06	1.39	912	12.987	1.21	0.51028	1.19	0.988	0.18458	0.19	2657.8	2678.7	2694.5	3.1	1.4
10	yes	29	19	0.06	1.12	3118	13.014	0.38	0.51085	0.374	0.977	0.18476	0.08	2660.2	2680.7	2696.1	1.3	1.3
11	yes	12	8	0.10	1.01	740	13.167	0.74	0.51632	0.727	0.982	0.18495	0.14	2683.6	2691.7	2697.8	2.3	0.5
12	yes	41	28	0.96	1.15	279	13.152	0.35	0.51548	0.331	0.956	0.18505	0.10	2680.0	2690.6	2698.6	1.7	0.7
13	no	23	15	0.05	1.25	2707	12.894	0.47	0.50476	0.454	0.981	0.18526	0.09	2634.2	2671.9	2700.6	1.5	2.5
14	no	294	198	0.15	1.49	11,252	12.554	0.60	0.49066	0.59	0.991	0.18557	0.08	2573.5	2646.8	2703.3	1.3	4.8
15	no	40	28	0.07	1.56	3607	13.234	0.49	0.51642	0.488	0.989	0.18586	0.07	2684.0	2696.5	2705.9	1.2	0.8

(a) Analyses are arranged by increasing $^{207}Pb/^{206}Pb$ dates.
(b) Quantities of U, total Pb and non-radiogenic Pb calculated from isotope dilution data. The grains were not weighted, therefore the concentrations cannot be calculated.
(c) Model Th/U ratio calculated from radiogenic $^{208}Pb/^{206}Pb$ and $^{207}Pb/^{206}Pb$ age.
(d) Atomic ratios corrected for blank, spike, fractionation and initial non-radiogenic Pb.
(e) Uncertainty correlation between $^{206}Pb/^{238}U$ and $^{207}Pb/^{235}U$ radiogenic ratios.
(f) Model dates calculated from radiogenic atomic ratios shown in columns (d), assuming $^{238}U/^{235}U = 137.88$
(g) Discordance of the U–Pb system. The values are positive if $^{207}Pb/^{206}Pb$ model date is older than $^{238}U/^{206}Pb$ model date.

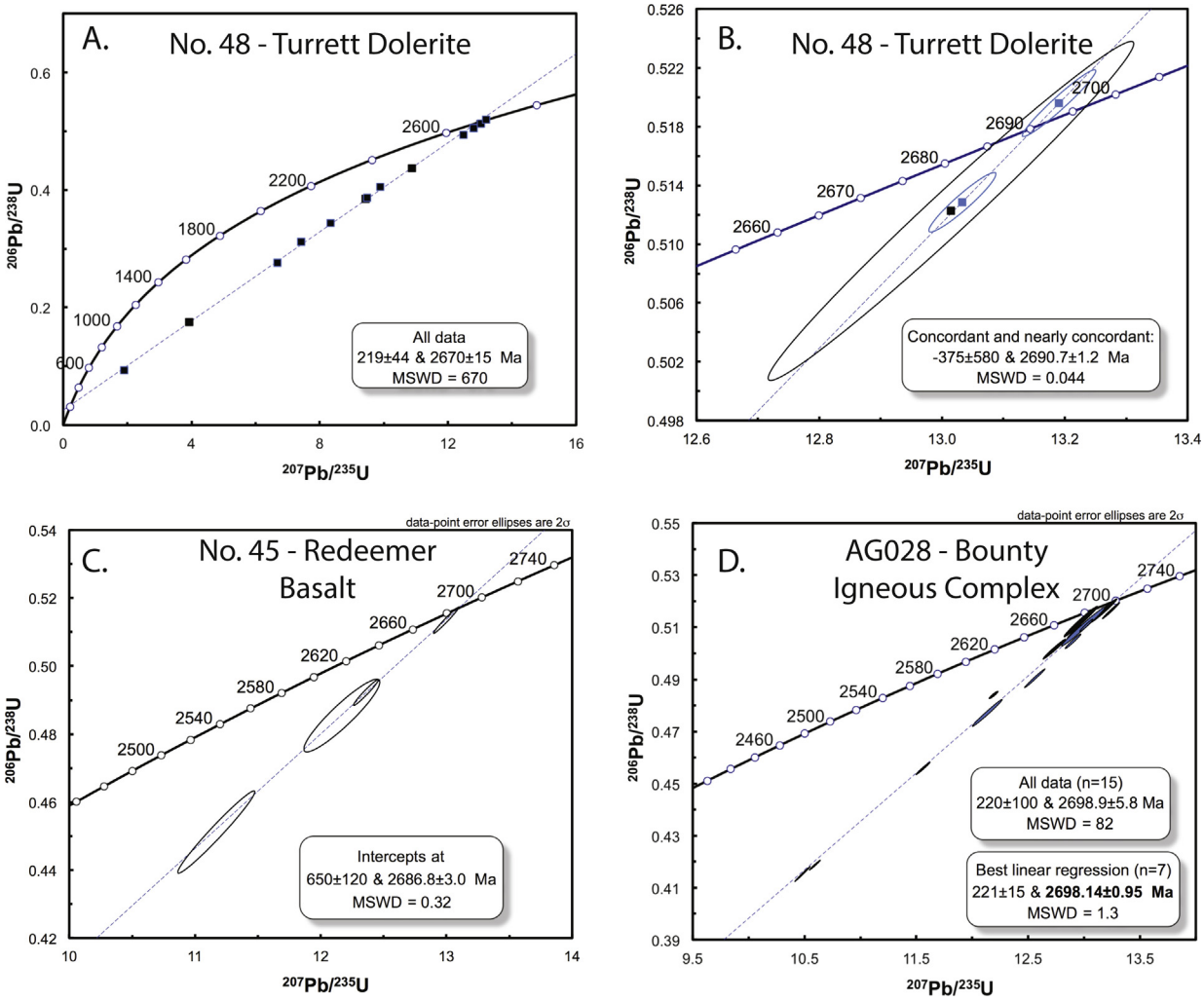

Fig. 11. $^{206}Pb/^{238}U$ vs. $^{207}Pb/^{238}U$ plots of TIMS data for mafic sills: (A) plot of all 14 zircons for Turrett Dolerite, (B) plot of three concordant and nearly concordant data points for Turrett Dolerite, (C) plot of three moderately discordant and one concordant zircon analyses of the Redeemer Basalt, and (D) plot of all 15 analyses with calculated age, and linear regression through seven points that form a tight linear array with no excess scattering, for the Bounty Igneous Complex (see text for more explanation).

Hence we interpret these grains as the least altered by the secondary processes, and the upper intercept age of 2698.14 ± 0.95 Ma as the best age estimate for crystallisation of the Bounty Igneous Complex.

6.2. SHRIMP dating

One siltstone sample was analysed using the sensitive high-resolution ion microprobe (SHRIMP II) at Curtin University. Zircons were mounted in 25 mm diameter epoxy-resin disks with chips of U/Pb zircon standard BR266 (559 Ma, 903 ppm U; Stern, 2001), crystals of zircon $^{207}Pb/^{206}Pb$ standard OGC1 (3465 Ma; OG1 of Stern et al., 2009), and NBS610 glass. Cathodoluminescence (CL) and backscattered electron (BSE) imaging on gold-coated mounts were performed using a Philips XL30 scanning electron microscope (SEM) at the Department of Imaging and Applied Physics at Curtin University in Perth, Western Australia, and a JEOL 6400 SEM at the Centre for Microscopy and Microanalysis at the University of Western Australia.

Analysis was conducted using standard operating procedures similar to those described by Compston et al. (1992) and Wingate and Kirkland (2014). The diameter of the primary ion probe used during all sessions was about 20 μm. Six data collection cycles (scans) were performed per analysis, and count times (per scan) were 10 s for the ^{204}Pb, ^{206}Pb, and ^{208}Pb mass peaks and background, and 30 s for the ^{207}Pb mass peak. Analyses of unknown zircons were referenced to multiple analyses of the BR266 standard for U/Pb calibration. Calibration and reproducibility uncertainties are included in the errors of $^{238}U/^{206}Pb$ ratios and dates listed in supplementary papers. Data reduction was carried out using the software SQUID v2.2 and 2.5 and ISOPLOT v3.0 (MS Excel add-ins by Ludwig, 2003, 2009). Corrections for common Pb were based on measured ^{204}Pb, assuming an average crustal composition (Stacey and Kramers, 1975) appropriate to the age of the mineral. Mean ages are quoted below with 95% uncertainties (MSWD; Ludwig, 2003).

The SHRIMP data are listed in Table 6 and illustrated in concordia diagrams (Fig. 12). The data for the siltstone sample are discussed in detail below.

Sample PHAG020–siltstone (MGA Zone 51, 274419, 6880993)

This siltstone layer within the Never Can Tell Basalt consists of a microcrystalline quartz and albite (70%), well-aligned foliated sericite (25%) and fine-grained to medium-grained muscovite micro-porphyroblasts (5%) overgrowing foliation. Zircon forms a trace component. The rock is classified as an upper greenschist to amphibolite facies meta-siltstone, which underwent late stage post-kinematic metamorphism. Zircons are clear and colourless to dark brown, and up to 200 μm long. Most of the zircons isolated

Table 6
SHRIMP II results for zircons from siltstone sample PHAG020 from the Agnew Greenstone Belt.

Group ID	Spot no.	f204 (%)	^{238}U (ppm)	^{232}Th (ppm)	^{232}Th/^{238}U	^{206}Pb*/^{238}U date (Ma) ± 1σ		^{207}Pb*/^{206}Pb* date (Ma) ± 1σ		^{238}U/^{206}Pb ± 1σ		^{207}Pb/^{206}Pb ± 1σ		^{238}U/^{206}Pb* ± 1σ		^{207}Pb*/^{206}Pb* ± 1σ		Disc (%)
(a)		(b)								(c)				(d)				(e)
A	A-15-1	−0.037	77	32	0.426	2762	67	2700	10	1.87	3	0.1848	0.57	1.87	3.1	0.1852	1.04	-3
A	a-1-1	0.407	128	70	0.565	2759	37	2713	9	1.865	1.7	0.19036	0.44	1.872	1.9	0.18671	1.03	-2
A	A-18-1	−0.094	55	25	0.464	2744	68	2706	11	1.886	3.1	0.185	0.64	1.885	3.2	0.1858	1.1	-2
A	A-19-1	0.085	62	26	0.424	2751	68	2728	11	1.877	3	0.1891	0.62	1.879	3.1	0.1883	1.08	-1
A	A-12-1	0.052	102	68	0.69	2711	64	2701	8	1.912	2.9	0.1858	0.48	1.913	3	0.1853	1	0
A	A-20-1	0.047	121	90	0.765	2708	63	2700	8	1.915	2.9	0.1856	0.46	1.915	3	0.1852	0.98	0
A	A-7-1	−0.1	120	55	0.471	2704	63	2717	8	1.921	2.9	0.1862	0.47	1.919	3	0.1871	0.99	1
A	A-16-1	0.095	72	28	0.395	2682	65	2698	10	1.936	3	0.1858	0.58	1.938	3.1	0.185	1.06	1
A	A-6-1	0.01	170	102	0.618	2693	62	2714	7	1.928	2.8	0.1869	0.42	1.928	3	0.1868	0.96	1
A	A-14-1	−0.014	88	42	0.491	2696	64	2720	8	1.926	2.9	0.1873	0.5	1.926	3	0.1874	1	1
A	A-2-1	−0.07	90	43	0.491	2681	64	2716	10	1.94	2.9	0.1864	0.56	1.939	3.1	0.187	1.04	2
A	A-5-1	0.304	148	83	0.575	2684	63	2721	9	1.93	2.9	0.1902	0.47	1.936	3	0.1875	1.02	2
A	a-2-1	−0.041	85	41	0.496	2695	38	2736	12	1.928	1.7	0.18893	0.55	1.927	1.9	0.1893	1.11	2
A	a-5-1	0.073	161	85	0.544	2644	35	2711	8	1.971	1.6	0.18713	0.44	1.972	1.8	0.18649	0.96	3
A	A-1-1	0.031	104	46	0.46	2636	63	2710	9	1.979	2.9	0.1866	0.52	1.979	3	0.1863	1.01	3
A	A-8-1	0.026	159	149	0.968	2625	61	2709	7	1.989	2.8	0.1864	0.4	1.989	2.9	0.1862	0.95	4
A	a-6-1	0.1	162	90	0.574	2622	37	2709	14	1.99	1.7	0.18709	0.66	1.992	1.9	0.18622	1.22	4
A	a-7-1	0.123	91	55	0.616	2622	38	2714	12	1.99	1.8	0.18792	0.71	1.992	2	0.18683	1.13	4
D	a-4-2	0.098	299	231	0.798	2899	38	2708	6	1.76	1.6	0.18703	0.3	1.761	1.8	0.18613	0.92	-9
D	a-2-2	0.036	257	187	0.75	2895	37	2706	6	1.763	1.6	0.18625	0.31	1.764	1.8	0.18592	0.92	-9
D	a-3-1	0.072	99	53	0.554	2833	39	2710	9	1.811	1.7	0.18701	0.52	1.812	1.9	0.18635	1	-6
D	a-4-1	0.406	63	27	0.446	2826	40	2714	21	1.81	1.8	0.19042	0.65	1.817	2	0.18676	1.51	-5
D	A-17-1	0.047	90	71	0.82	2551	61	2693	9	2.059	2.9	0.1849	0.53	2.06	3	0.1844	1.02	6
D	a-8-1	0.029	82	71	0.893	2575	36	2719	10	2.036	1.7	0.18765	0.55	2.037	1.9	0.18739	1.05	6
D	A-13-1	−0.036	80	65	0.841	2550	62	2697	10	2.062	2.9	0.1846	0.56	2.061	3.1	0.1849	1.03	7
D	A-4-1	0.013	146	99	0.7	2517	59	2710	8	2.093	2.8	0.1865	0.48	2.094	3	0.1863	0.99	9
D	a-3-2	−0.173	58	38	0.671	2478	36	2687	16	2.137	1.8	0.18221	0.76	2.133	2	0.18371	1.3	9
D	A-3-1	−0.172	94	48	0.527	2188	54	2669	12	2.479	2.9	0.1802	0.68	2.475	3.1	0.1818	1.14	21

(a) A = concordant or slightly discordant grains included in age calculations, D = grains >5% discordant, excluded from calculations.
(b) f204 is the fraction of common ^{206}Pb in total ^{206}Pb, estimated using 204Pb.
(c) Analyses are listed by increasing ^{207}Pb*/^{206}Pb* date.
(d) Pb* = radiogenic Pb.
(e) Disc = discordance (%), calculated as $100 \times [1 - (^{238}\text{U}/^{206}\text{Pb*}\ \text{date})/(^{207}\text{Pb}/^{206}\text{Pb*}\ \text{date})]$.

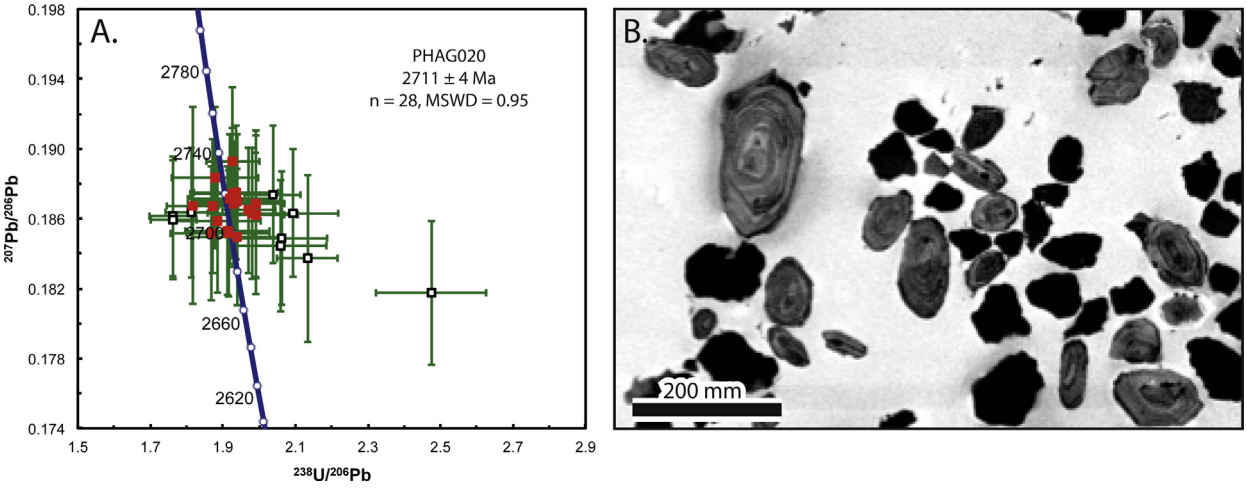

Fig. 12. SHRIMP results for siltstone sample PH020. (A) $^{207}Pb/^{206}Pb$ vs. $^{238}U/^{206}Pb$ plot of 28 zircons, and (B) cathodoluminescence image of representative grains (see text for more explanation).

display subhedral to euhedral crystal forms shapes with aspect ratios of up to 3:1. In cathodoluminescence (CL) images, concentric growth zoning is found in the majority of zircon. Some of the zircons were partially to complexly metamict displaying high-uraniuam zones and mottled textures. Twenty-eight analyses were obtained from 28 zircons (Fig. 12). Ten analyses >5% discordant were not included in the age calculation. The remaining 18 analyses are concordant to slightly discordant and yield a weighted mean $^{207}Pb^*/^{206}Pb^*$ date of 2711 ± 4 Ma (MSWD = 0.95). This is interpreted as the depositional age of the sediment, interpreted as an air-fall deposit from a distal felsic pyroclastic eruption.

7. Discussion

7.1. Reconstruction of events

7.1.1. One large igneous province (~30 Ma) represented by two cycles of magmatism

The ultramafic–mafic stratigraphy at Agnew represents a ~7 km succession of subaqueous lavas and comagmatic intrusions, as well as mafic sills without associated extrusions, all of which form a stacked flow field. The lateral continuity of the extrusive units, absence of coarse-grained sediments or re-sedimented successions, as well as the predicted low magma viscosity, suggest there was little topographic relief. Magma volume calculations are poorly constrained, but considering the belt extends for 100s of kilometres (Section 7.2); SHRIMP, TIMS and detrital zircon data indicate volcanism spanned ~30 m.y. without major time breaks (see below); and there are no unconformities to suggest major time breaks, the greenstone belt can be considered a large igneous province (Bryan and Ernst, 2008; Ernst et al., 2013). Other studies provide convincing evidence that some, if not all, of the Kalgoorlie Terrane is underlain by older (>3 Ga) basement (Oversby, 1975; Compston et al., 1986; Campbell and Hill, 1988; Hill et al., 1989; Champion and Cassidy, 2007; Mole et al., 2012; Wyche et al., 2012), and thus the sequence was built on felsic rather than oceanic crust.

The eruption source(s) for the flow field is unknown, but by inference from other large igneous provinces (White et al., 2009), magmas were likely erupted through a network of fissures. Aside from the inter-fingering relationship between the Burrell Well and Redeemer Basalts, all other extrusive units form a layer cake stratigraphy, indicating that each magma batch was erupted before eruption of the next batch.

The base of the exposed sequence is made of the Butchers Well Basalt. Without further timing constraints, it is unclear if it is part of the same magmatic event as the overlying cycle I, or part of older basement. Insight into rock forming events is provided by detrital zircon data of the Agnew region (Dunphy et al., 2003; Squire et al., 2010). These data provide ages of exposed rocks during sedimentation, and demonstrate a large spread of ages from ~2650 to ~2720 Ma, with a gap of ~50 m.y., and then another well-defined group of age data from ~2770 to 2830 Ma, which is best interpreted as part of the old basement (Fig. 13). The Butchers Well Basalt may be part of the same thermal event as cycles I and II, or it may belong to an older >~2770–2830 Ma event. We tentatively assign this unit to cycle 0.

The onset of cycle I magmatism is constrained by the oldest date in the cycle (2711 ± 4 Ma), which is from an interflow sediment near the top of cycle I. This age indicates that cycle I volcanism is associated with the ~2650–2720 Ma thermal event highlighted by the detrital zircon dataset. We suggest the onset of cycle I magmatism is ~2720 Ma, although it could be older if the oldest rocks were not

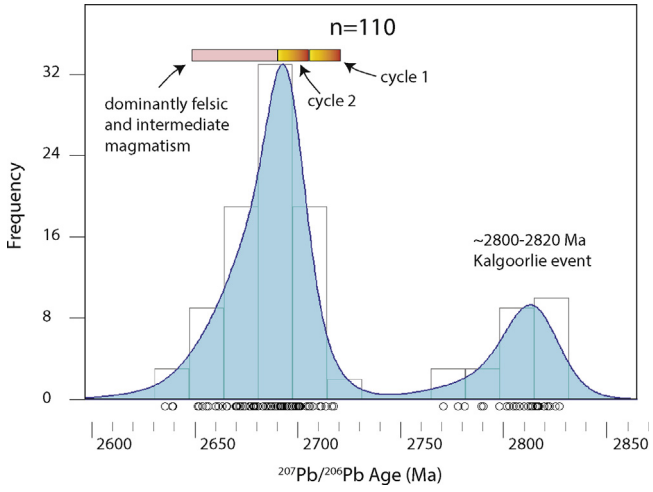

Fig. 13. Kernel density plot (blue shaded region) and histogram (light grey rectangles) for detrital zircons (Dunphy et al., 2003; Squire et al., 2010) recovered from sediments overlying the ultramafic–mafic stratigraphy at Agnew. The lone constraint from this study places cycle I in the younger group of the bimodal dataset. Data plotted using DensityPlotter (Vermeesch, 2012) (For interpretation of the references to colour in this figure legend, the reader is referred to the web version of this article.).

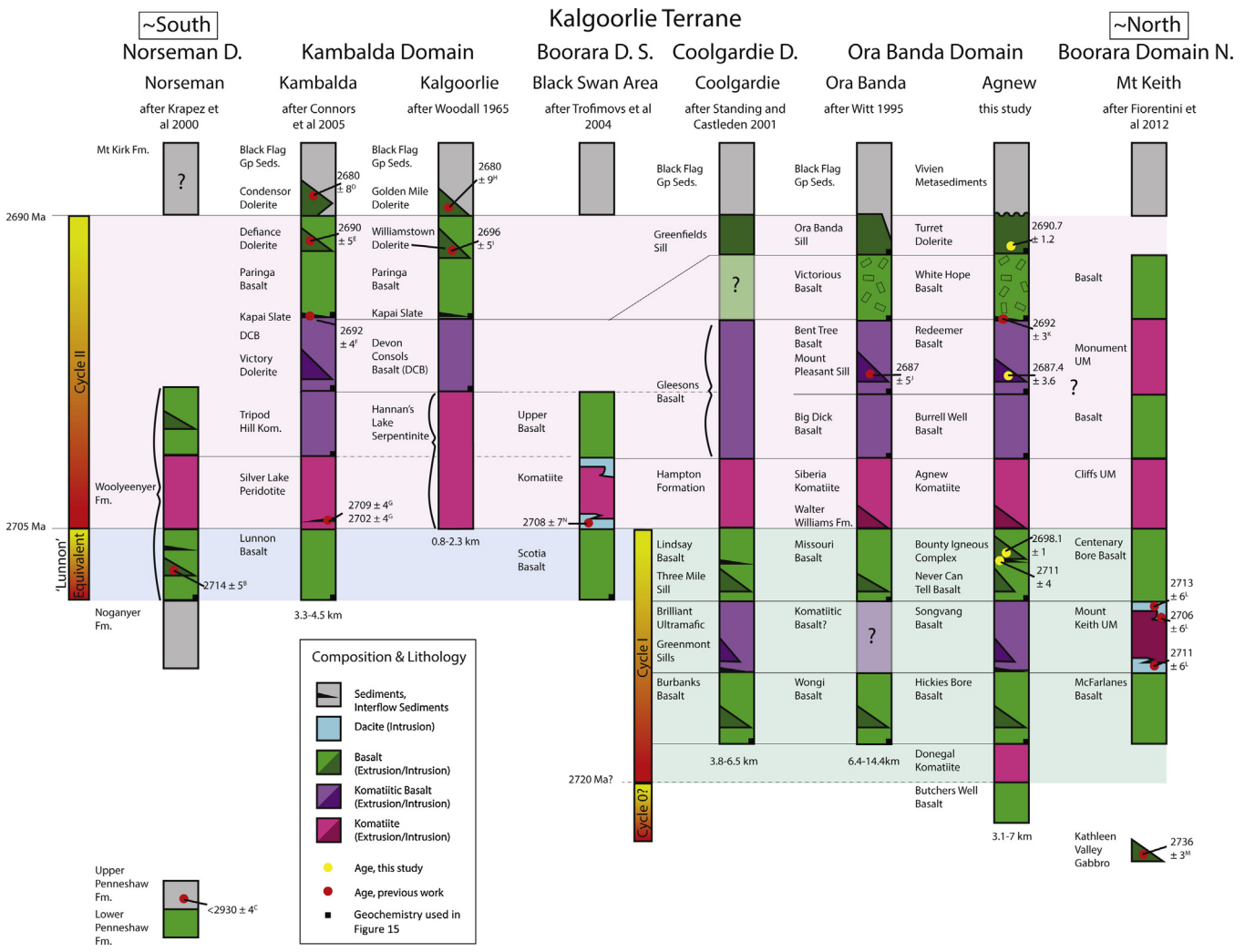

Fig. 14. Stratigraphic relationships of the principal mafic–ultramafic units of the Kalgoorlie Terrane based on comparing geochronology as well as the order and geochemistry of stratigraphic units in this study with published geochronology, stratigraphy and geochemistry. Vertical positions are an approximation of their relative stratigraphic positions. See text for further explanation. A, stratigraphic column modified after Barley et al. (2008), B, granophyric interval of mafic intrusion (Hill et al., 1992), C, detrial zircons, maximum depositional age, U–Pb SHRIMP (Nelson, 1995), D, granophyre, U–Pb zircon SHRIMP (Carey, 1994), E, Defiance Dolerite (Clout, 1991), F, Interflow sediment, U–Pb zircon SHRIMP (Claoue-Long et al., 1988), G, Interflow sediment near base on Kambalda Komatiite U–Pb zircon SHRIMP (Campbell and Hill, 1988); H, granophyre, U–Pb zirconolite and xenotime SHRIMP (Rasmussen et al., 2009). I, granophyre, U–Pb SHRIMP (Fletcher et al., 2001), J, granophyre, U–Pb zircon (I.H. Campbell, 1988 unpublished, referenced in Kent and McDougall, 1995), K, detrial zircons, maximum depositional age, U–Pb SHRIMP (Kositcin et al., 2008), L, U–Pb SHRIMP, crystallisation age of dacite (Fiorentini et al., 2012), M, Tonalite from Kathleen Valley Gabbro, U–Pb zircon, SHRIMP (Black et al., 2002), and N, Dacite intrusion, U–Pb zircon (Claoue-Long et al., 1988). Minimum and maximum stratigraphic thickness listed below each column, calculated by summing the thickness variations listed for each stratigraphic column from the references provided at top.

exposed during sedimentation. For example, around the Cosmos Nickel Mine, 25 km north of Agnew, ages up to ~2736 Ma are known (Black et al., 2002; de Joux et al., 2013) and could be related to cycle I. The ~2800 Ma event is the next older major known crustal forming event in the Yilgarn (e.g., Pawley et al., 2012; Wyche et al., 2012). However, linking this with the cycle I would require magmatism to span >90 m.y., which we think is unlikely given that the lifespan of most large igneous provinces is <50 m.y. (Bryan and Ernst, 2008), and is more difficult to reconcile with the large gap in detrital zircon ages. Because there is no inter-fingering of the Never Can Tell Basalt and Agnew Komatiite, cycle I ended before the onset of cycle II. Termination of cycle I magmatism is constrained by the youngest date from cycle I (<2711 ± 4 Ma) and the oldest cycle II date (>2692 ± 3; Kositcin et al., 2008). The Agnew Komatiite heralds the beginning of cycle II, and is estimated, based on regional correlations, to be ~2705 Ma (Fig. 14, Section 7.2.5). Termination of cycle II magmatism is well constrained from this study by dating the youngest mafic unit in the sequence at 2690.7 ± 1.2 Ma.

Constraints on the average duration of each individual volcanic event (i.e., stratigraphic unit) are provided by the total duration of cycles I and II (interpreted here as 30 m.y.), and the number of individual events (9); this gives a maximum average duration of 3.3 m.y. However, this does not account for the fact that individual lava flows were likely emplaced rapidly, whereas the time to accumulate the thin sediment intervals would have been extremely long. When considering Phanerozoic large-igneous provinces, which are characterised by pulses of magmatism spanning 0.5–1 m.y. (Bryan and Ernst, 2008), it is reasonable to presume similar lengths of time for the individual volcanic events at Agnew, and that sedimentation took longer to accumulate than the entire volcanic sequence. The ~30 m.y. lifespan for the ultramafic–mafic event is longer than that of most Phanerozoic large igneous provinces, but well within the typical range (generally 5–15 m.y., up to 50 m.y.; Bryan and Ernst, 2008).

The Agnew section is most easily explained as the product of one large igneous province, rather than two overlapping provinces,

which would require a number of special circumstances. Firstly, the spread of detrital zircon ages, from ~2650 to ~2720 Ma, suggest one thermal event, rather than two (Fig. 13). Secondly, both cycles are sourced from magmas of similar composition (Figs. 9b and 10a). And lastly, there is no interfingering of cycles I and II, which indicates there was no time overlap between cycle emplacement. Although we cannot exclude the possibility of two separate large igneous provinces, the data is more easily explained by one province formed by two cycles.

Another aspect we considered is the magma's pathway through the crust. Archean thermal events heat the crust through magmatic intraplating, magmatic underplating, conduction and thermal blanketing such that partial melting generates voluminous granitic domes (Campbell and Hill, 1988; Rey et al., 2003). In the Kalgoorlie Terrane, crustal melting is initiated at ~2700 Ma, with peak granitic magmatism at ~2665 Ma (Champion and Sheraton, 1997). The time-lag between the arrival of the thermal event and crustal melting ranges from ~20 to 40 m.y., with peak granitic magmatism at ~40 m.y. after the onset of the thermal event (Rey et al., 2003). Although the estimated timescales at Agnew are shorter, after ~15 m.y. of conductive heating and transfer of melt from the mantle to the crust, it is likely that some degree of partial melting in the crust had already begun. As a result, it is not clear how the first magmatic products of cycle II could have erupted through the same hot conduits as cycle I without displaying any signs of crustal contamination. An explanation is also required for the uncontaminated Bounty Igneous Complex. One model is that the second cycle exploited a different, not yet heated, conduit through the crust. This may reflect progressive eastward migration of rifting of the Kalgoorlie Terrane and magma ascent paths (Fig. 16). An alternative 'single-conduit' model, proposed by others to explain similar relationships elsewhere, is that thermal erosion of wall rocks only occurs during turbulent flow, and once flow rates wane, chilled margins develop and consequently, late erupting magmas remain uncontaminated (Lesher and Arndt, 1995; Hollings and Kerrich, 1999).

In summary, based on lithostratigraphy, geochemistry and geochronology, and by comparison with other large igneous provinces, the Agnew section is interpreted as one large igneous province having formed by several punctuated mafic-ultramafic volcanic events over ~30 m.y. that can be grouped into two ~15 m.y. cycles.

7.1.2. Sub- and intra-crustal magma chambers

Geochemical data are consistent with cycles I and II forming by the pooling and stalling of komatiitic melts in crustal magma chambers where, to various degrees, the parent magmas assimilated wall rock and underwent crystal fractionation. Intermediate storage chambers are invoked for several reasons. Firstly, element ratios within many individual stratigraphic units are uniform, which indicates that each erupting magma batch was relatively homogeneous, yet distinct from the overlying conformable stratigraphic unit (e.g., see TiO_2/Th; Fig. 9). This observation is best explained through assimilation and fractional crystallisation followed by convection and mixing in a magma chamber, before eruption (e.g., Barnes et al., 2012). If all of the assimilation happened during magma ascent one would expect to find gradational compositional changes in successively younger extrusive units. Also, the large degrees of crystal fractionation we infer occur on time scales more consistent with residence in magma chambers (Hawksworth et al., 2000), than during uninterrupted magma ascent (Rutherford, 2008). Lastly, the thin sediment intervals indicate time breaks in volcanism, and provide the necessary time for assimilation, fractionation and homogenisation. Although each cycle displays an overall progression, in detail, the cycles do not follow a strict progression from primitive melts to progressively more fractionated and contaminated melts (Fig. 9). We explain this by invoking multiple magma chambers and suggest that fractionation and assimilation of crust occurred at different rates. Similar sub-crustal and intra-crustal magma chambers have been invoked for a number of Phanerozoic large igneous provinces (East African Rift: Coleman and McGuire, 1988; southeast Greenland: Fitton et al., 2000).

7.2. Correlations in the Eastern Goldfields Superterrane

The Kalgoorlie Terrane (KT) has been previously subdivided, based on lithology, geochemistry and geochronology, into a number of domains that are separated from each other by NNW-trending regional faults (Fig. 1b) (Nelson, 1997; Swager, 1997; Cassidy et al., 2006; Barley et al., 2008). We mainly use the scheme of Cassidy et al. (2006), which identifies 10 domains within the Kalgoorlie Terrane. Well constrained stratigraphy is restricted to the Ora Banda and Kambalda Domains in the southern Kalgoorlie Terrane, and less well defined stratigraphic columns exist for the Coolgardie, Norseman and Boorara Domains. For our correlations, we compare our Agnew data with all available published geochemical and geochronological data for the defined stratigraphic columns across the Kalgoorlie Terrane (Fig. 14).

7.2.1. Ora Banda Domain

The Agnew greenstone belt occurs in the northern Ora Banda Domain, which can be traced from Agnew to the south for ~260 km (Fig. 1b) (Wyche and Witt, 1991; Witt, 1993, 1995; Tranthem, 2004; Cassidy et al., 2006; Barley et al., 2008; Said et al., 2010). The stratigraphic, geochemical and geochronological data from Ora Banda correlates well with the Agnew area (Figs. 14 and 15). The Wongi Basalt makes up the lowermost unit and is an excellent geochemical match with the Hickies Bore Basalt (Fig. 15). There is no defined unit at Ora Banda that relates to the Songvang Basalt, however, the Wongi Basalt has also been described as Mg-rich basalt (Witt, 1995) and 'Paringa-like' (Barley et al., 2008); descriptions that could also describe the Songvang Basalt. Overlying the Wongi Basalt is the Missouri Basalt, which is an excellent geochemical match with the Never Can Tell Basalt. The Missouri Basalt is geochemically distinct (Mg# <50 and high contents of incompatible elements) from other basalts at Ora Banda and is absent from the well-defined Kambalda sequence. The next overlying units are the ultramafic Walter Williams Formation and then the Siberia Komatiite, which correlate with the Agnew Komatiite cumulate and spinifex flows, respectively. The overlying Big Dick Basalt and Bent Tree Basalt match the chemistry of the Burrell Well and Redeemer Basalts, respectively (Fig. 15). The Mount Pleasant Sill (2687 ± 5 Ma, Kent and McDougall, 1995), hosted in the Bent Tree Basalt, correlates to the comagmatic intrusion within the Redeemer Basalt, dated in this study at 2687.4 ± 3.6 Ma. Witt (1993) linked the Mount Pleasant Sill to the Devon Consols Basalt in the Kambalda Domain, which is consistent with our correlations. Overlying this is the Victorious Basalt, a feldspar megacrystic basalt that is texturally and geochemically similar to the White Hope Basalt (Fig. 15). The Ora Banda Sill, which occurs at the top of the sequence and below the Black Flag Group Sediments, has no published geochemistry, but is described as a strongly enriched komatiitic basalt similar in composition to the Paringa Basalt (Barley et al., 2008), and thus a reasonable correlate to the Turret Dolerite (Fig. 15).

7.2.2. Kambalda Domain

The Kambalda Domain (Lesher and Arndt, 1995; Cassidy et al., 2006) extends south-southeast from Kalgoorlie to the southern boundary of the Kalgoorlie Terrane (similar to the Kalgoorlie Domain of Woodall, 1965), and comprises a relatively simple stratigraphy. The lowermost unit is the tholeiitic Lunnon Basalt.

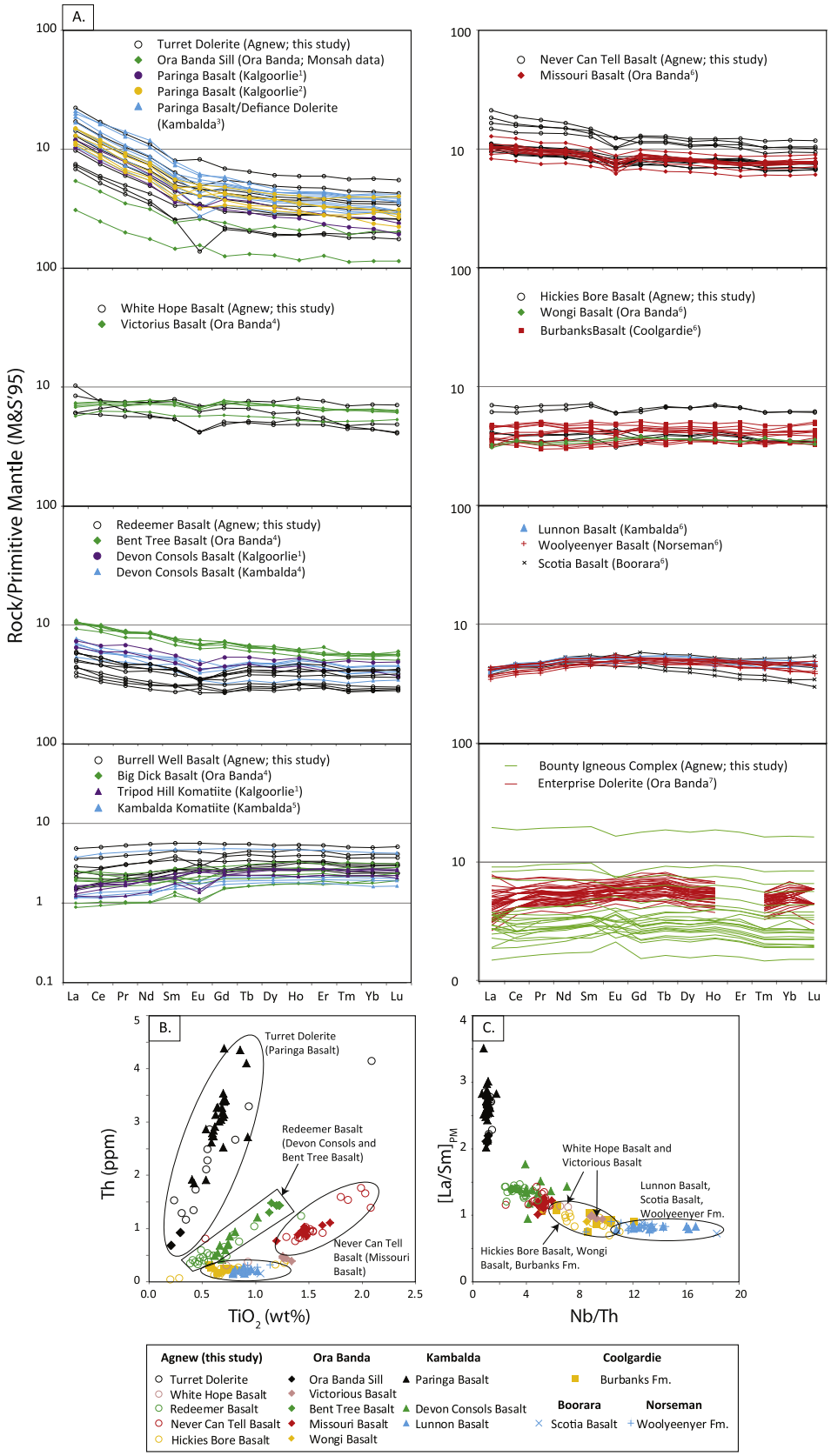

Fig. 15. Comparison of geochemistry from Agnew (this study) with available published geochemistry for domains within the Kalgoorlie Terrane. (A) Rare Earth element plots, (B) Th vs. TiO_2 and (C) $[La/Sm]_{PM}$ vs. Nb/Th. [1]Bateman et al. (2001); [2]Said and Kerrich (2009); [3]Timmermans (2010); [4]Said and Kerrich (2010); [5]Arndt and Jenner (1986); [6]Said et al. (2010); [7]Gregory (1998). Note: legend applies only to (B) and (C).

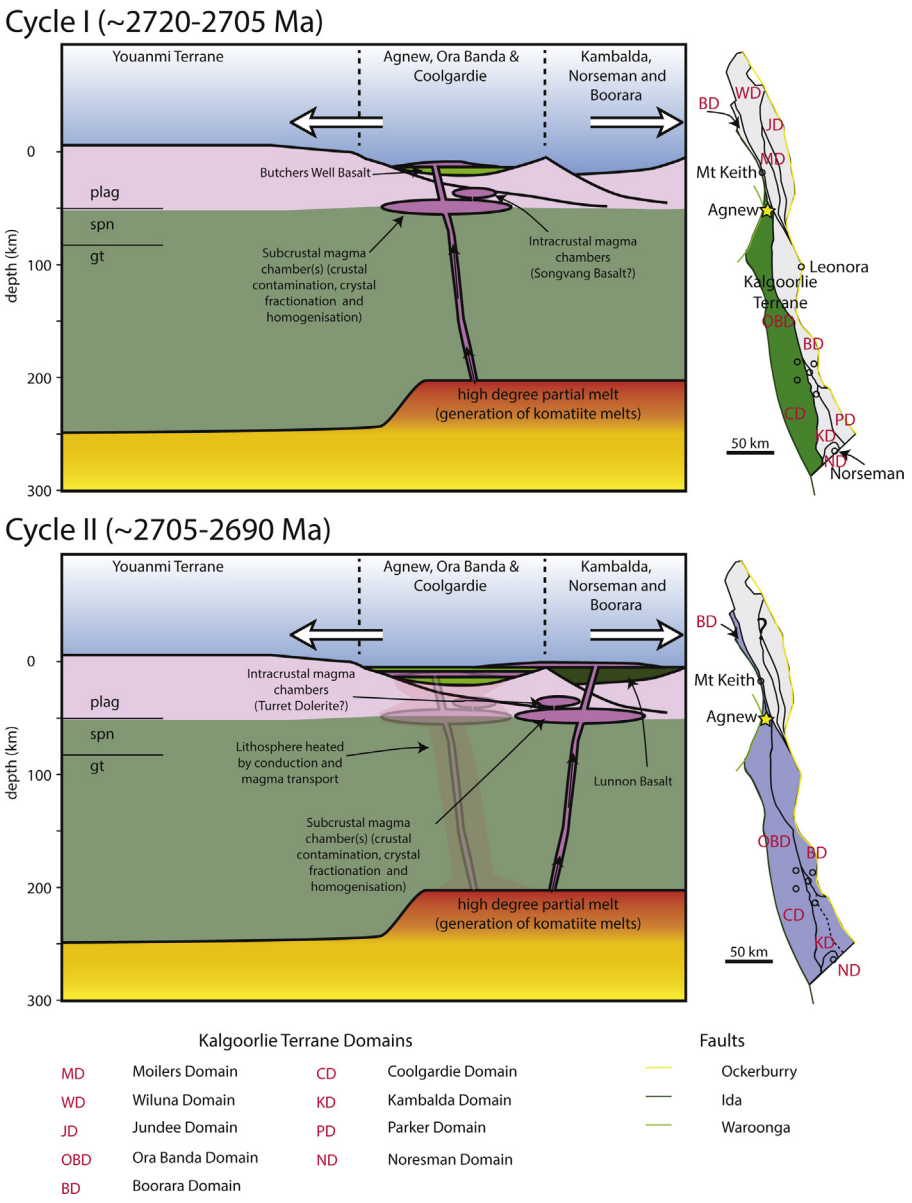

Fig. 16. Spatial distribution of 2720–2690 Ma mafic-ultramafic rocks in the Kalgoorlie Terrane, grouped into cycles I and II.

This unit contains variable proportions of massive, pillowed and breccia lithofacies, and can be subdivided into lower Mg-rich and upper Mg-poor components, which are separated by a thin mudstone (Squire et al., 1998). In many respects the Lunnon Basalt is similar to the Hickies Bore Basalt, however, it is more depleted in LREEs and has a higher ratio of Nb/Th (Fig. 15). The overlying Silver Lake Peridotite is a lithological match to the thick cumulates of the Agnew Komatiite, while the overlying Tripod Hill Komatiite is a good compositional match to the Burrell Well Basalt (Fig. 15). Overlying this is the Devon Consols Basalt and the compositionally similar Victory Dolerite intrusion. These units correlate well with the Redeemer Basalt and its comagmatic intrusion (Fig. 15). Overlying this is the Paringa Basalt and the compositionally similar Defiance Dolerite intrusion (2690 ± 5 Ma; Clout, 1991). The Defiance Dolerite is a compositional and temporal match to the Turret Dolerite (2690.7 ± 1.2 Ma), although there are no known extrusive correlates at Agnew. The Williamstown Peridotite at Kalgoorlie (2696 ± 5 Ma; Fletcher et al., 2001) appears to correlate to the Turrett Dolerite, although geochemistry is lacking. Correlates for the White Hope, Never Can Tell, Songvang, Hickies Bore Basalts, and Donegal Komatiite are not known from the Kambalda Domain, although the base of the Lunnon Basalt is not exposed, and so what underlies it is unknown.

7.2.3. *Coolgardie Domain*

The most detailed stratigraphic and geochemical study of the Coolgardie Domain is by Standing (2001) (Fig. 14), which builds on the work by Hunter (1993). The stratigraphy is a good match with the sequence at Agnew, although there is not enough geochemistry to confidently finger-print some unit. The lowermost unit is the Burbanks Basalt, a massive and pillowed basalt intercalated with thin mafic intrusions, and correlates geochemically and lithologically with the Hickies Bore Basalt lavas and comagmatic intrusions (Figs. 14 and 15). The Burbanks Basalt is separated from an overlying basaltic komatiite unit, known as the Brilliant Ultramafic, and in places by the Greenmont Sill (high-Mg basaltic rocks), by a thin sedimentary interval. The high-Mg character and lithologies of the Brilliant Ultramafic and Greenmong Sill match the Songvang Basalt and its comagmatic intrusion well, although detailed geochemistry is lacking. Overlying this is the Lindsay Basalt, a dominantly

pillowed high-Fe tholeiite. The lithology and distinctive geochemistry (e.g., Th vs. TiO_2; Fig. 15) of this unit match well with the Never Can Tell Basalt. The Lindsay Basalt is intercalated with several thin sediment intervals and intruded by the Three Mile Sill, a 150–800 m thick differentiated mafic intrusion that may correlate with the Bounty Igneous Complex, but trace element geochemistry is lacking. The Lindsay Basalt is overlain by the Hampton Formation, which has spinifex texture in places, and displays a range of compositions, from komatiite, through komatiitic basalt to high-Mg basalt, which in turn is overlain by the basaltic and high-Mg basaltic Gleeson Basalt. These units correlate lithologically with the Agnew Komatiite and the overlying Burrell Well and Redeemer Basalts. There is no overlying unit that correlates stratigraphically with the White Hope Basalt, however, megacrystic basalts (e.g., 'cat-rock') have been reported in the Coolgardie area (Hunter, 1993; Morris, 1993), where they occur below the Hampton Formation, although it is unclear if these are extrusive or intrusive rocks (Hunter, 1993).

7.2.4. Boorara Domain

The Boorara Domain, as proposed by Cassidy et al. (2006), can be traced for over 300 km, from near Black Swan in the south, to north of Mount Keith. To the south of Agnew, the Boorara Domain is located along the eastern margin of the Kalgoorlie Terrane, whereas the domain occurs along the western edge of the terrane to the north of Agnew. Comagmatic komatiitic and dacitic volcanism are common in the Boorara Domain.

Around Black Swan (~280 km S-SE of Agnew), a simple stratigraphy has been developed by Trofimovs et al. (2004), building on work by Swager (1997). The lowermost basalt, the Scotia Basalt, is massive and pillowed and has geochemistry that matches well with the Lunnon Basalt of the Kambalda Domain, and matches poorly with any basalts at Agnew (Fig. 15). Overlying the basalt are primary intercalations of dacite and spinifex-textured (unnamed) komatiite. These units are conformably overlain by an Upper Basalt. There is no published geochemical data on the komatiite or upper basalts.

The Mount Keith (~60 km N of Agnew) nickel mine is hosted in Boorara Domain greenstones and is characterised by three komatiites, comagmatic dacitic volcanism, and intercalated basalt (Beresford et al., 2004; Rosengren et al., 2008; Fiorentini et al., 2012) (Fig. 14). However, without geochemistry on the basalts, it is difficult to test correlations. The basal unit, the McFarlanes Basalt, is a poorly preserved pillowed unit, and overlying this is the Mount Keith Ultramafic, which is characterised by adcumulate textures, high MgO (25–30%; Fiorentini et al., 2010) and [La/Sm] >1.5 (Fiorentini et al., 2010; Gole et al., 2013). Overlying this unit is the Centenary Bore Basalt, a massive and pillowed high-Mg and high-Fe unit. The next overlying unit is the Cliffs Ultramafic, a spinifex-textured komatiite with 25–30 wt.% MgO and [La/Sm] <1 that includes comagmatic dacite intrusions (Fiorentini et al., 2010). Overlying this is another basalt unit, which is turn is overlain by the spinifex-textured Monument Ultramafic. The top of the mafic-ultramafic sequence is another unnamed basalt unit. The Mount Keith Ultramafic has been interpreted as a comagmatic intrusion to the extrusive Cliffs Ultramafic, and its higher [La/Sm] content an indicator of contamination by syn-intrusive dacites (Fiorentini et al., 2010). We propose an alternative origin for the Mount Keith Ultramafic that is consistent with both geochemistry and geochronology (~2707–2712 Ma) of Fiorentini et al. (2010), and the faulted upper contact interpretation of Gole et al. (2013), and which fits well with the Agnew stratigraphy. We correlate the McFarlanes Basalt, Mount Keith Ultramafic, Centenary Bore and Cliffs Ultramafic with the Hickies Bore Basalt, Songvang Basalt, Never Can Tell Basalt and Agnew Komatiite, respectively. In this correlation, the absence of extrusive rocks at Mount Keith (correlatives to the Songvang Basalt sheet flows) could be a result of faulting or that they have not been recognised. There is not enough data on the overlying basalts and Monument Ultramafic to suggest correlations.

The Cosmos (~25 km N of Agnew) nickel mine is characterised by three ultramafic horizons, coherent and fragmental extrusive lithologies, and compositions ranging from andesitic-basalt through to rhyolite (de Joux et al., 2013). The oldest komatiitic event at Cosmos is ~2736–2730 Ma, while the two younger komatiitic events at Cosmos are ~2724–2685 Ma and ~2685–2670 Ma (de Joux et al., 2013). The ages of the komatiites and the dominantly intermediate to felsic character of the sequence cannot be correlated with the Agnew section.

7.2.5. Norseman Domain

The Norseman Domain (470 km south of Agnew) is located at the southern edge of the Kalgoorlie Terrane. Although structurally complicated, the domain is generally considered to consist of a two-part stratigraphy. The lower part includes the poorly understood Penneshaw Formation, which includes some of the oldest ages known for the Eastern Goldfields Superterrane, including detrital ages generally in the ~2865–2985 range, but extending to ~3650 Ma (Campbell and Hill, 1988; Barley et al., 2008). The upper part of the sequence is composed of three sequences: the basal Noganyer (sedimentary rocks, banded iron formation, mafic and ultramafic rocks), Woolyeenyer (pillow lavas, minor mudstone and felsic rocks) and upper Mount Kirk (felsic, mafic to ultramafic rocks, including sediments) formations (Doepel, 1973). A mafic intrusion within the Woolyeenyer Formation has been dated at 2714 ± 5 (Hill et al., 1992), suggesting that part of the sequence at Norseman is a similar age to the lower mafic rocks elsewhere in the Kalgoorlie Terrane. The relationship between the dated sample and the basalts analysed for geochemistry by Said et al. (2010) is unclear, however, there are compositional similarities with the Lunnon (Kambalda) and Scotia (Boorara) Basalts, and differences to the lower tholeiitic basalts of the other domains (Coolgardie and Ora Banda), in terms of Nb/Th, [La/Sm] and Th content (Fig. 15).

7.2.6. Komatiites

This study highlights the presence of two separate komatiites at Agnew, each characterised by well-developed layered spinifex-textured compound flows, with primitive uncontaminated compositions and similarities to Munro-type komatiites. We found no suitable correlates in the Kalgoorlie Terrane for the lower komatiite (Donegal Komatiite), however, the upper komatiite (Agnew Komatiite) is correlated across the Kambalda, Ora Banda and Coolgardie Domains because of the compositional and geochemical similarities with the overlying basalts (Agnew cycle II basalts, with the exception of the less regionally widespread megacrystic White Hope Basalt). Correlations are extended, albeit with less confidence, to the Norseman and Boorara Domains because of similarities between the basalts immediately below the komatiite to the Lunnon Basalt (Kambalda Domain). There is uncertainty as to the age of the upper komatiite, which we explore in detail below.

The age of the Kambalda Komatiite has been dated from interflow sediments at Kambalda and is ~2705 Ma (2702 ± 4 Ma: Campbell and Hill, 1988; 2709 ± 4 Ma; Connors et al., 2005). The other approach to constrain its age has been to date syn-depositional dacites and felsic clasts derived from interlayered fragmental rocks, both of which are only common in the Boorara Domain. Dacites from Black Swan (southern Boorara Domain) have yielded ages of 2708 ± 7 Ma (Ballarat Last Chance, Nelson, 1997), while clasts have yielded an age of 2707 ± 4 Ma (Kositcin et al., 2008). However, there is considerable controversy as to whether the dacites are indeed syn-depositional (e.g., Gole et al., 2013), and in any case, this approach fails to directly date the stratigraphically well constrained komatiites from the Kambalda and

Ora Banda Domains. In the northern Boorara Domain (e.g., Mt Keith and Cosmos) syn-depositional dacites yield some slightly older ages to those reported from Kambalda and southern Boorara, although they are within error: 2713 ± 6 Ma and 2706 ± 6 Ma (footwall and hangingwall dacites, respectively, to the Mt Keith Ultramafic; Fiorentini et al., 2005) and 2711 ± 6 Ma (Albion Downs; Fiorentini et al., 2005). We have outlined our arguments for correlating the Mount Keith Dunite to the Songvang Basalt (Section 7.2.4). If this interpretation is correct, the 2706–2713 Ma ages date the emplacement of the Songvang Basalt during cycle I.

Younger komatiitic events have also been proposed. Coeval dacites at Golden Ridge (southern Boorara) yield a 2697 ± 4 Ma age (Krapež and Pickard, 2010), and an extrusive rhyolite and late felsic intrusion bracket the age of komatiitic volcanism at Cosmos (northern Boorara) between ~2685 and 2670 Ma (de Joux et al., 2013). The older age is permissible with the existing stratigraphic correlations and age constraints, or it may indeed represent a younger komatiitic event; however, the youngest age does not correlate with any known events elsewhere in the Kalgoorlie Terrane.

7.3. Implications for the geodynamic setting and mineral exploration

An important result of this study is our demonstration that the supracrustal stratigraphy of the Kalgoorlie Terrane can be confidently traced for hundreds of kilometres across the domain boundaries proposed by Cassidy et al. (2006). Furthermore, we have shown that the differences in the stratigraphy below the regional komatiite are not the result of variable preservation or exposure. Instead, two distinct stratigraphic groups can be recognised below the regional komatiite. One group (cycle I), which includes the Ora Banda, Agnew, Coolgardie and tentatively the Mount Keith greenstone belts, is characterised by an older komatiite, overlain by crustally contaminated units, including the distinctive high-Fe Never Can Tell and Missouri Basalts. In addition to having high Fe, these basalts are also weakly LREE enriched and have negative Eu anomalies (Fig. 15). The basalts from the other group, at the same age and stratigraphic level, are the Lunnon, Woolyeenyer and Scotia Basalts. These differ from the Never Can Tell and Missouri Basalts in having lower Fe, no Eu anomaly, LREE depletion and lower total REE (Fig. 15). The former can be derived from the later by fractional crystallisation; Fe-enrichment being a characteristic of fractional crystallisation of tholeiitic magmas.

The two >2705 Ma groups are separated by the Bardoc Fault System, a <12 km wide deformed zone with tight to isoclinal folding (Morey et al., 2007), which is composed of the Bardoc Fault and the Abattoir and Zuleika Shear Zones (Cassidy et al., 2006). The Never Can Tell-type volcanism occurs to the west of the fault system, whereas the Lunnon-type is present to the east. We suggest that there is a fundamental difference between the lower crust to the east and west of the fault system, such that magma chambers could form to the west of the Bardoc Fault System but not to the east. Thus, the Bardoc Fault System represents a tectonically important bounding structure.

Autochthonous basement underlies at least some of the Kambalda and Norseman Domains, as inferred from both Pb isotope studies of granites (Oversby, 1975) and the presence of very old inherited zircons (Compston et al., 1986; Hill et al., 1989). Although there are no similar datasets to for the Ora Banda and Coolgardie Domains, whole-rock Sm-Nd and Lu-Hf in zircon isotopic studies are consistent with an autochthonous model and argue against an origin for the Kalgoorlie Terrane basement by amalgamation of exotic terranes (Wyche et al., 2012). Studies in the northeast of the Yilgarn craton have found rocks of similar lithology and age to those in the Youannmi Terrane (immediately west of the Kalgoorlie Terrane) and suggest ~2720 Ma extension resulting in crustal thinning, but not rifting and widespread formation of oceanic crust (Pawley et al., 2012).

The ~2705 Ma komatiite eruption, which produced the Agnew Komatiite, Siberia Komatiite, Hampton Formation, Hannan's Lake Serpentinite, Kambalda Komatiite and Cliffs Ultramafic, is a regional event that can be correlated across the whole Kalgoorlie Terrane, and this is also the case for most of the upper basalts, suggesting a common magmatic history after ~2705 Ma (i.e., cycle II) (Fig. 14).

The observation that the basaltic units, which make up the bulk of the Kalgoorlie Terrane, can be traced over hundreds of kilometres is consistent with them being the Archean equivalent of flood basalts and therefore the melting product of a mantle plume (Campbell and Hill, 1988). They cannot be the product of calc-alkaline volcanism, which is dominated by pyroclastic eruption and units that cannot normally be correlated over distances of more than tens of kilometres (Campbell, 2001). However, calc-alkaline volcanism is important in the adjacent Kurnalpi Terrane.

The principal exploration implications of being able to trace stratigraphic units over great distances (>100 km) is that the regional ~2705 Ma komatiite is prospective for nickel wherever its lower contact offers a source of S. If the Mount Keith Dunite correlates with the Songvang Basalt, then local and regional exploration should also consider this stratigraphic level prospective for Ni-sulphide mineralisation. Stratigraphic horizons hosting other base metal occurrences, such as the Zn-Ag-Ag Nimbus VMS deposit (Hollis et al., 2014), are similarly prospective.

8. Conclusions

The principal findings of this study on the mafic-ultramafic stratigraphy of the Agnew Greenstone Belt, Kalgoorlie Terrane, Western Australia, include:

- The greenstone stratigraphy at Agnew consists of nine conformable subaqueous extrusions (and comagmatic intrusions), as well two layered mafic intrusive units.
- The stratigraphy can be divided into two cycles, each of which has a komatiite at the beginning of the cycle.
- Geochronological constraints provided from mafic intrusions and interflow sediments indicate that most of the stratigraphy was emplaced in ~20 m.y. (~2710–2690 Ma), but detrital zircon data from previous studies indicate the onset of magmatism may have been closer to 2720 Ma. Combined with regional datasets, the voluminous ultramafic–mafic magmatism associated with the Agnew thermal event thus spanned ~30 m.y., with each cycle lasting ~15 m.y.
- Magmatism was derived primarily from one source similar in composition to the modern Depleted Mantle.
- Crustal contamination is evident in most other units, as judged by [La/Sm] > 1, negative Nb and Ti anomalies, and geochemical mixing trends towards felsic contaminants.
- The range of melt compositions formed when a komatiitic magma pooled within the crust in magma chambers where they fractionated crystals, assimilated crust and homogenised, before eruption.
- The shift from cycle I to cycle II magmatism at ~2705 Ma may reflect a change in the crustal pathways, as a new unheated pathway is exploited for the eruption of cycle II magma.
- Cycle I volcanism (~2720–2705 Ma) occurred on the western margin of the Kalgoorlie Terrane, encompassing Ora Banda (including the Agnew greenstone belt) and Coolgardie Domains.
- Cycle II volcanism (~2705–2690 Ma) was more widespread, covering at least Ora Banda, Coolgardie and Kambalda Domains,

indicating a common history across much of the Kalgoorlie Terrane.

Acknowledgments

This research is part of ARC Linkage Project LP110200747. Data for the Coolgardie Domain was kindly provided by Jon Standing. Ashely Uren is thanked for his patient work finding zircons in 'undateable rocks'. We are also very grateful to Jean Bédard and Paul Duuring for their constructive reviews. PCH would like to thank Dr. Massimo Raveggi for his help with the trace element geochemistry.

Appendix A. Supplementary data

Supplementary data associated with this article can be found, in the online version, at http://dx.doi.org/10.1016/j.precamres.2015.09.016.

References

Amelin, Y., Kaltenbach, A., Iizuka, T., Stirling, C.H., Ireland, T.R., Petaev, M., Jacobsen, S.B., 2010. U–Pb chronology of the Solar System's oldest solids with variable 238U/235U. Earth Planet. Sci. Lett. 300, 343–350.

Amelin, Y., Lee, D.C., Halliday, A.N., Pidgeon, R.T., 1999. Nature of the Earth's earliest crust from hafnium isotopes in single detrital zircons. Nature 399, 252–255.

Arndt, N., Bruzak, G., Reischmann, T., 2001. The oldest continental and oceanic plateaus: geochemistry of basalts and komatiites of the Pilbara craton Australia. In: Ernst, R.E., Buchan, K.L. (Eds.), Mantle Plumes: Their Identification Through Time. Geological Society of America Special Paper, pp. 359–387.

Arndt, N.T., Jenner, G.A., 1986. Crustally contaminated komatiites and basalts from Kambalda, Western-Australia. Chem. Geol. 56, 229–255.

Arndt, N.T., Lesher, C.M., Barnes, S.J., 2008. Komatiite. Cambridge University Press, Cambridge.

Ayer, J., Amelin, Y., Corfu, F., Kamo, S., Ketchum, J., Kwok, K., Trowell, N., 2002. Evolution of the southern Abitibi greenstone belt based on U–Pb geochronology: autochthonous volcanic construction followed by plutonism, regional deformation and sedimentation. Precambrian Res. 115, 63–95.

Backhous, S., 2008. Zonation of a Late Archean Dolerite-Gabbro Sill: Implications for Lode Gold Mineralisation in the High-Grade Vivien Deposit, Agnew Region, Yilgarn Craton, Western Australia. School of Geosciences, Monash University, Melbourne, pp. 160.

Baltazar, O.F., Zucchetti, M., 2007. Lithofacies associations and structural evolution of the Archean Rio das Velhas greenstone belt, Quadrilátero Ferrífero, Brazil: a review of the setting of gold deposits. Ore Geol. Rev. 32, 471–499.

Barley, M.E., Krapež, B., Kositcin, N., Cassidy, K., Champion, D.C., Doyle, M., Brown, S., Amira P763/pmd*CRC Project Y1 2008. Terrane Stratigraphy of the Eastern Goldfields Superterrane and Review of the Geotectonic History.

Barnes, S.J., Fisher, L.A., Anand, R., Uemoto, T., 2014. Mapping bedrock lithologies through in situ regolith using retained element ratios: a case study from the Agnew-Lawlers area, Western Australia. Aust. J. Earth Sci. 61, 269–285.

Barnes, S.J., Van Kranendonk, M.J., Sonntag, I., 2012. Geochemistry and tectonic setting of basalts from the Eastern Goldfields Superterrane. Aust. J. Earth Sci. 59, 707–735.

Barrie, C.T., Corfu, F., Davis, P., Coutts, A.C., MacEachern, D., 1999. Geochemistry of the Dundonald Komatiite-Basalt Suite and genesis of Dundeal Ni deposit, Abitibi Subprovince, Canada. Econ. Geol. 94, 845–866.

Bateman, R., Costa, S., Swe, T., Lambert, D., 2001. Archaean mafic magmatism in the Kalgoorlie area of the Yilgarn Craton Western Australia: a geochemical and Nd isotopic study of the petrogenetic and tectonic evolution of a greenstone belt. Precambrian Res. 108, 75–112.

Bavinton, O.A., Taylor, S.R., 1980. Rare-Earth element geochemistry of Archean metasedimentary rocks from Kambalda, Western-Australia. Geochim. Cosmochim. Acta 44, 639–648.

Beardsmore, T.J., 2002. The Geology, Tectonic Evolution and Gold Mineralisation of the Lawlers Region: A Synopsis of Present Knowledge. Barrick Gold of Australia, pp. 279.

Bédard, J.H., 2013. How many arcs can dance on the head of a plume?: a 'Comment' on: A critical assessment of Neoarchean 'plume only' geodynamics: evidence from the Superior province, by Derek Wyman, Precambrian Research, 2012. Precambrian Res. 229, 189–197.

Bédard, J.H., Harris, L.B., Thurston, P.C., 2013. The hunting of the snArc. Precambrian Res. 229, 20–48.

Beresford, S.W., Fiorentini, M., Rosengren, N.M., Duuring, P., Barley, M.E., Bleeker, W., In: Report A.P.F. 2004. The structural and stratigraphic architecture of the Agnew-Wiluna greenstone belt, Western Australia.

Black, L.P., Champion, D.C., Cassidy, K., Geoscience Australia Record 2002. Compilation of SHRIMP U–Pb Geochronology Data, Yilgarn Craton, Western Australia, 1997–2000.

Blewett, R.S., Czarnota, K., Henson, P.A., 2010. Structural-event framework for the eastern Yilgarn Craton Western Australia, and its implications for orogenic gold. Precambrian Res. 183, 203–229.

Boggs, S., 1987. Principles of Sedimentology and Stratigraphy. Merrill Publishing Company, Columbus.

Bryan, S.E., Ernst, R.E., 2008. Revised definition of large igneous provinces (LIPs). Earth Sci. Rev. 86, 175–202.

Campbell, I.H., 2001. The identification of old mantle plumes. Geol. Soc. Am. Spec. Publ. 352, 5–21.

Campbell, I.H., Griffiths, R.W., Hill, R.I., 1989. Melting in an Archaean mantle plume: heads it's basalts, tails it's komatiites. Nature 339, 697–699.

Campbell, I.H., Hill, R.I., 1988. A 2-stage model for the formation of the granite-greenstone terrains of the Kagoorlie-Norsemand area, Western Australia. Earth Planet. Sci. Lett. 90, 11–25.

Carey, M.L., 1994. Petrgraphy and Geochemistry of Selected Sills from the Kambalda-Kalgoorlie Region. W.A. Australian National University, B. Sc. (Hons.) thesis, Canberra, pp. 80.

Cassidy, K.F., Champion, D.C., Krapež, B., Barley, M.E., Brown, S.J.A., Blewett, R.S., Groenewald, P.B., Tyler, I.M., Geological Survey of Western Australia 2006. A Revised Geological Framework for the Yilgarn Craton, Western Australia., pp. 8.

Champion, D.C., Cassidy, K., 2007. An overview of the Yilgarn Craton and its crustal evolution. In: Bierlein, F.P., Knox-Robinson, C.M. (Eds.), Kalgoorlie '07 Conference. Geoscience Australia, Kalgoorlie, pp. 8–13.

Champion, D.C., Sheraton, J.W., 1997. Geochemistry and Nd isotope systematics of Archaean granites of the Eastern Goldfields, Yilgarn Craton Australia: implications for crustal growth processes. Precambrian Res. 83, 109–132.

Claoue-Long, J.C., Compston, W., Cowden, A., 1988. The age of tha Kambalda greenstones resolved by ion-microprobe: implications for Archean dating methods. Earth Planet. Sci. Lett. 89, 239–259.

Clifton, H.E., Dingler, J.R., 1984. Wave-formed structures and paleoenvironmental reconstruction. Mar. Geol. 60, 165–198.

Clout, J.M.F., 1991. Geochronology of the Kambalda-Kalgoorlie area: A Review. Western Mining Corporation.

Coleman, R.G., McGuire, A.V., 1988. Magma systems related to the Red Sea Opening. Tectonophysics 150, 77–100.

Compston, W., Williams, I.S., Campbell, I.H., Gresham, J.J., 1986. Zircon xenocrysts from the Kambalda volcanics – age constraints and direct evidence for older continental-crust below the Kambalda-Norseman Greenstones. Earth Planet. Sci. Lett. 76, 299–311.

Compston, W., Williams, I.S., Kirschvink, J.L., Zhang Zichau, M.G., 1992. Zircon U–Pb ages for the Early Cambrian time-scale. J. Geol. Soc. Lond. 149, 171–184.

Connors, K., Donaldson, J., Morrison, B., Davy's, C., Neumeyer, P., Technical Note: SIG0329 2005. The Stratigraphy of the Kambalda-St ives District: Workshop Notes. St Ives Gold Fields, pp. 1–99.

Cox, K.G., Hawkesworth, C.J., 1984. Geochemical stratigraphy of the Deccan Traps at Mahabaleshwar, Western Ghats, India, with implications for open system magmatic processes. J. Petrol. 26, 355–377.

de Joux, A., Thordarson, T., Denny, M., Hinton, R.W., de Joux, A.J., 2013. U–Pb dating constraints on the felsic and intermediate volcanic sequence of the nickel-sulphide bearing Cosmos succession, Agnew-Wiluna greenstone belt, Yilgarn Craton, Western Australia. Precambrian Res. 236, 85–105.

Doepel, J.J.G., 1973. Norseman Western Australia 1250000 Geological Series – Explanatory Notes. Department of Mines, Western Australia, pp. 40.

Dunphy, J.M., Fletcher, I.R., Cassidy, K.F., Champion, D.C., Record G.A. 2003. Compilation of SHRIMP U–Pb Geochronological Data, Yilgarn Craton, Western Australia, 2001–2002., pp. 139.

Duuring, P., Bleeker, W., Beresford, S.W., 2007. Structural modification of the komatiite-associated Harmony nickel sulfide deposit, Leinster, Western Australia. Econ. Geol. 102, 277–297.

Duuring, P., Bleeker, W., Beresford, S.W., Fiorentini, M.L., Rosengren, N.M., 2012. Structural evolution of the Agnew-Wiluna greenstone belt Eastern Yilgarn Craton and implications for komatiite-hosted Ni sulfide exploration. Aust. J. Earth Sci. 59, 765–791.

Ernst, R.E., Bleeker, W., Söderlund, U., Kerr, A.C., 2013. Large Igneous Provinces and supercontinents: toward completing the plate tectonic revolution. Lithos 174, 1–14.

Fink, J.H., Griffiths, R.W., 1992. A laboratory analog study of the surface-morphology of lava flows extruded from point and line sources. J. Volcanol. Geotherm. Res. 54, 19–32.

Fiorentini, M., Beresford, S., Barley, M., Duuring, P., Bekker, A., Rosengren, N., Cas, R.A.F., Hronsky, J., 2012. District to camp controls on the genesis of komatiite-hosted nickel sulfide deposits, Agnew-Wiluna greenstone belt Western Australia: insights from the multiple sulfur isotopes. Econ. Geol. 107, 781–796.

Fiorentini, M.L., Barley, M.E., Pickard, A.L., Beresford, S.W., Rosengren, N., Cas, R.A.F., Duuring, P., 2005. Age Constraints of the Structural and Stratigraphic Architecture of the Agnew-Wiluna Greenstone Belt: Implications for the Age of Komatiite-Felsic Association and Interaction in the Eastern Goldfields Province, Western Australia: Perth, MERIWA Final Report. Minerals and Energy Research Institute of Western Australia, pp. 39.

Fiorentini, M.L., Beresford, S.W., Rosengren, N., Barley, M.E., McCuaig, T.C., 2010. Contrasting komatiite belts, associated Ni-Cu-(PGE) deposit styles and assimilation histories. Aust. J. Earth Sci. 57, 543–566.

Fitton, J.G., Godard, M., 2004. Origin and evolution of magmas on the Ontong Java Plateau. Geol. Soc. Lond. Spec. Publ. 229, 151–178.

Fitton, J.G., Larsen, L.M., Saunders, A.D., Hardarson, B.S., Kempton, P.D., 2000. Palaeogene continental to oceanic magmatism on the SE Greenland Continental Margin at 63 N: a review of the results of ocean drilling program legs 152 and 163. J. Petrol. 41, 951–966.
Fletcher, I.R., Dunphy, J.M., Cassidy, K.F., Champion, D.C., Geoscience Australia Record 2001. Compilation of SHRIMP U–Pb Geochronology Data, Yilgarn Craton, Western Australia., pp. 111.
Fletcher, I.R., Mikucki, J.A., McNaughton, N.J., Mikucki, E.J., Groves, D.I., 1988. The Age of Felsic Magmatism and Lode-Gold Mineralisation Events in the Lawlers Area, Yilgarn Craton, Western Australia. Geological Society of Australia Abstract, pp. 146.
Gole, M.J., Robertson, J., Barnes, S.J., 2013. Extrusive origin and structural modification of the Komatiitic Mount Keith ultramafic unit. Econ. Geol. 108, 1731–1752.
Gregory, M.J., 1998. The Geochemistry and Petrology of the Enterprise Dolerite, Ora Banda, Western Australia. School of Earth Sciences, University of Melbourne.
Griffiths, R.W., Fink, J.H., 1992. Solidification and morphology of submarine lavas – a dependence on estrusion rate. J. Geophys. Res. 97, 19729–19737.
Hall, C.E., Pawley, M.J., Sapkota, J., Wyche, S., Geological Information Series 2014. 1:100,000 Interpreted Bedrock Geology Geological Survey of Western Australia East Yilgarn 2014 Geological Survey of Western Australia.
Hawksworth, C.J., Blake, S., Evans, P., Hughes, R., Macdonald, R., Thomas, L.E., Turner, S.P., Zellmer, G., 2000. Time scales of crystal fractionation in magma chambers – integrating physical, isotopic and geochemical perspectives. J. Petrol. 41, 991–1006.
Hill, R.E.T., Barnes, S.J., Gole, M.J., Dowling, S.E., 1995. The volcanology of komatiites as deduced from field relationships in the Norseman-Wiluna greenstone-belt, Western Australia. Lithos 34, 159–188.
Hill, R.I., Campbell, I.H., Compston, W., 1989. Age and origin of granitic-rocks in the Kalgoorlie-Norseman region of Western Australia – implications for the origin of Archean crust. Geochim. Cosmochim. Acta 53, 1259–1275.
Hill, R.I., Chappell, B.W., Campbell, I.H., 1992. Late Archean granites of the Southeastern Yilgarn Block Western-Australia – age, geochemistry, and origin. Trans. R. Soc. Edinb. Earth Sci. 83, 211–226.
Hollings, P., Kerrich, R., 1999. Trace element systematics of ultramafic and mafic volcanic rocks from the 3 Ga North Caribou greenstone belt, northwestern Superior Province. Precambrian Res. 93, 257–279.
Hollis, S.P., Yeats, C.J., Wyche, S., Barnes, S.J., Ivanic, T.J., Belford, S.M., Davidson, G.J., Roache, A.J., Wingate, M.T.D., 2014. A review of volcanic-hosted massive sulfide (VHMS) mineralization in the Archean Yilgarn Craton, Western Australia: tectonic, stratigraphic and geochemical associations. Precambrian Res., http://dx.doi.org/10.1016/j.precamres.2014.11.002.
Hooper, P.R., Camp, V.E., Reidel, S.P., Ross, M.E., 2007. The origin of the Columbia River flood basalt province: Plume versus nonplume models. Plates Plumes Planet. Process. 430, 635–656.
Hunter, W.M., In: Australia, G.S.o.W. 1993. Geology of the Granite-Greenstone Terrane of the Kalgoorlie and Yilmia 1:100,000 Sheets, Western Australia., pp. 78.
Huppert, H.E., Sparks, R.S.J., 1985. Cooling and contamination of mafic and ultramafic magmas during ascent through continental crust. Earth Planet. Sci. Lett. 74, 371–386.
Irvine, T.N., Baragar, W.R.A., 1971. A guide to the chemical classification of the common volcanic rocks. Can. J. Earth Sci. 8, 523–548.
Jowitt, S.M., Ernst, R.E., 2013. Geochemical assessment of the metallogenic potential of Proterozoic LIPs of Canada. Lithos 174, 291–307.
Kent, A.J.R., McDougall, I., 1995. 40Ar-39Ar and U–Pb age constraints on the timing of gold mineralisation in the Kalgoorlie gold field, Western Australia. Econ. Geol. 90, 845–859.
Kositcin, N., Brown, S.J.A., Barley, M.A., Krapež, B., Cassidy, K.F., Champion, D.C., 2008. SHRIMP U–Pb zircon age constraints on the Late Archaean tectonostratigraphic architecture of the Eastern Goldfields Superterrane, Yilgarn Craton, Western Australia. Precambrian Res. 161, 5–33.
Krapež, B., Barley, M.E., Brown, S.J.A., 2008. Late Archaean synorogenic basins of the Eastern Goldfields Superterrane, Yilgarn Craton Western Australia Part III. Signatures of tectonic escape in an arc-continent collision zone. Precambrian Res. 161, 183–199.
Krapež, B., Hand, J.L., 2008. Late Archaean deep-marine volcaniclastic sedimentation in an arc-related bas The Kalgoorlie Sequence of the Eastern Goldfields Superterrane Yilgarn Craton, Western Australia. Precambrian Res. 161, 89–113.
Krapež, B., Pickard, A.L., 2010. Detrital-zircon age-spectra for Late Archaean synorogenic basins of the Eastern Goldfields Superterrane, Western Australia. Precambrian Res. 178, 91–118.
Lesher, C.M., Arndt, N.T., 1995. REE and Nd isotope geochemistry, petrogenesis and volcanic evolution of contaminated komatiites at Kambalda, Western Australia. Lithos 34, 127–157.
Lightfoot, P.C., Hawkesworth, C.J., Hergt, J., Naldrett, A.J., Gorbachev, N.S., Fedorenko, V.A., Doherty, W., 1993. Remobilization of the continental lithosphere by a mantle plume: major element, trace-element, and Sr-, Nd-, and Pb-isotope evidence from picritic and tholeiitic lavas of the Noril'sk District, Siberian Trap, Russia. Contrib. Mineral. Petrol. 114, 171–188.
Ludwig, K.R., 2003. Isoplot 3.00: A Geochronological Toolkit for Microsoft Excel. Berkeley Geochronology Center.
Ludwig, K.R., 2009. Squid 2.50, A User's Manual. Berkeley Geochronology Centre, Berkeley, CA, USA.
Marsh, J.S., Bowen, M.P., Rogers, N.W., Bowen, T.B., 1992. Petrogenesis of Late Archean flood-type basic lavas from the Klipriviersberg Group, Ventersforp Supergroup, South-Africa. J. Petrol. 33, 817–847.
Mattinson, J.M., 2005. Zircon U–Pb chemical abrasion ("CA-TIMS") method: combined annealing and multi-step dissolution analysis for improved precision and accuracy of zircon ages. Chem. Geol. 220, 47–66.
Mattinson, J.M., 2011. Extending the Krogh legacy: development of the CA-TIMS method for zircon U–Pb geochronology. Can. J. Earth Sci. 48, 95–105.
McDonough, W.F., Ireland, T.R., 1993. Intraplate origin of komatiites inferred from trace elements in glass inclusions. Nature 365, 432–434.
McDonough, W.F., Sun, S.S., 1995. The composition of the Earth. Chem. Geol. 120, 223–253.
Mole, D.R., Fiorentini, M.L., Thébaud, N., McCuaig, T.C., Cassidy, K.F., Kirkland, C.L., Wingate, M.T.D., Romano, S.S., Doublier, M.P., Belousova, E.A., 2012. Spatio-temporal constraints on lithospheric development in the southwest-central Yilgarn Craton, Western Australia. Aust. J. Earth Sci. 59, 625–656.
Morey, A.A., Weinberg, R.F., Bierlein, F.P., 2007. The structural controls of gold mineralisation within the Bardoc Tectonic Zone, Eastern Goldfields Province, Western Australia: implications for gold endowment in shear systems. Miner. Depos. 42, 583–600.
Morris, P.A., In: G.S.o.W.A. 1993. Archean Mafic and Ultamafic Volcanic Rocks, Menzies to Norseman, Western Australia Report. Geological Survey of Western Australia, pp. 107.
Nelson, D.R., 1995. Compilation of SHRIMP U–Pb Zircon Geochronology Data 1994. Western Australia Geological Survey, pp. 244.
Nelson, D.R., 1997. Evolution of the Archaean granite-greenstone terranes of the eastern goldfields, Western Australia: SHRIMP U–Pb zircon constraints. Precambrian Res. 83, 57–81.
Nyga, M., 2011. Architecture and Evolution of the Late Archean Successions that Host Gold in the Waroonga-Redeemer Corridor, Agnew, Yilgarn Craton, Western Australia School of Geosciences. Monash University, BSc. Hons. Thesis, pp. 192.
Oversby, V.M., 1975. Lead isotopic systematics and ages of Archaean acid intrusives in the Kalgoorlie-Norseman area, Western Australia. Geochim. Cosmochim. Acta 39, 1107–1125.
Pak, H., Zaneveld, J.R.V., Kitchen, J., 1980. Intermediate nepheloid layers observed off Oregon and Washington. J. Geophys. Res. 85, 6697–6708.
Pawley, M.J., Wingate, M.T.D., Kirkland, C.L., Wyche, S., Hall, C.E., Romano, S.S., Doublier, M.P., 2012. Adding pieces to the puzzle: episodic crustal growth and a new terrane in the northeast Yilgarn Craton, Western Australia. Aust. J. Earth Sci. 59, 603–623.
Pearce, J.A., 2008. Geochemical fingerprinting of oceanic basalts with applications to ophiolite classification and the search for Archean oceanic crust. Lithos 100, 14–48.
Platt, J.P., Allchurch, P.D., Rutland, R.W.R., 1978. Archaean tectonics in the Agnew supracrustal belt, Western Australia. Precambrian Res. 7, 3–30.
Polat, A., Appel, P.W.U., Fryer, B.J., 2011. An overview of the geochemistry of Eoarchean to Mesoarchean ultramafic to mafic volcanic rocks SW Greenland: implications for mantle depletion and petrogenetic processes at subduction zones in the early Earth. Gondwana Res. 20, 255–283.
Polat, A., Li, J., Fryer, B., Kusky, T., Gagnon, J., Zhang, S., 2006. Geochemical characteristics of the Neoarchean (2800–2700 Ma) Taishan greenstone belt North China Craton: evidence for plume-craton interaction. Chem. Geol. 230, 60–87.
Pyke, D.R., Naldrett, A.J., Eckstrand, O.R., 1973. Archean ultramafic flows in Munro Township. Geol. Soc. Am. Bull. 4, 955–978.
Rasmussen, B., Mueller, A.G., Fletcher, I.R., 2009. Zirconolite and xenotime U–Pb age constraints on the emplacement of the Golden Mile Dolerite sill and gold mineralization at the Mt Charlotte mine, Eastern Goldfields Province, Yilgarn Craton, Western Australia. Contrib. Mineral. Petrol. 157, 559–572.
Rey, P.F., Philippot, P., Thébaud, N., 2003. Contribution of mantle plumes, crustal thickening and greenstone blanketing to the 2.75–2.65 Ga global crisis. Precambrian Res. 127, 43–60.
Rollinson, H., 1993. Using Geochemical Data: Evaluation, Presentation, Interpretation. Pearson Prentice Hall, England.
Rosengren, N.M., Beresford, S.W., Grguric, B.A., Cas, R.A.F., 2005. An intrusive origin for the komatiitic dunite-hosted Mount Keith disseminated nickel sulfide deposit, Western Australia. Econ. Geol. 100, 149–156.
Rosengren, N.M., Cas, R.A.F., Beresford, S.W., Palich, B.M., 2008. Reconstruction of an extensive Archaean dacitic submarine volcanic complex associated with the komatiite-hosted Mt Keith nickel deposit, Agnew-Wiluna Greenstone Belt, Yilgarn Craton, Western Australia. Precambrian Res. 161, 34–52.
Rudnick, R.L., Fountain, D.M., 1995. Nature and composition of the continental crust: a lower crustal perspective. Rev. Geophys. 33, 267–309.
Rutherford, M.J., 2008. Magma ascent rates. Rev. Mineral. Geochem. 69, 241–271.
Said, N., Kerrich, R., 2009. Geochemistry of coexisting depleted and enriched Paringa Basalts, in the 2.7 Ga Kalgoorlie Terrane, Yilgarn Craton, Western Australia: Evidence for a heterogeneous mantle plume event. Precambrian Res. 174, 287–309.
Said, N., Kerrich, R., 2010. Elemental and Nd-isotope systematics of the Upper Basalt Unit, 2.7 Ga Kambalda Sequence: quantitative modeling of progressive crustal contamination of plume asthenosphere. Chem. Geol. 273, 193–211.
Said, N., Kerrich, R., Groves, D., 2010. Geochemical systematics of basalts of the Lower Basalt Unit, 2.7 Ga Kambalda Sequence Yilgarn craton, Australia: plume impingement at a rifted craton margin. Lithos 115, 82–100.
Schilling, J.G., Kingsley, R.H., Hanan, B.B., McCully, B.L., 1992. Nd-Sr-Pb isotopic variations along the gulf of ard evidence for afar mantle plume-continental lithosphere. Interact. J. Geophys. Res. Solid Earth 97, 10927–10966.
Schmitz, M.D., Schoene, B., 2007. Derivation of isotope ratios, errors, and error correlations for U–Pb geochronology using 205Pb-235U-(233U)-spiked isotope dilution thermal ionization mass spectrometric data. Geochem. Geophys. Geosyst. 8, Q08006.

Shervais, J.W., 1982. Ti-V plots and the petrogenesis of modern and ophiolitic lavas. Earth Planet. Sci. Lett. 59, 101–118.
Shimizu, K., Nakamura, E., Maruyama, S., 2005. The geochemistry of ultramafic to mafic volcanics from the Belingwe Greenstone Belt, Zimbabwe: magmatism in an Archean Continental Large Igneous Province. J. Petrol. 46, 2367–2394.
Smithies, R.H., Van Kranendonk, M.J., Champion, D.C., 2005. It started with a plume – early Archaean basaltic proto-continental crust. Earth Planet. Sci. Lett. 238, 284–297.
Smithies, R.H., Witt, W.K., 1997. Distinct basement terranes identified from granite geochemistry in late Archaean granite-greenstones, Yilgarn Craton, Western Australia. Precambrian Res. 83, 185–201.
Sparks, R.S.J., 1986. The role of crustal contamination in magma evolution through geological time. Earth Planet. Sci. Lett. 78, 211–223.
Squire, R.J., Allen, C.M., Cas, R.A.F., Campbell, I.H., Blewett, R.S., Nemchin, A.A., 2010. Two cycles of voluminous pyroclastic volcanism and sedimentation related to episodic granite emplacement during the late Archean: Eastern Yilgarn Craton, Western Australia. Precambrian Res. 183, 251–274.
Squire, R.J., Cas, R.A.F., Clout, J.M.F., Behets, R., 1998. Volcanology of the Archaean Lunnon Basalt and its relevance to nickel sulfide-bearing trough structures at Kambalda, Western Australia. Aust. J. Earth Sci. 45, 695–715.
Stacey, J.S., Kramers, J.D., 1975. Approximation of terrestrial lead isotope evolution by a two-stage model. Earth Planet. Sci. Lett. 26, 207–221.
Standing, J.G., In-house report 2001. New Insights into the Structural and Stratigraphic Setting of the Coolgardie District: Implications for Gold Exploration. Fluid Focus Pty Ltd.
Stern, R.A., 2001. A New Isotopic and Trace-Element Standard for the Ion Microprobe: Preliminary Thermal Ionization Mass Spectrometry (TIMS) U–Pb and Electron-Microprobe Data. Current Research 2001-F1. Geological Survey of Canada, pp. 11.
Stern, R.A., Bodorkos, S., Kamo, S.L., Hickman, A.H., Corfu, F., 2009. Measurement of SIMS instrumental mass fractionation of Pb isotopes during zircon dating. Geostand. Geoanal. Res. 33, 145–168.
Swager, C.P., 1997. Tectono-stratigraphy of late Archaean greenstone terranes in the southern eastern goldfields, Western Australia. Precambrian Res. 83, 11–42.
Taylor, S.R., Mclennan, S.M., 1985. The Continental Crust: Its Composition and Evolution. Blackwell, Oxford.
Timmermans, L.J., 2010. Architecture and Evolution of Possible Intrusion Related Au Deposits in the Bellerophon – Little Sandy region, St Ives, Yilgarn Craton Western Australia School of Geosciences. Monash University, Clayton, pp. 90.
Tranthem, C., 2004. The Geochemistry and Tectonic Setting of Archaean mafic volcanic rocks in the Ora Banda Domain of the Kalgoorlie Terrane, Western Australia. The School of Earth and Geographical Sciences. The University of Western Australia, B. Sc. (Hons), Thesis, pp. 139.
Trofimovs, J., Davis, B.K., Cas, R.A.F., 2004. Contemporaneous ultramafic and felsic intrusive and extrusive magmatism in the Archaean Boorara Domain, Eastern Goldfields Superterrane, Western Australia, and its implications. Precambrian Res. 131, 283–304.
van den Boorn, S.H.J.M., van Bergen, M.J., Nijman, W., Vroon, P.Z., 2007. Dual role of seawater and hydrothermal fluids in Early Archean chert formation: evidence from silicon isotopes. Geology 35, 939–942.
van Hunen, J., Moyen, J.F., 2012. Archean Subduction: Fact or Fiction? Annual Review of Earth and Planetary Sciences 40, 195–219.
Van Kranendonk, M.J., 2006. Volcanic degassing, hydrothermal circulation and the flourishing of early life on Earth: A review of the evidence from c. 3490–3240 Ma rocks of the Pilbara Supergroup, Pilbara Craton, Western Australia. Earth Sci. Rev. 74, 197–240.
Van Kranendonk, M.J., Ivanic, T.J., Wingate, M.T.D., Kirkland, C.L., Wyche, S., 2013. Long-lived, autochthonous development of the Archean Murchison Domain, and implications for Yilgarn Craton tectonics. Precambrian Res. 229, 49–92.
Vermeesch, P., 2012. On the visualisation of detrital age distributions. Chem. Geol. 312-313, 190–194.
Weinberg, R.F., van der Borgh, P., 2008. Extension and gold mineralization in the Archean Kalgoorlie Terrane, Yilgarn Craton. Precambrian Res. 161, 77–88.
Werne, J.P., Sageman, B.B., Lyons, T.W., Hollander, D.J., 2002. An integrated assessment of a "Type Euxinic" Deposit: evidence for multiple controls on black shale deposition in the Middle Devonian Oatka Creek Formation. Am. J. Sci. 302, 110–143.
White, J.D.L., Bryan, S.E., Ross, P.-S., Self, S., Thordarson, T., 2009. Physical volcanology of continental large igneous provinces: update and review. In: Thordarson, T., Self, S., Larsen, G., Rowland, S.K., Hoskuldsson, A. (Eds.), Studies in Volcanology: The Legacy of George Walker. Special Publications of IAVCEI. Geological Society, London, pp. 291–321.
Whitworth, A., 2012. Understanding the Contect of Orogenic Gold Deposits in Archean Terranes: Architecture and Evolution of the Stratigraphy north of the Waroonga Complex, Agnew Yilgarn Craton, Western Australia. School of Geosciences. Monash University, BSc. (Hons) Thesis, pp. 282.
Wingate, M.T.D., Kirkland, C.L., 2014. Introduction to Geochronology Information Released in 2014. Geological Survey of Western Australia, pp. 5.
Witt, W.K., 1993. Lithological and structural controls on gold mineralisation in the Archean Menzies-Kambalda area, Western-Australia. Aust. J. Earth Sci. 40, 65–86.
Witt, W.K., 1995. Tholeiitic and high-Mg mafic/ultramafic sills in the Eastern Goldfields Province, Western Australia: implications for tectonic settings. Aust. J. Earth Sci. 42, 407–422.
Woodall, R., 1965. Structure of the Kalgoorlie Goldfield. In: McAndrew, J. (Ed.), Geology of Australian Ore Deposits, 2 ed., 8th Commonwealth Mining and Metallurgical Congress, Australia and New Zealand. , pp. 71–79.
Wyche, S., Kirkland, C.L., Riganti, A., Pawley, M.J., Belousova, E., Wingate, M.T.D., 2012. Isotopic constraints on stratigraphy in the central and eastern Yilgarn Craton, Western Australia. Aust. J. Earth Sci. 59, 657–670.
Wyche, S., Witt, W.K., 1991. Geology of the Davyhurst 1:100,000 Sheet, Western Australia. Geological Survey of Western Australia, pp. 48.